Theoretical study on topological crystalline insulators

米澤, 弦起

https://hdl.handle.net/2324/7393649

出版情報：Kyushu University, 2025, 博士（理学）, 課程博士

Theoretical study on topological crystalline insulators

Genki Yonezawa

May 26, 2025

Abstract

Topology, originally a branch of pure mathematics, has become an essential tool in physics since the latter half of the 20th century. One of its most significant applications is in band topology, which emerged from the study of the quantum Hall effect. This framework classifies band structures using topological invariants, such as the Chern number, which encode the connectivity of wave functions in the Brillouin zone. While the quantum Hall effect relies on broken time-reversal symmetry, it is now well understood that topological phases can also arise in time-reversal-invariant systems, enabled by adopting spin-orbit couplings, crystalline symmetries, and so on.

The concept of band topology is applicable not only to conventional solid-state electronic systems but also to unconventional solid-state analogs. For example, photonic crystals, which consist of periodic variations in the refractive index, support photonic modes that can be characterized by wave vectors within the Brillouin zone. Consequently, the principles of band topology can be applied to photonic crystals, leading to the realization of topological photonic systems exhibiting nontrivial topology in their photonic modes.

Studying band topology in unconventional solid-state systems offers several advantages. Unlike traditional electronic systems, these platforms allow for the realization of models with exotic hopping terms or in dimensions that would be challenging to achieve in real materials. Additionally, since these systems generally do not require ultralow temperatures, they offer better experimental control and enable direct observation of edge states.

This study aims to establish a theoretical framework of topological crystalline insulators which can be applicable to classical systems, such as photonic crystals, without relying on solid-state-specific interactions like spin-orbit coupling. Furthermore, the goal is to construct models that are widely applicable and experimentally accessible. To achieve this, we focus on tight-binding models with only real hopping terms, ensuring feasibility in photonic crystal implementations using simple dielectric rods.

The first key result concerns a model on a chiral honeycomb lattice. We developed a minimal model that describes systems with broken mirror symmetry. Our model is an extension of the Wu–Hu model, which was originally proposed as a minimal model that realizes quantum pseudo spin Hall effect. By incorporating next-nearest-neighbour hopping, the system lose both sublattice and mirror symmetries, and thus becomes topologically distinct from the original Wu-Hu model. Using Dirac Hamiltonian analysis

and Wilson loop calculations, we detected the topological nontriviality of the system. Furthermore, by mapping the model onto a classical mass-spring system, we investigated edge currents and found that a novel asymmetric edge currents attributable to chirality can be excited.

The second key result pertains to the study of the topological quadrupole phase using an extra-site model. We begin with the well-known BBH model, a prototypical model of higher-order topological insulators known to exhibit a topological quadrupole phase. This model fundamentally relies on the sign flip of certain hopping terms. We introduced an extra-site model as a systematic approach to realizing such sign flips and analyzed its properties. Using analytical calculations based on the Brillouin-Wigner formalism and numerical simulations, we demonstrated band inversion analogous to that in the BBH model. Furthermore, numerical calculations confirmed the emergence of corner-localized modes.

Contents

1 Background and Motivation **7**
- 1.1 Topological phase in electronic systems . . . 7
  - 1.1.1 Quantum Hall insulators . . . 7
  - 1.1.2 Quantum spin Hall insulators . . . 9
  - 1.1.3 Topological phase in one-dimensional systems . . . 12
  - 1.1.4 Topological crystalline insulators . . . 14
  - 1.1.5 Higher-order topological insulators . . . 19
- 1.2 Topological phase in unconventional "solids" . . . 23
  - 1.2.1 Ultracold atomic gases . . . 24
  - 1.2.2 Coupled cavity arrays . . . 26
  - 1.2.3 Photonic crystals . . . 28
- 1.3 Motivation for the research in this thesis . . . 35
- 1.4 Organization of this thesis . . . 35

2 Wilson loops and topological invariants **37**
- 2.1 Wilson loops . . . 37
  - 2.1.1 Definitions . . . 37
  - 2.1.2 Hybrid Wannier centers . . . 38
- 2.2 Sublattice symmetry and winding number . . . 39
  - 2.2.1 Basics . . . 39
  - 2.2.2 Su-Schrieffer-Heeger model . . . 41
- 2.3 Mirror symmetry and quadrupole moment . . . 42
  - 2.3.1 π-flux and mirror symmetry . . . 42
  - 2.3.2 Benalcazar-Bernevig-Hughes model . . . 44
- 2.4 Mirror winding number . . . 46
  - 2.4.1 Edge states in honeycomb lattice model . . . 46
  - 2.4.2 Topological characterization of Wu-Hu model . . . 46

3 $\mathbb{Z}_2$ phase in a chiral honeycomb lattice **49**
- 3.1 Introduction . . . 49
- 3.2 Model . . . 51
- 3.3 Band structures and effective Hamiltonian . . . 51
- 3.4 Topological edge states . . . 54

3.5 Berry bands and $\mathbb{Z}_2$ index . . . 55
  3.5.1 Berry bands . . . 57
  3.5.2 C_2T-protected $\mathbb{Z}_2$ phase . . . 58
3.6 Short summary . . . 60

4 Interface transport in the chiral honeycomb lattice 63
4.1 Introduction . . . 63
4.2 Model . . . 64
4.3 Interface transport . . . 65
4.4 Short summary and discussion . . . 67

5 Topological quadrupole-like phase in an extra-site model 69
5.1 Introduction . . . 69
5.2 Model . . . 70
5.3 Band structures . . . 73
5.4 Corner states and electron density . . . 77
5.5 Wannier bands . . . 80
5.6 Short summary and future perspectives . . . 82

6 Conclusion 83

A Derivation of the effective Hamiltonian 87

Chapter 1

Background and Motivation

In this chapter, we provide a review of topological materials. While the study of topological phases originates from electronic systems, the concept of band topology extends beyond these electronic systems, and can be applied to unconventional "solids". Finally, we clarify the standpoint of our research.

1.1 Topological phase in electronic systems

The discovery of the integer quantum Hall effect (IQHE) and the subsequent development of topological insulator theories have profoundly influenced condensed matter physics. These phenomena represent a bridge between quantum mechanics and topology. In this section, we briefly review topological phases in electronic systems.

1.1.1 Quantum Hall insulators

The IQHE is a quantum mechanical phenomenon observed in two-dimensional electron systems subjected to strong magnetic fields [1, 2]. This effect was first identified in experiments involving two-dimensional electron gases formed at semiconductor heterojunction surfaces [1]. Since its discovery, the IQHE has been extensively studied as a profound link between topology and quantum mechanics in physics [3].

Within specific ranges of magnetic field strength at low temperatures, the longitudinal conductivity vanishes, $\sigma_{xx} = 0$, while the Hall conductivity is quantized in integer multiples of e^2/h:

$$\sigma_{xy} = \frac{e^2}{h} C. \tag{1.1}$$

Here e is the elementary charge, h is Planck's constant, and the integer C corresponds to the filling factor of the Landau levels. This quantization is universal, remaining independent of system-specific details like sample size or geometry.

The mechanism underlying this quantized Hall conductivity lies in the concept of band topology. In two-dimensional systems, the band structure can be represented as a mapping from the crystal momentum, $\boldsymbol{k}$ (defined on a torus), to the Bloch Hamiltonian $H(\boldsymbol{k})$. Gapped band structures are topologically classified based on equivalence classes of $H(\boldsymbol{k})$, which can be continuously deformed into one another without closing the energy gap. In the absence of the time-reversal symmetry, the topological nature of such classes is characterized by a topological invariant, known as the (first) Chern number, and the above integer C is expressed as

$$C = \sum_{n} \mathrm{ch}_n. \tag{1.2}$$

Here the quantity ch_n, the Chern number of the n-th band, is an integer, and the summation n extends over all states below the Fermi level. This relationship is rooted in reference [4, 5], known as the TKNN formula. The Chern number is originated in fiber bundles theory [3], and, in this case, can be expressed in terms of Berry phase [6], i.e.,

$$\mathrm{ch}_n = \int_{\mathrm{BZ}} \frac{d^2\boldsymbol{k}}{2\pi} b_n^z(\boldsymbol{k}), \quad b_n^z(\boldsymbol{k}) := \left(\frac{\partial a_n^y(\boldsymbol{k})}{\partial k_x} - \frac{\partial a_n^x(\boldsymbol{k})}{\partial k_y} \right), \tag{1.3}$$

where $b_n^z(\boldsymbol{k})$ is known as the Berry curvature, and $\boldsymbol{a}_n(\boldsymbol{k})$, known as the Berry connection, is defined as

$$\boldsymbol{a}_n(\boldsymbol{k}) := -i \left\langle u_n(\boldsymbol{k}) \right| \nabla_{\boldsymbol{k}} \left| u_n(\boldsymbol{k}) \right\rangle . \tag{1.4}$$

Here $|u_n(\boldsymbol{k})\rangle$ is the periodic part of the Bloch wavefunction. Although the above discussion of Hall conductivity and the Chern number has been conducted using only bulk information, it is known that the integer C corresponds to the number of edge states localized at the system's boundaries (bulk-edge correspondence [7, 8]). Consequently, when C is nonzero, chiral, gapless edge states emerge.

We have discussed setups involving two-dimensional electron systems under an external magnetic field. In 1988, however, Haldane proposed that the quantum Hall effect can also be realized in the absence of such fields, i.e. without the Landau levels [9]. The model introduced by Haldane is defined on a honeycomb lattice, and its Hamiltonian in the second-quantized form is given by

$$H_{\mathrm{Haldane}} = \sum_{i} \Delta \epsilon_i c_i^\dagger c_i + \sum_{\langle i,j \rangle} t_1 c_i^\dagger c_j + \sum_{\langle\langle i,j \rangle\rangle} e^{i\varphi} t_2 \nu_{ij} c_i^\dagger c_j. \tag{1.5}$$

Here c_i ($c_i^\dagger$) is the annihilation (creation) operator for electrons at atomic site i. $\epsilon_i = \pm 1$ As shown in the Figure 1.1(a), each site on the honeycomb lattice is classified into white sites (A sites) and gray sites (B sites). Each A site has an onsite potential Δ (i.e. $\epsilon_i = 1$), while each B site has an onsite potential $-\Delta$ (i.e. $\epsilon_i = -1$). t_1 is the nearest-neighbor (NN) hopping term, where $\langle i, j\rangle$ denotes a pair of the NN sites i and j. Similarly, $e^{i\varphi}t_2$ describes the next-nearest-neighbor (NNN) hopping term, where $\langle\langle i, j\rangle\rangle$ denotes a pair of the NNN sites i and j. The NNN hopping term is assigned a factor ν_{ij}, where $\nu_{ij} = +1$ if the hopping follows the direction of the arrows in the hexagon shown in Figure 1.1(a), and $\nu_{ij} = -1$ if the hopping occurs in the opposite direction. In momentum space, the Hamiltonian is expressed as

$$H_{\text{Haldane}}(\boldsymbol{k}) = \begin{pmatrix} R_3(\boldsymbol{k}) & R_1(\boldsymbol{k}) - iR_2(\boldsymbol{k}) \\ R_1(\boldsymbol{k}) + iR_2(\boldsymbol{k}) & -R_3(\boldsymbol{k}) \end{pmatrix}, \tag{1.6}$$

where

$$R_1(\boldsymbol{k}) := t_1(1 + \cos(\boldsymbol{k} \cdot (\boldsymbol{a}_1 + \boldsymbol{a}_2)) + \cos(\boldsymbol{k} \cdot \boldsymbol{a}_2)), \tag{1.7}$$

$$R_2(\boldsymbol{k}) := t_1(\sin(\boldsymbol{k} \cdot (\boldsymbol{a}_1 + \boldsymbol{a}_2)) + \sin(\boldsymbol{k} \cdot \boldsymbol{a}_2)), \tag{1.8}$$

$$R_3(\boldsymbol{k}) := \Delta + 2t_2 \sin(\varphi)(\sin(\boldsymbol{k} \cdot (\boldsymbol{a}_1 - \boldsymbol{a}_2)) - \sin(\boldsymbol{k} \cdot \boldsymbol{a}_1) - \sin(\boldsymbol{k} \cdot \boldsymbol{a}_2)). \tag{1.9}$$

Here the unit vectors are $\boldsymbol{a}_1 = a_0(1, 0)^T$ and $\boldsymbol{a}_2 = a_0(-1/2, \sqrt{3}/2)^T$, where we denote the lattice constant as a_0. When $t_2 = 0$, this Hamiltonian reduces to a minimal model used to describe nonmagnetic systems, such as monolayer graphene ($\Delta = 0$) or boron nitride ($\Delta \neq 0$). However, when $t_2 \neq 0$, the phase of the hopping term introduces a sign change via complex conjugation, and thus breaks time-reversal symmetry. In this case, the phase diagram of the topological phases in this model has been determined (see FIG. 1.1(b)), and it is known that the Chern number takes finite values in the parameter regions satisfying

$$\left| \frac{\Delta}{t_2} \right| < 3\sqrt{3} \sin \varphi. \tag{1.10}$$

1.1.2 Quantum spin Hall insulators

In the previous subsection, we have reviewed the IQHE, where the key feature lies in the breaking of time-reversal symmetry, leading to a nonzero Chern number. This naturally prompts a question: what kinds of topological phases can arise in systems where time-reversal symmetry is preserved? A breakthrough in this field was the theoretical proposal by Kane and Mele concerning the quantum spin Hall effect (QSHE) [10].

The fundamental idea of the QSHE is to construct a system that restores time-reversal symmetry by combining two time-reversed quantum Hall insulators [10]. This scheme is naively implemented by including spin degrees of freedom and stacking two Haldane models, as depicted in FIG 1.2(a). Thus, the Hamiltonian reads

$$H_{\text{KM}} = \sum_{\langle i,j \rangle, \alpha} t_1 c^\dagger_{i\alpha} c_{j\alpha} + \sum_{\langle\langle i,j \rangle\rangle, \alpha, \beta} it_2 \nu_{ij} \sigma^z_{\alpha\beta} c^\dagger_{i\alpha} c_{j\beta}, \tag{1.11}$$

or, in momentum space,

$$H_{\text{KM}}(\boldsymbol{k}) = \begin{pmatrix} H_{\text{Haldane},\uparrow}(\boldsymbol{k}) & 0 \\ 0 & H^*_{\text{Haldane},\downarrow}(-\boldsymbol{k}) \end{pmatrix}. \tag{1.12}$$

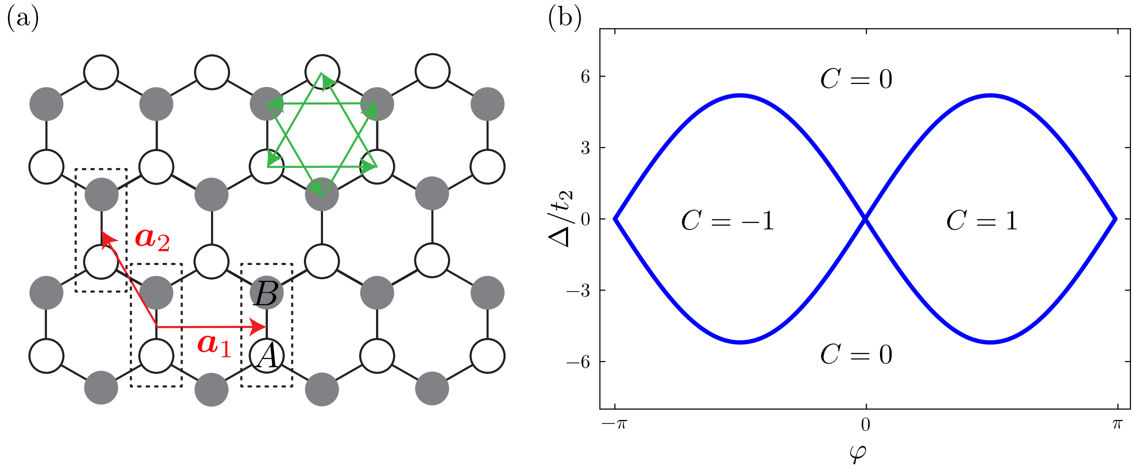

Figure 1.1: (a) Schematic illustration of the Haldane model. The on-site potential Δ $(-\Delta)$ are denoted by black (white) circle. The NN hoppings inside unit cells are denoted by t_1 (black solid lines), and the NN hoppings between unit cells are denoted by t_2 (green arrows). (b) The topological phase diagram of the Haldane model.

Here, $\alpha, \beta = \uparrow, \downarrow$ represent spin degrees of freedom, and σ^z is the z-component of the Pauli matrices. Compared to the Haldane model, this system can be understood as introducing intrinsic spin-orbit coupling into graphene ($\Delta = 0$ and $\varphi = \pi/2$) , which opens a gap at the Dirac cone. It should be noted that this system preserves time-reversal symmetry, i.e.

$$T^{-1} H_{\mathrm{KM}}(-\boldsymbol{k}) T = H_{\mathrm{KM}}(\boldsymbol{k}), \tag{1.13}$$

where

$$T = -i s_y K = \begin{pmatrix} 0 & -I_{2\times2} \\ I_{2\times2} & 0 \end{pmatrix} K. \tag{1.14}$$

Here, s_y is the y-component of spin operator, K is the complex conjugate operator. Moreover, since the system combines two Haldane models, it is expected to exhibit helical edge states, where spin-up and spin-down currents flow in opposite directions in equal amounts. Indeed, as shown in FIG 1.2 (b), numerical calculations with open boundary conditions confirm the presence of gapless energy dispersions at zero energy, corresponding to helical edge states. In addition, the spin Hall conductivity in this model is quantized, satisfying

$$\sigma^s_{xy} = \frac{e}{2\pi}. \tag{1.15}$$

In topological classification, the Chern number $C_\uparrow$ $(C_\downarrow)$ can be defined separately for the spin-up (spin-down) sector. By combining these, the $\mathbb{Z}_2$ invariant can be introduced

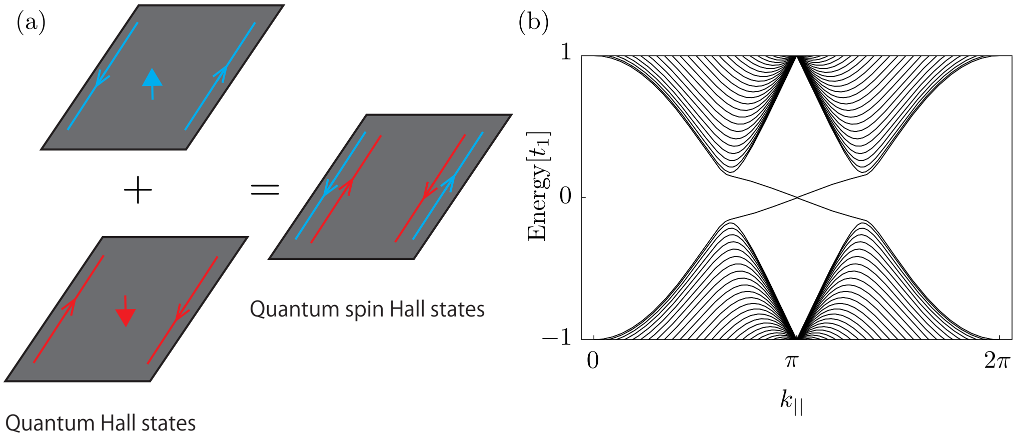

Figure 1.2: (a) Schematic illustration of the quantum spin Hall insulators. A time-reversal-invariant quantum spin Hall insulator can be constructed by pairing a quantum Hall insulator of spin-up electrons with its time-reversed counterpart for spin-down electrons. (b) The energy band structure of a quantum spin Hall insulator under open boundary conditions with $t_2 = 0.03t_1$ and $a_0 = 1$, calculated for a zigzag edge configuration, in which the boundary runs along one of the crystallographic directions of the honeycomb lattice, exposing one type of sublattice atoms at the edge.

as

$$\nu = \frac{C_\uparrow - C_\downarrow}{2} \mod 2. \tag{1.16}$$

This $\mathbb{Z}_2$ invariant distinguishes topologically trivial and nontrivial phases, where $\nu = 1$ corresponds to a topological insulator (quantum spin Hall phase), and $\nu = 0$ corresponds to a trivial insulator.

Kane and Mele's work [10, 11] was pivotal in demonstrating that insulators with time-reversal symmetry could possess nontrivial band topology. However, experimental verification of their theory in real graphene was challenging due to the weak spin-orbit interaction in graphene. Despite this difficulty, the concept of time-reversal-symmetric topological phases turns out to be experimentally accessible. In 2006, Bernevig, Hughes, and Zhang (BHZ) proposed a practical model (BHZ model) [12] based on the band structure of HgTe, which is a zero-gap semiconductor. They showed that such a system could exhibit nontrivial $\mathbb{Z}_2$ topology. This was experimentally confirmed in a CdTe/HgTe/CdTe quantum well structure [13], where the 2D electron system in HgTe forms a gapped topological phase, leading to the emergence of 1D edge states.

The idea of quantum spin Hall insulators has also been extended to 3D systems [14, 15]. In fact, diamond lattice models and Bi_2Se_3-based systems have been proposed in theoretical framework [16]. Experimentally, the surface Dirac cone, which is characteristic surface states of 3D $\mathbb{Z}_2$ topological phases, has been confirmed in several materials, such as Bi_2Se_3, Bi_2Te_3, Sb_2Te_3, using angle-resolved photoemission spectroscopy (ARPES[1]) [17, 18, 19].

1.1.3 Topological phase in one-dimensional systems

As anothor concrete example of topological insulators, we also introduce the Su-Schrieffer-Heeger (SSH) model [20], which is a minimal one-dimensional lattice model describing the electronic states of polyacetylene. As shown in FIG. 1.3, this model is characterized by alternating hopping strengths. Denoting the intra-unit-cell hopping by t_1 and the inter-unit-cell hopping by t_2, the Hamiltonian is expressed as

$$H_{\mathrm{SSH}} = \sum_i t_1(c_{iA}^\dagger c_{iB} + \mathrm{h.c.}) + \sum_i t_2(c_{iB}^\dagger c_{i+1A} + \mathrm{h.c.}). \tag{1.17}$$

Here, i labels the unit cells. Within the unit cell, we denote the left sublattice as A and the right sublattice as B. The Bloch Hamiltonian is given by

$$H_{\mathrm{SSH}}(k_x) = \begin{pmatrix} 0 & t_1 + t_2 e^{-ik_x} \\ t_1 + t_2 e^{ik_x} & 0 \end{pmatrix}. \tag{1.18}$$

Here, the lattice constant a_0 is set to $a_0 = 1$. In the SSH model, hoppings exist only between different sublattices, ensuring the presence of sublattice symmetry. This symmetry is essential for topological classification of SSH model (see Chapter 2).

To understand how edge states emerge, we impose open boundary conditions and examine specific cases. The topological classification will be addressed in Chapter 2; for now, let us develop an intuitive understanding of the presence of edge states. In the extreme case of $t_2 = 0$, all eigenstates split into bonding and antibonding states, resulting in a trivial insulating ground state (see FIG. 1.3(b)). In contrast, for $t_1 = 0$, isolated edge sites remain unsplit, leading to zero-energy edge modes and indicating a topologically nontrivial ground state (see FIG. 1.3(c)).

The above considerations can also be confirmed through numerical calculations. Figure 1.4 shows the energy dispersion plotted for different values of t_1 and t_2. The band gap closes at $t_1 = t_2$, and opens on $t_1 \neq t_2$, which imply that a topological phase transition between $|t_1| < |t_2|$ (non-trivial) and $|t_1| > |t_2|$ (trivial). Indeed, by computing the energy spectrum of a finite-length SSH model, we find that when $t_1 < t_2$, in-gap states appear at zero energy (FIG. 1.5(a)). These states are doubly degenerate, and their spatial distributions show that one eigenstate is localized at the left edge (FIG. 1.5(b)), while the other is localized at the right edge (FIG. 1.5(c)), confirming the presence of edge states.

---

[1] Angle-resolved photoemission spectroscopy (ARPES) is an experimental technique that provides direct insight into the distribution of electrons in the momentum space of a solid, specifically the density of single-particle electronic excitations. As an improvement of conventional photoemission spectroscopy, ARPES involves analyzing photoelectrons emitted when the sample is exposed to soft X-rays. This technique is considered one of the most direct methods for studying the electronic structure of solid surfaces.

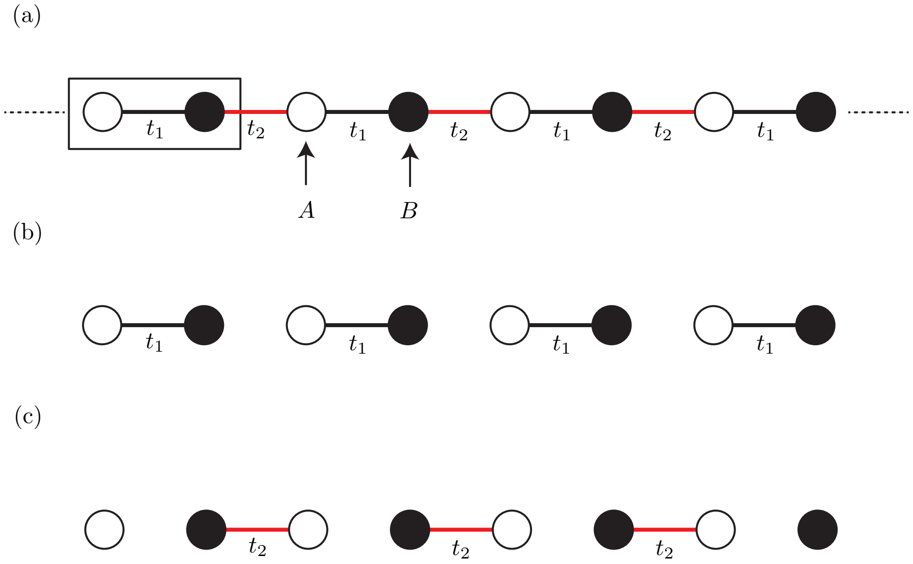

Figure 1.3: (a) Schematic illustration of the SSH model. The unit cell, indicated by a rectangle in the figure, consists of one A and one B sublattice site. The intra-unit-cell hoppings are denoted by t_1 (black solid lines), and the inter-unit-cell hoppings between unit cells are denoted by t_2 (red solid lines). (b) For the case where $t_2 = 0$. (c) For the case where $t_1 = 0$.

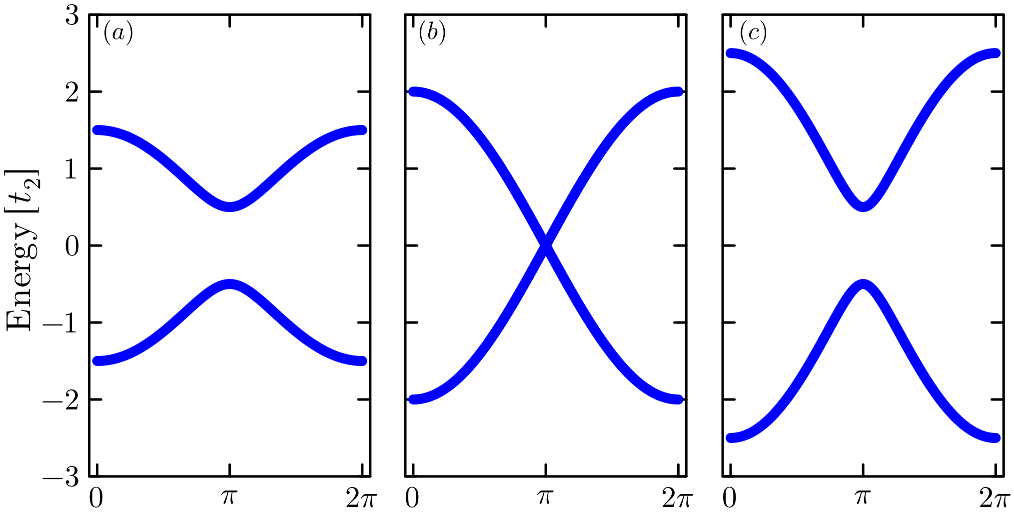

Figure 1.4: Energy dispersions for the SSH model given by Eq. (1.18): (a) $t_1 = 0.5t_2$, (b) $t_1 = t_2$, (c) $t_1 = 1.5t_2$.

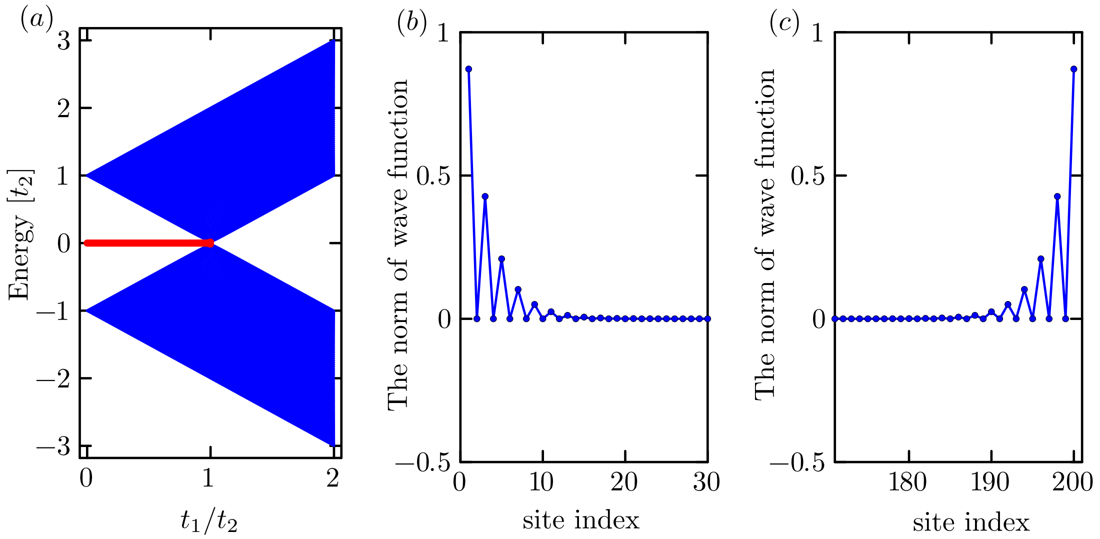

Figure 1.5: (a) the energy spectrum of the SSH model with open boundaries, plotted as a function of t_1/t_2. (b, c) the spatial distribution of the zero-energy states at $t_1 = 0.5t_2$. In all panels, the numerical calculations are performed for a system with 100 unit cells (200 sites).

1.1.4 Topological crystalline insulators

Topological crystalline insulators (TCIs) extend the concept of topological phases by utilizing crystalline symmetries, such as mirror or rotational symmetries, to protect edge states. Unlike quantum spin Hall states, which rely only on time-reversal symmetry, TCIs are characterized by symmetry-protected edge states that depend on the underlying crystal structure.

The theoretical framework for TCIs was first established by considering the role of mirror Chern numbers, which generalize the topological invariants in systems with mirror symmetry [21]. Indeed, Hsieh et al. [22] proposed SnTe-based model as a candidate material for TCI behavior due to its strong spin-orbit coupling and mirror-symmetric crystal structure. In addition, experimental confirmation [23] came from ARPES measurements, which revealed gapless surface states on specific crystal planes of SnTe and related compounds.

In the rest of this subsection, as an example of TCIs, we review Wu-Hu model [24], which is a key concept exploited in chapter 3 and chapter 4. This model is constructed on a honeycomb lattice, and Wu and Hu adopt a hexagonal unit cell as its fundamental building block. Indeed, the model includes six sublattices per unit cell, as depicted in FIG. 1.6. The hopping scheme involves two types of processes: intra-hexagon hopping, which links NN sites within the same hexagon, and inter-hexagon hopping, which connects NN sites across different hexagons. Then, the Hamiltonian reads

$$H_{\mathrm{Wu-Hu}} = \sum_{\langle i,j\rangle} t_0 c_i^\dagger c_j + \sum_{\langle i',j'\rangle} t_1 c_{i'}^\dagger c_{j'}. \tag{1.19}$$

Here t_0 and t_1 represent the intra- and inter-hexagon hopping respectively, and we define $e_l(\boldsymbol{k}) := e^{i\boldsymbol{k}\cdot\boldsymbol{a}_l}$ $(l = 1, 2)$. The unit vectors for the modulated honeycomb lattice are $\boldsymbol{a}_1 = (3a_0/2, \sqrt{3}a_0/2)^T$ and $\boldsymbol{a}_2 = (-3a_0/2, \sqrt{3}a_0/2)^T$. In momentum space, the Bloch Hamiltonian becomes

$$H_{\mathrm{Wu-Hu}}(\boldsymbol{k}) = \begin{pmatrix} 0 & D(\boldsymbol{k}) \\ D^\dagger(\boldsymbol{k}) & 0 \end{pmatrix}, \tag{1.20}$$

$$D(\boldsymbol{k}) = \begin{pmatrix} t_1 e_1^*(\boldsymbol{k}) e_2^*(\boldsymbol{k}) & t_0 & t_0 \\ t_0 & t_1 e_1(\boldsymbol{k}) & t_0 \\ t_0 & t_0 & t_1 e_2(\boldsymbol{k}) \end{pmatrix}. \tag{1.21}$$

For later convenience, we first focus on the eigenstates of $H_{\mathrm{Wu-Hu}}(\boldsymbol{k} = \boldsymbol{0})$. These eigenstates can be understood in terms of the irreducible representations of group theory [25]. Since this model possesses the crystalline point group symmetry $\mathrm{C_{6v}}$, the eigenfunctions at the Γ point become the basis of its irreducible representation. Thus, the six eigenstates decompose into four irreducible representations: A_1, B_2, E_1, E_2, which correspond to physical orbitals s, $f_{y(3x^2-y^2)}$, $p_{x,y}$, $d_{x^2-y^2,xy}$, respectively. The explicit expression for these orbitals are given as

$$\begin{aligned} |s\rangle &= (1,1,1,1,1,1)^T/\sqrt{6}, \\ |f_{y(3x^2-y^2)}\rangle &= (-1,-1,-1,1,1,1)^T/\sqrt{6}, \\ |p_x\rangle &= (0,-1,1,0,1,-1)^T/2, \\ |p_y\rangle &= (2,-1,-1,-2,1,1)^T/2\sqrt{3}, \\ |d_{x^2-y^2}\rangle &= (-2,1,1,-2,1,1)^T/2\sqrt{3}, \\ |d_{xy}\rangle &= (0,1,-1,0,1,-1)^T/2. \end{aligned} \tag{1.22}$$

Furthermore, using these orbitals, we construct pseudospin modes as follows:

$$|p_\pm\rangle = \frac{1}{\sqrt{2}}(p_x \pm i p_y), \quad |d_\pm\rangle = \frac{1}{\sqrt{2}}(d_{x^2-y^2} \pm i d_{xy}). \tag{1.23}$$

Here the $+$ $(-)$ sign corresponds to the pseudospin up (down) state [24]. These pseudospin modes are directly related to the current density within a hexagon. In fact, in this case, the current density between two sites inside the hexagon is given by $I_{ij} = (i/\hbar)[t_0 c_i^\dagger c_j - t_0 c_j^\dagger c_i]$ (i, j are site indices), and the current distribution evaluated by using the pseudospin up (down) state exhibits a anticlockwise (clockwise) circulating current, as shown in FIG. 1.7.

Let us now consider the band structures. When $t_1 = t_0$, this model takes a form of the minimal model of graphene. The Dirac cones initially located at the K and K'

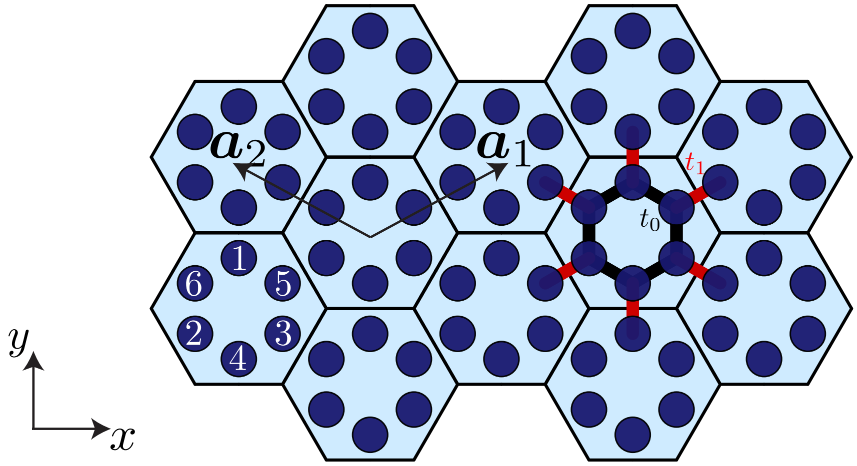

Figure 1.6: Schematic illustration of the Wu-Hu model. The unit cell consists of six sites, where the intra-hexagon hopping is denoted by t_0 (black solid lines) and the inter-hexagon hopping is denoted by t_1 (red solid lines).

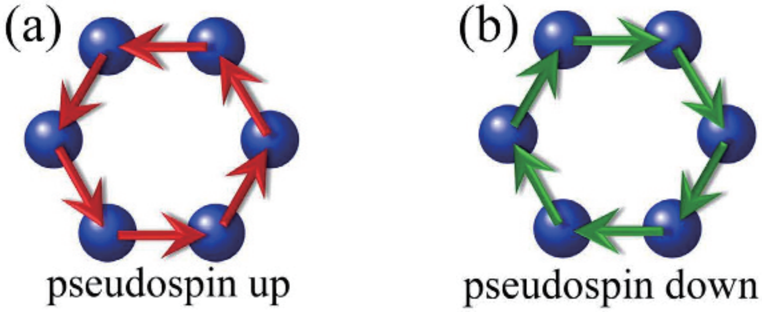

Figure 1.7: Current densities of (a) the pseudospin-up states and (b) pseudospin-down states respectively. These figures are cited from [24].

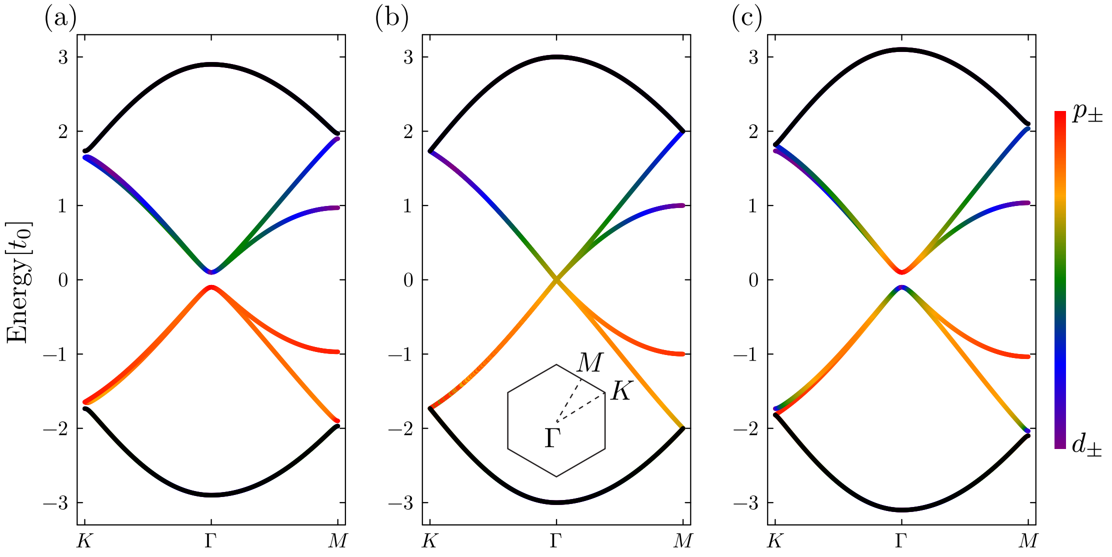

Figure 1.8: Energy dispersions for the system given by Eq.(1.20). (a) $t_1 = 0.9t_0$, (b) $t_1 = t_0$, (c) $t_1 = 1.1t_0$. The color maps are for the values of $|\langle u^n(\boldsymbol{k})|d_+\rangle|$. $|p_\pm\rangle$ and $|d_\pm\rangle$ are pseudo-spin modes.

points are folded onto the Γ point, resulting in the appearance of the double Dirac cone at Γ point (FIG. 1.8 (b)). Next, when $t_1 \neq t_0$, this modulation breaks the degeneracy of the Dirac cone, and band gaps open at the Γ point (FIG. 1.8 (a, c)). From the viewpoint of group theory, the four states near the zero energy originate from the representation E_1 and E_2. As shown in Fig. 1.8, the band inversion, which means the swapping of E_1 and E_2, occurs between $t_1 = 0.9t_0$ and $t_1 = 1.1t_0$. This can also be analyzed from the perspective of the effective model. By using $\{|p_\pm\rangle, |d_\pm\rangle\}$ as a basis and expanding the Hamiltonian to first order in momentum [26], the effective Hamiltonian becomes

$$\mathcal{H}^{(\mathrm{eff})}_{\mathrm{Wu-Hu}}(k_x, k_y) \simeq \begin{pmatrix} \mathcal{H}^{(\mathrm{eff})}_{\mathrm{Wu-Hu},+}(k_x, k_y) & 0 \\ 0 & \mathcal{H}^{(\mathrm{eff})}_{\mathrm{Wu-Hu},-}(k_x, k_y) \end{pmatrix}, \tag{1.24}$$

where

$$\mathcal{H}^{(\mathrm{eff})}_{\mathrm{Wu-Hu},\pm}(k_x, k_y) := (t_0 - t_1)\sigma_z + \frac{t_1|\boldsymbol{a}_1|}{2}(\pm k_x\sigma_x + k_y\sigma_y). \tag{1.25}$$

which takes the form of a Dirac Hamiltonian. Here σ_i $(i = x, y, z)$ are Pauli matrices. The parameter $m := t_0 - t_1$ functions as the Dirac mass term, governing the bandgap and indicating the transition between topologically trivial and non-trivial phases. Furthermore, the effective Hamiltonian satisfies the pseudo-time-reversal symmetry

$$\mathcal{T}^{-1}\mathcal{H}^{(\mathrm{eff})}_{\mathrm{Wu-Hu}}(-k_x, -k_y)\mathcal{T} = \mathcal{H}^{(\mathrm{eff})}_{\mathrm{Wu-Hu}}(k_x, k_y), \tag{1.26}$$

where

$$\mathcal{T} = \begin{pmatrix} 0 & -I_{2\times 2} \\ I_{2\times 2} & 0 \end{pmatrix} K. \tag{1.27}$$

This symmetry resembles the time-reversal symmetry of QSHE in Eq.(1.13), and suggests the realization of quantum pseudo spin Hall states.

To examine the emergence of edge states, let us also consider the boundary. Here, let the Dirac mass be uniform along x-axis, making k_x a good quantum number. On the other hand, in y-axis, we introduce the boundary at $y = 0$, and set $t_0 - t_1 = m_0$ for $y > 0$ and $t_0 - t_1 = -m_0$ for $y < 0$. In addition, we apply the continuous approximation $k_y \to -i\partial_y$. Then, the eigenvalue equation of $\mathcal{H}^{(\mathrm{eff})}_{\mathrm{Wu-Hu},\pm}$ is

$$\begin{pmatrix} m_0 \mathrm{sgn}(y) & v(\pm k_x - \partial_y) \\ v(\pm k_x + \partial_y) & -m_0 \mathrm{sgn}(y) \end{pmatrix} \begin{pmatrix} \phi_1 \\ \phi_2 \end{pmatrix} = E \begin{pmatrix} \phi_1 \\ \phi_2 \end{pmatrix}, \tag{1.28}$$

where $v := t_1 |\boldsymbol{a}_1|/2$. Their physical solutions are given by

$$E_\pm = \pm v k_x, \quad \begin{pmatrix} \phi_{\pm,1} \\ \phi_{\pm,2} \end{pmatrix} = \begin{pmatrix} 1 \\ -1 \end{pmatrix} \exp\left(-\frac{m_0}{v}|y|\right). \tag{1.29}$$

These results suggest that, when interpreting the eigenstate from $\mathcal{H}^{(\mathrm{eff})}_{\mathrm{Wu-Hu},+}$ as pseudo spin-up and $\mathcal{H}^{(\mathrm{eff})}_{\mathrm{Wu-Hu},-}$ as pseudo spin-down, the propagation direction depends on the pseudo spin orientation (see FIG. 1.9). Thus, from the viewpoint of edge states, it has been verified that the quantum pseudo spin state is successfully implemented.

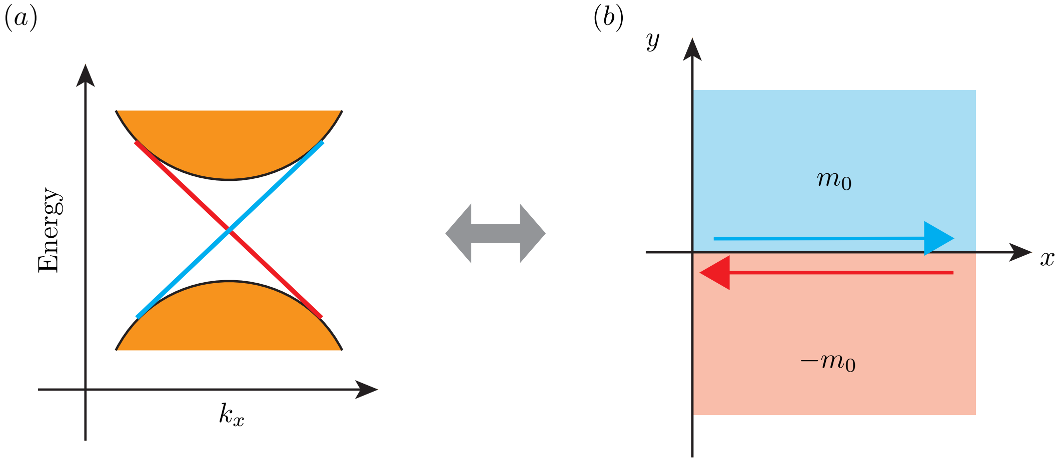

Figure 1.9: (a) Schematic illustration of the edge band structure obtained from Eq.(1.29). (b) Schematic illustration of the edge states. The propagation directions of the edge states are opposite, reflecting the group velocity.

The above discussion is based on the effective model using the Dirac Hamiltonian. In general, however, topological phases are fundamentally characterized by the global structure of the Bloch wavefunctions, and often expressed via topological indices. In this model, sublattice symmetry allows the definition of a mirror winding number [27], complementing the Dirac equation analysis (see also Chater 2).

While the present discussion is framed within a tight-binding model, this methodology applies to other systems beyond electronic systems. In fact, for systems with the same symmetry, an effective continuum model can be constructed based on the E_1, E_2 states [28], leading to the Dirac equation. This perspective is particularly significant when one analyzes the photonic crystal analog of the Wu-Hu model, which will be discussed in Sec. 1.2.3.

1.1.5 Higher-order topological insulators

We have reviewed the concept of topological insulators. A key feature of a d-dimensional topological insulators is the presence of gapless boundary states in $d-1$ dimensions. Recently, however, the concept of topological insulators has been expanded to include a new class known as higher-order topological insulators (HOTIs) [29, 30, 31, 32, 33, 34, 35]. Unlike conventional topological insulators, d-dimensional HOTI lack gapless boundary states in $d-1$ dimensions. Instead, they exhibit localized states on boundaries that are two or more dimensions lower than the bulk. For instance, systems with states localized in $d-2$ dimensions are d-dimensional second-order topological insulators (see FIG. 1.10 (b)), while those with states in $d-3$ dimensions are called d-dimensional third-order topological insulators (see FIG. 1.10 (c)). The boundary states are also categorized by their dimensionality: 0-dimensional zero-energy states are known as corner states [29], and 1-dimensional boundary states are referred to as hinge states [36].

There are two main approaches to constructing HOTIs. The first involves extending SSH model to higher dimensions [29, 33, 37, 38]. In this class of systems, a quantity known as the Wannier center becomes quantized, playing the role of a topological insulators. These systems are often referred to as Wannier-type HOTIs [37, 38]. The second approach involves adding a new mass term to the Hamiltonian of a topological insulator [30, 32, 39, 40]. For example, it is known that introducing a mass term by applying a tilted magnetic field to the BHZ model enables the implementation of a 3-dimensional second-order topological insulator [40].

In the rest of this subsection, as an example of Wannier-type HOTIs, we review Benalcazar-Bernevig-Hughes (BBH) model [29], which is a key concept discussed in chapter 5. Benalcazar et al. consider a two-dimensional tight-binding model on a square lattice with NN hoppings. The primitive unit cell is a square containing four sites. As NN hoppings, they introduced both intra-square hopping γ and inter-square hopping λ, as depicted in FIG 1.11. Here, to make this system an insulator, they assigned a negative sign to the hopping terms to ensure that the accumulated phase around each plaquette sums to π, effectively introducing a π-flux per plaquette in the

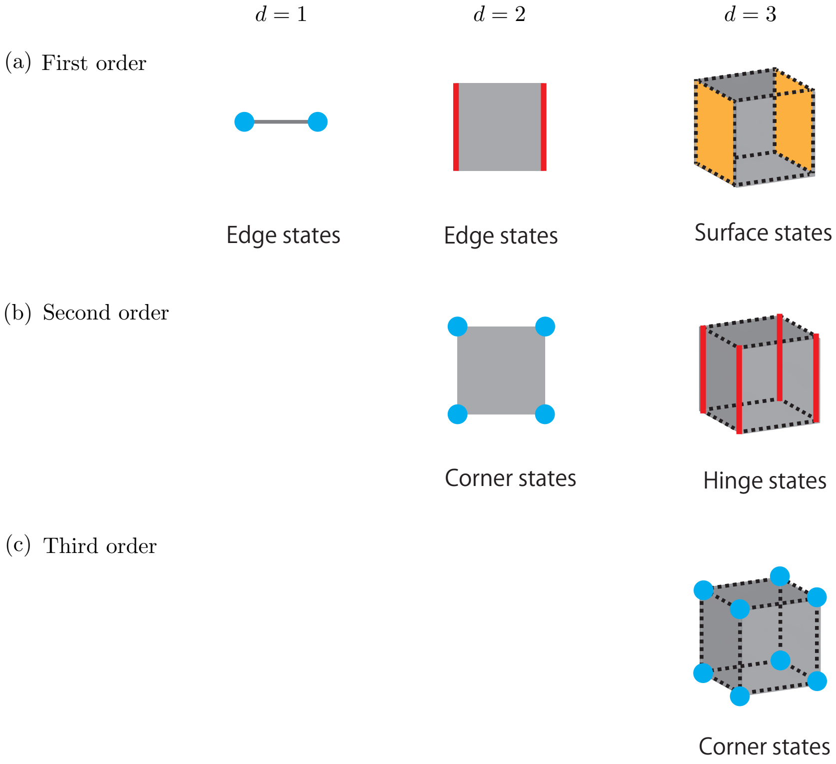

Figure 1.10: Schematic illustration of HOTIs. (a) First order, (b) second order, (c) third order HOTIs.

system.

The emergence of corner states can be grasped intuitively, much like in the SSH model. To preliminarily investigate corner states, we consider a system under open boundary conditions. We use the parameter γ/λ to characterize this system. Let us first discuss the case of $\gamma/\lambda \to \infty$ $(\lambda \to 0)$. In this case, energy eigenstates within each unit cell split into bonding and antibonding states, resulting in a trivial insulating ground state where all bonding states are occupied. Conversely, when, $\gamma/\lambda \to 0$ $(\gamma \to 0)$ isolated sites appear at the corners of the system, and these sites exhibit no energy splitting. This leads to the presence of zero-energy modes at the corners, indicating a topologically nontrivial ground state.

Although we have focused on the extreme cases of $\gamma/\lambda \to 0, \infty$, the topological properties of the system should remain invariant under small changes to the value of γ/λ. Therefore, the next task is to determine where topological phase transition between $\gamma/\lambda \to 0$ and $\gamma/\lambda \to \infty$ occurs, that is, where the band gap closes. The Bloch Hamiltonian of this model reads

$$H_{\mathrm{BBH}}(\boldsymbol{k}) = (\gamma + \lambda\cos(\boldsymbol{k}\cdot\boldsymbol{a}_1))\Gamma_4 + \lambda\sin(\boldsymbol{k}\cdot\boldsymbol{a}_1)\Gamma_3 + (\gamma + \lambda\cos(\boldsymbol{k}\cdot\boldsymbol{a}_2))\Gamma_2 + \lambda\sin(\boldsymbol{k}\cdot\boldsymbol{a}_2)\Gamma_1. \tag{1.30}$$

Here the unit vectors are $\boldsymbol{a}_1 = a_0(1,0)^T$ and $\boldsymbol{a}_2 = a_0(0,1)^T$, and we use Γ matrices, which is defined as

$$\Gamma_i := \begin{pmatrix} 0 & \sigma_i \\ -\sigma_i & 0 \end{pmatrix}. \tag{1.31}$$

The eigenenergies are

$$E_\pm(\boldsymbol{k}) = \pm\sqrt{2\lambda^2 + 2\gamma^2 + 2\lambda\gamma[\cos(\boldsymbol{k}\cdot\boldsymbol{a}_1) + \cos(\boldsymbol{k}\cdot\boldsymbol{a}_2)]} \tag{1.32}$$

with twofold degenerate, as shown in FIG. 1.12. From the expression for the energy eigenvalues, it can be seen that the bulk energy gap arises at the X point for $\gamma/\lambda = 1$ (and at the Γ point for $\gamma/\lambda = -1$). This suggests that the topological phase transitions occur at $\gamma/\lambda = \pm 1$. Indeed, this is confirmed numerically, as shown in FIG. 1.12, where band inversion occurs at $\gamma/\lambda = 1$.

The assertion for the emergence of topological phase can also be verified through numerical calculations for a system with open boundary conditions in both the x- and y-directions. By computing the energy eigenvalues and eigenstates of this quantum many-body system, it is found that, for $|\gamma/\lambda| < 1$, zero-energy states localized at the corners appear within the band gap (FIG. 1.13 (a)). Additionally, when $|\gamma/\lambda| < 1$, this system exhibits a quantized corner charge (FIG. 1.13 (b)), while, for $|\gamma/\lambda| > 1$, the corner charge disappears. Thus, we refer to the phase with $-1 < \gamma/\lambda < 1$ as the nontrivial quadrupole phase and the phase with $|\gamma/\lambda| > 1$ as the trivial quadrupole phase.

The remaining issue is how to characterize the band topology of this system. For this purpose, a framework involving the Wilson loop is available (see Chapter 2).

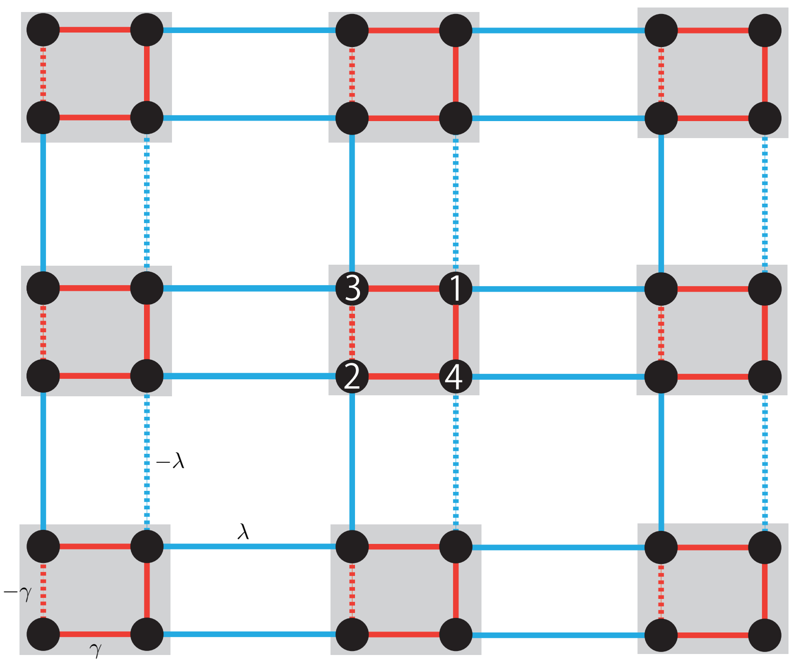

Figure 1.11: Schematic illustration of the BBH model. The intra-square hoppings are denoted by γ , and the inter-square hoppings are denoted by λ. The sign flip of the hoppings are indicated by dashed lines.

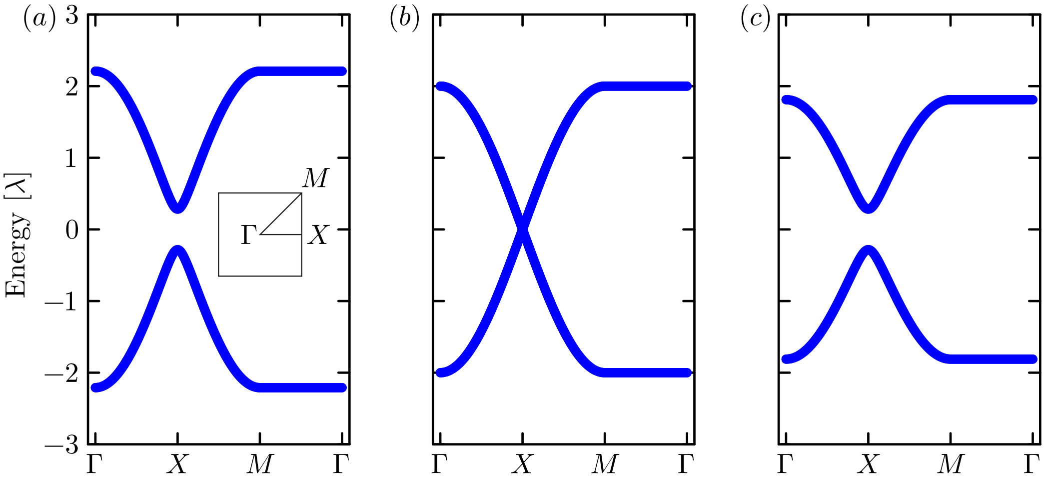

Figure 1.12: Energy dispersions for the BBH model given by Eq. (1.32). (a) $\gamma = 1.2\lambda$. (b) $\gamma = \lambda$. (c) $\gamma = 0.8\lambda$.

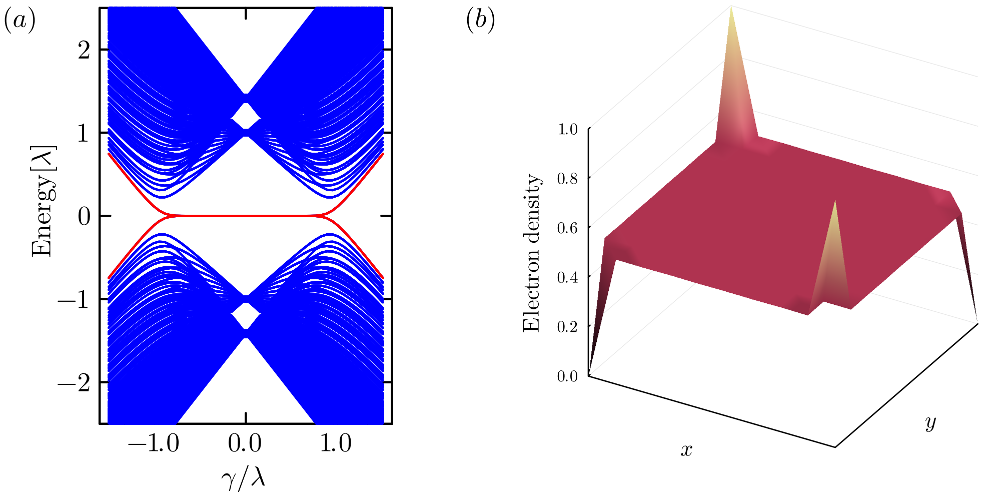

Figure 1.13: (a) The energy spectrum of the BBH model with open boundaries, plotted as a function of γ/λ. The calculation is performed for a 20×20 unit cell system. For $|\gamma/\lambda| < 1$, zero-energy states appear, as indicated by the red lines. (b) The spatial distribution of the electron density at $\gamma = 10^{-3}\lambda$. The calculation is performed for a 5×5 unit cell system and under the assumption of half-filling, where there is one electron per site.

1.2 Topological phase in unconventional “solids”

Topological physics has provided deep insights into the properties of various physical systems by connecting their global features to local behavior through topological invariants. While initially developed for quantum many-body systems, the principles of topological physics have been extended to unconventional settings. There are several key motivations for studying topological phases in platforms beyond conventional solid-state electronic systems:

- **Engineering of exotic hopping processes:**
  These systems allow the realization of complex hopping terms that are difficult to implement in solids, such as long-range tunneling, complex phase factors, and synthetic gauge fields.

- **Implementation of higher-dimensional models:**
  They enable the construction of models in dimensions that are inaccessible in real materials, for instance, through the use of synthetic dimensions to realize higher-dimensional quantum Hall effects.

- **High controllability:**
  Experimental parameters, including lattice geometry, interaction strength, and

external fields, can be precisely controlled, often without requiring extreme conditions such as cryogenic temperatures or strong magnetic fields.

- **Direct observation of edge states:**
  Unlike in electronic systems where edge states are typically detected indirectly via transport measurements, these platforms allow real-space imaging of edge modes, such as density distributions in cold atom systems and light propagation in photonic structures.

To provide a clearer understanding of these motivations, we next review such unconventional "solids" that serve as versatile platforms for realizing topological phases. The content of this section is based on the review paper [41].

1.2.1 Ultracold atomic gases

Cold atomic systems refer to gases of atoms that are cooled to extremely low temperatures using methods like laser cooling [42, 43]. Most substances, except helium, solidify near absolute zero. While cold atomic systems can temporarily exist in a metastable (supercooled) gaseous phase, if confined as a gas for a sufficiently long time, they eventually crystallize into a solid state. Research in this field focuses on understanding the metastable (supercooled) gaseous phases of cold atomic systems [44].

At these low temperatures, atoms prominently exhibit quantum mechanical behaviors, such as the wave-like nature of their motion and the superposition of their electronic states. The significance of cold atomic systems in condensed matter physics was firmly established in 1995, with the realization of Bose-Einstein condensation (BEC) in rubidium atoms [45]. BEC is known for the collective behavior of atoms acting as a macroscopic wave [42, 43]. Since then, a wide range of experiments [46, 47, 48] have investigated the properties of various atomic species by cooling them to temperatures where phenomena like BEC and Fermi degeneracy become observable.

Atoms with reduced kinetic energy (lower speeds) can be trapped using coherent laser light [49, 50, 51, 52, 53, 54]. A major milestone in this field was the development of optical lattices [52, 53], which utilize the standing waves created by interfering laser beams to periodically trap atoms. This periodic trapping structure gives rise to an energy spectrum with a band structure, similar to electrons in crystal lattices. By carefully adjusting parameters such as the laser's orientation, intensity, and phase, various lattice geometries can be achieved [55]. Thus, optical lattices serve as an exceptional platform for studying the physics of particles in lattice systems. In fact, in the context of topological materials research, optical lattices have been used to realize a variety of theoretical models [56, 57, 58, 59, 60, 61, 62, 63, 64, 65, 66, 67, 68].

A particularly notable research direction involves Floquet engineering of the Haldane model [69, 70]. This idea can be summarized as follows: Let us consider a two-dimensional honeycomb lattice that is periodically driven in a circular manner. The oscillations cause particles within the lattice to experience centrifugal forces. Indeed, if the driving frequency is ω and the magnitude of the force is F, $\boldsymbol{F}(t) = F(\cos\omega t, \sin\omega t)$

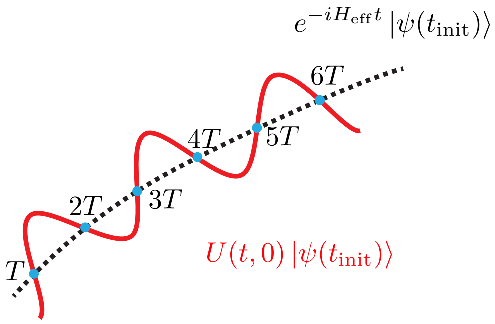

Figure 1.14: A schematic illustration of the stroboscopic picture in Floquet engineering. The red solid line schematically represents the actual dynamics in Hilbert space, while the black dashed line illustrates the effective dynamics in a simplified or reduced description.

acts on each lattice site. Then, the lattice model under this force can be described by the following Hamiltonian:

$$H(t) = \sum_{\langle i,j\rangle} J c_i^\dagger c_j + \sum_i \boldsymbol{F}(t)\cdot \boldsymbol{r}_i c_i^\dagger c_i, \tag{1.33}$$

where $\boldsymbol{r}_i$ denotes the position of site i. In general, the time evolution of this system is formally written as $U(t,0) = \mathcal{T}\exp\left(-(i/\hbar)\int_0^t dt' H(t')\right)$, where $\mathcal{T}$ is the time-ordering operator. However, in the regime of high driving frequencies, the period $T = 2\pi/\omega$ becomes the shortest timescale of this system, making the micromotion within a single cycle typically irrelevant, which can be intuitively understood as the contraction of the dynamics represented by the red lines in FIG. 1.14 into the effective dynamics indicated by the black dashed lines. Indeed, the effective dynamics of this system are governed by an effective Hamiltonian H_{eff}, which can be systematically derived through a high-frequency expansion [71, 72, 73, 74, 75] in the high-frequency limit:

$$H_{\text{eff}} := \frac{i\hbar}{T}\log U(T,0) \simeq \sum_{\langle i,j\rangle} J_{\text{eff}} c_i^\dagger c_j + \sum_{\langle\langle m,n\rangle\rangle} i\nu_{mn} J_{\text{eff}}^{\text{NNN}} c_m^\dagger c_n, \tag{1.34}$$

where $J_{\text{eff}} = J\mathcal{J}_0(Fd/\omega)$, $J_{\text{eff}}^{\text{NNN}} = (\sqrt{3}J^2/\omega)\mathcal{J}_1^2(Fd/\omega)$. Here $\mathcal{J}_{0,1}$ denote Bessel functions of the first kind and d is the lattice spacing. This effective Hamiltonian is identical to the Haldane model with $\Delta = 0$ and $\varphi = \pi/2$, as introduced in Sec. 1.1.1. Following this scheme, the Haldane model was implemented in ultracold atoms loaded into an optical lattice, with the lattice being circularly shaken by piezoelectric actuators [62].

1.2.2 Coupled cavity arrays

A cavity is a device designed to stably confine light [44], such as by placing two mirrors facing each other (see FIG. 1.15 (a)). When the reflectivity of the mirrors is perfect (i.e., 1), preventing any light from escaping, the electromagnetic field inside the cavity forms a standing wave, with discrete resonance frequencies. If the spacing between these frequencies is sufficiently large, the electromagnetic field within the cavity can be approximated as a single mode by focusing on one specific frequency. For simplicity, when the polarization degree of freedom is ignored, the Hamiltonian of a single cavity can be expressed as

$$H_{\mathrm{c}} = \omega_0 a_0^\dagger a_0. \tag{1.35}$$

Here, we adopt units where $\hbar = 1$, and a_0 ($a_0^\dagger$) is the annihilation (creation) operator of the single photon mode. When two cavities are present and no light leaks out, the Hamiltonian describing this system can be written as

$$H_{\mathrm{cc}} = \sum_{i=1,2} \omega_0 a_{i0}^\dagger a_{i0}. \tag{1.36}$$

Here, the subscripts 1 and 2 are labels used to distinguish between the cavities.

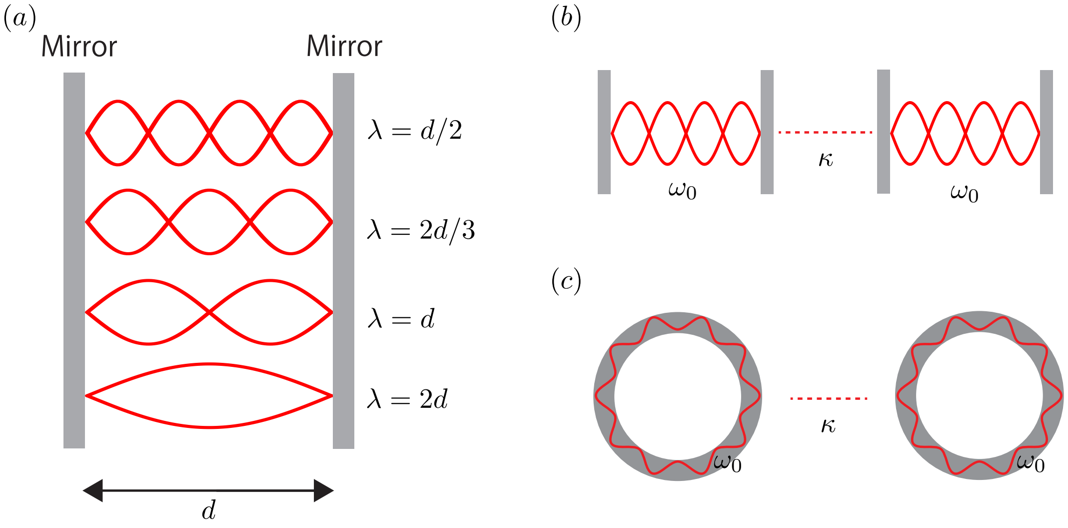

Figure 1.15: (a) Schematic illustration of an optical cavity. Two mirrors are arranged at a distance that is an integer multiple of the wavelength, confining the standing wave of light. (b) Schematic illustration of a weakly coupled optical cavity system. (c) Schematic illustration of a ring optical cavity. A ring optical cavity consists of a closed loop of optical paths formed by multiple mirrors, allowing light to circulate continuously in one direction.

Next, let us consider the case where the mirror reflectivity is less than 1, allowing light to escape, and the two resonators are weakly coupled (see FIG. 1.15 (b, c)). The treatment of electromagnetic field coupling in such a setup has been studied using coupled-mode theory [76]. When considering coupling up to the lowest order, it is known that the Hamiltonian can be expressed as

$$H_{\mathrm{cc}} = \sum_{i=1,2} \omega_0 a^\dagger_{i0} a_{i0} + \kappa (a^\dagger_{10} a_{20} + \mathrm{h.c.}), \tag{1.37}$$

where κ is a coupling constant. Furthermore, by restricting the input to coherent light, we can replace the operators with $\mathbb{C}$-number-valued expectation values α_{j0} [41], and the equations of motion for this system, derived from the Heisenberg equations, can be written as

$$i\frac{d}{dt}\begin{pmatrix}\alpha_{10}\\ \alpha_{20}\end{pmatrix} = \begin{pmatrix}\omega_0 & \kappa\\ \kappa & \omega_0\end{pmatrix}\begin{pmatrix}\alpha_{10}\\ \alpha_{20}\end{pmatrix}, \tag{1.38}$$

which is analogous to the Schrödinger equation for a two-site tight-binding model. Extending this concept, coupling N cavities results in an N-site tight-binding model. By varying the arrangement of the cavities, a wide range of lattice models can be realized, and coupled cavity arrays provide an excellent platform for studying lattice models [41].

A particularly important direction of research related to the topological phases of cavities is the study of synthetic frequency dimensions[2] [80, 81]. Let us briefly review this topic based on Ref. [80]. While the previous discussion focused on a single mode with frequency ω_0, we now consider the degrees of freedom of modes near ω_0 and denote the Hamiltonian for an N-cavity system (see FIG. 1.16 (a)) as

$$H_0 = \sum_{im} \omega_m a^\dagger_{im} a_{im} + \sum_{im} \left(\kappa a^\dagger_{im} a_{i+1m} + \mathrm{h.c.} \right). \tag{1.39}$$

where $a^\dagger_{im}$ (a_{im}) is the creation (annihilation) operator for the m-th mode at the i-th cavity, $\omega_m := \omega_0 + \Omega m$ is the frequency for the m-th resonant mode, and κ is the coupling constant. We assume that coupling occurs only between modes with the same frequency, and that all such couplings share a common coupling constant κ. Furthermore, we impose a time-periodic modulation on refractive index of cavities with frequency Ω. This modulation induces coupling between modes with frequencies differing by Ω, modifying the Hamiltonian as

$$H(t) = \sum_{im} \omega_m a^\dagger_{im} a_{im} + \sum_{im} \left(\kappa a^\dagger_{im} a_{i+1m} + 2g\cos(\Omega t + \phi_i) a^\dagger_{im} a_{im+1} + \mathrm{h.c.} \right), \tag{1.40}$$

---

[2] Here, we focus only on synthetic frequency dimensions. In general, however, the concept of synthetic dimensions is frequently employed in setups beyond optical cavity systems [77, 78, 79].

where g is the strength of modulation, and ϕ_i is the associated modulation phase at the i-th cavity. Applying the rotating wave approximation to this Hamiltonian yields an effective Hamiltonian

$$\tilde{H}(t) = \sum_{im} \left(\kappa \tilde{a}^\dagger_{im} \tilde{a}_{i+1m} + g e^{i\phi_i} \tilde{a}^\dagger_{im} \tilde{a}_{im+1} + \text{h.c.} \right), \tag{1.41}$$

Here we have defined $\tilde{a}_{im} := a_{im} e^{-i\omega_m t}$. We note that the hopping terms in this effective Hamiltonian (1.41) acquire a phase. Consequently, arranging two or more cavities in a linear configuration and considering the coupling between them enables the realization of a two-dimensional lattice model, comprising one real spatial dimension and one synthetic frequency dimension. By varying the phase ϕ_i across the cavities, it is possible to introduce a synthetic gauge flux through each plaquette (see FIG. 1.16 (b)), thereby realizing the Harper-Hofstadter model, which describes a tight-binding model under a uniform magnetic field whose effect is incorporated as Peierls phases on the hopping terms. This model provides a lattice implementation of the quantum Hall effect, capturing its characteristic topological properties. Furthermore, by arranging resonators in three real spatial dimensions and incorporating the synthetic frequency dimension, a four-dimensional lattice model can be achieved. Therefore, this concept has been used to realize a four-dimensional Harper-Hofstadter model, leading to theoretical proposals for studying the four-dimensional quantum Hall effect.

1.2.3 Photonic crystals

Photonic crystals are materials with a periodic structure, typically formed by stacking different types of dielectrics [82]. Figure 1.17 illustrates a schematic representation of a photonic crystal, where two types of dielectric materials are stacked in an alternating manner. Depending on the dimensionality of the periodic arrangement, these structures are categorized as one-dimensional, two-dimensional, or three-dimensional photonic crystals. In addition, the stacking period is commonly referred to as the lattice constant due to its analogy with solid-state systems. The lattice constant of photonic crystals is comparable to the wavelength of the electromagnetic waves involved [83, 84]. For instance, in photonic crystals operating in the visible light spectrum, the lattice constant typically ranges from 0.2μm to 0.5μm [84].

One of the most remarkable properties of photonic crystals is their ability to prohibit the propagation of light within specific frequency ranges, owing to their periodic structure [82]. This behavior can be understood by applying a concept similar to Bloch's theorem from solid-state physics. The periodicity of the photonic crystal enables the classification of electromagnetic field modes and their associated frequencies within the first Brillouin zone, forming photonic bands. Since photonic bands generally exhibit band gaps, certain frequencies of light cannot propagate through the crystal.

To make the above statement concrete, let us discuss it in the framework of Maxwell's equations. By considering the electromagnetic fields $\boldsymbol{E}(\boldsymbol{r}, t)$ and $\boldsymbol{H}(\boldsymbol{r}, t)$, which describe mesoscale degrees of freedom in the system, we examine the constraints imposed

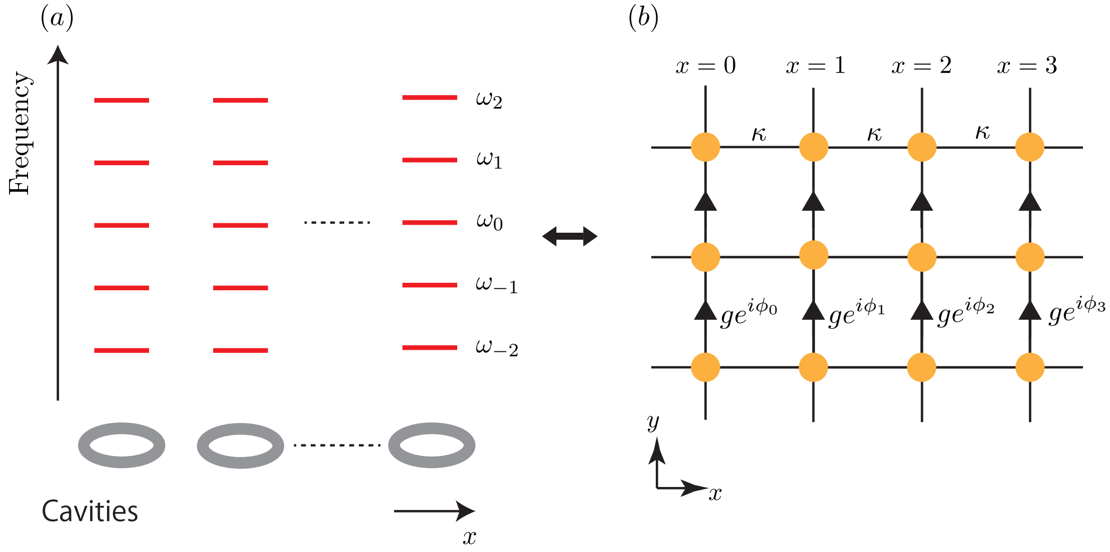

Figure 1.16: (a) Schematic illustration of the implementation of the Harper-Hofstadter model using a synthetic frequency dimension. Although the optical cavities are arranged in only one spatial dimension, careful engineering of coupling between frequency modes allows the frequency modes to be used as an additional synthetic dimension. (b) Schematic representation of the Hamiltonian Eq. (1.41) after applying the rotating wave approximation. The phase modulation in the optical cavity plays the role of the Peierls phase.

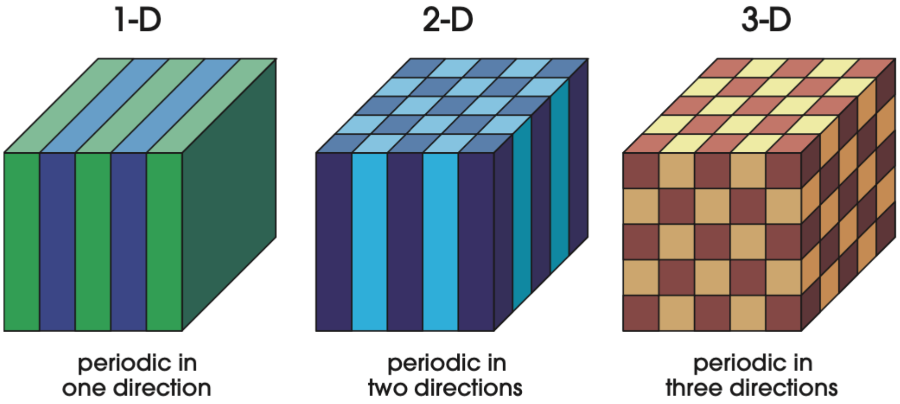

Figure 1.17: Schematic illustration of a photonic crystal. The color differences indicate variations in the dielectric constant. This figure is cited from [85]

.

on their solutions. Maxwell's equations in this context are expressed as

$$\nabla \cdot \boldsymbol{D} = 0, \quad \nabla \cdot \boldsymbol{B} = 0, \tag{1.42}$$

$$\nabla \times \boldsymbol{E} = -\frac{\partial \boldsymbol{B}}{\partial t}, \quad \nabla \times \boldsymbol{H} = \frac{\partial \boldsymbol{D}}{\partial t}. \tag{1.43}$$

For simplicity, we consider a situation where generic linear dielectrics are stacked periodically. Consequently, the displacement field $\boldsymbol{D}(\boldsymbol{r}, t)$ and the magnetic flux density $\boldsymbol{B}(\boldsymbol{r}, t)$ can be expressed as

$$\boldsymbol{D} = \epsilon_0 \underline{\epsilon}(\boldsymbol{r}) \boldsymbol{E}, \quad \boldsymbol{B} = \mu_0 \boldsymbol{H}. \tag{1.44}$$

Here, ϵ_0 and μ_0 are the vacuum permittivity and permeability, respectively, and we denote the relative permittivity as $\underline{\epsilon}(\boldsymbol{r})$. Thus, Maxwell's equations become

$$\nabla \cdot (\underline{\epsilon} \boldsymbol{E}) = 0, \quad \nabla \cdot \boldsymbol{H} = 0, \tag{1.45}$$

$$\underline{\epsilon}^{-1} \nabla \times (\nabla \times \boldsymbol{E}) = -\frac{1}{c^2} \frac{\partial^2 \boldsymbol{E}}{\partial t^2}, \quad \nabla \times \left(\underline{\epsilon}^{-1} \nabla \times \boldsymbol{H}\right) = -\frac{1}{c^2} \frac{\partial^2 \boldsymbol{H}}{\partial t^2}. \tag{1.46}$$

Here $c := 1/\sqrt{\epsilon_0 \mu_0}$ is the vacuum speed of light. For mathematical convenience, we use complex-valued fields. The physical fields are obtained by taking the real part of these complex-valued fields. Then, we can write electromagnetic fields using harmonic modes as a spatial part times a complex exponential representing temporal variation:

$$\begin{aligned} \boldsymbol{H}(\boldsymbol{r}, t) &= \boldsymbol{H}(\boldsymbol{r}) e^{-i\omega t}, \\ \boldsymbol{E}(\boldsymbol{r}, t) &= \boldsymbol{E}(\boldsymbol{r}) e^{-i\omega t}. \end{aligned}$$

This leads to eigenvalue equations for the electromagnetic field:

$$\Theta_E(\boldsymbol{r}) \boldsymbol{E}(\boldsymbol{r}) = \frac{\omega^2}{c^2} \boldsymbol{E}(\boldsymbol{r}), \quad \Theta_E(\boldsymbol{r}) \boldsymbol{E}(\boldsymbol{r}) := \underline{\epsilon}^{-1}(\boldsymbol{r}) \nabla \times (\nabla \times \boldsymbol{E}(\boldsymbol{r})) \tag{1.47}$$

or

$$\Theta_H(\boldsymbol{r}) \boldsymbol{H}(\boldsymbol{r}) = \frac{\omega^2}{c^2} \boldsymbol{H}(\boldsymbol{r}), \quad \Theta_H(\boldsymbol{r}) \boldsymbol{H}(\boldsymbol{r}) := \nabla \times \left(\underline{\epsilon}^{-1}(\boldsymbol{r}) \nabla \times \boldsymbol{H}(\boldsymbol{r})\right). \tag{1.48}$$

By incorporating the periodicity of the dielectric constant $\underline{\epsilon}(\boldsymbol{r}) = \underline{\epsilon}(\boldsymbol{r} + \boldsymbol{R})$ with a translation vector $\boldsymbol{R}$, it follows that the operators Θ_E and Θ_H inherit this periodicity. Consequently, the solutions to the eigenvalue problem, representing the frequencies and modes of the electromagnetic field, can be classified based on the wavevector $\boldsymbol{k}$ within the first Brillouin zone and band index n:

$$\Theta_E(\boldsymbol{r}) \boldsymbol{E}_{n\boldsymbol{k}}(\boldsymbol{r}) = \left(\frac{\omega_{n\boldsymbol{k}}}{c}\right)^2 \boldsymbol{E}_{n\boldsymbol{k}}(\boldsymbol{r}), \tag{1.49}$$

or

$$\Theta_H(\boldsymbol{r}) \boldsymbol{H}_{n\boldsymbol{k}}(\boldsymbol{r}) = \left(\frac{\omega_{n\boldsymbol{k}}}{c}\right)^2 \boldsymbol{H}_{n\boldsymbol{k}}(\boldsymbol{r}). \tag{1.50}$$

Here we denote the frequencies as $\omega_{n\boldsymbol{k}}$.

As shown above, photonic crystals exhibit photonic band structures. This structural characteristic opens the door to investigating the topological properties of these bands. The first theoretical proposal on the band topology of photonic crystals was presented by Raghu and Haldane [86, 87]. They studied a two-dimensional gyroelectric photonic crystal composed of dielectric rods arranged in a triangular lattice. By applying a static magnetic field to break time-reversal symmetry, they proposed a mechanism to open a gap in the Dirac cones present in the band structure (see FIG. 1.18 (a)). In fact, this approach revealed that the Chern number, defined as

$$\mathrm{ch_n} := \frac{1}{2\pi}\int d^2\boldsymbol{k}\left(\frac{\partial A_n^y(\boldsymbol{k})}{\partial k_x} - \frac{\partial A_n^x(\boldsymbol{k})}{\partial k_y}\right), \tag{1.51}$$

$$A_n^i(\boldsymbol{k}) := -i\left\langle \boldsymbol{E}_{n\boldsymbol{k}}\right| \partial_{k_i}\left|\boldsymbol{E}_{n\boldsymbol{k}}\right\rangle := -i\int d^2\boldsymbol{r}\,\boldsymbol{E}^*_{n\boldsymbol{k}}(\boldsymbol{r})\cdot\left(\underline{\epsilon}(\boldsymbol{r})\partial_{k_i}\boldsymbol{E}_{n\boldsymbol{k}}(\boldsymbol{r})\right), \tag{1.52}$$

takes non-zero values in such systems. Although the model proposed by Raghu and Haldane was challenging to realize experimentally, subsequent studies [88, 89] introduced practical designs using gyromagnetic photonic crystals (see FIG. 1.18(b, c)). These designs paved the way for experimental verification [89], significantly advancing the understanding of photonic band topology.

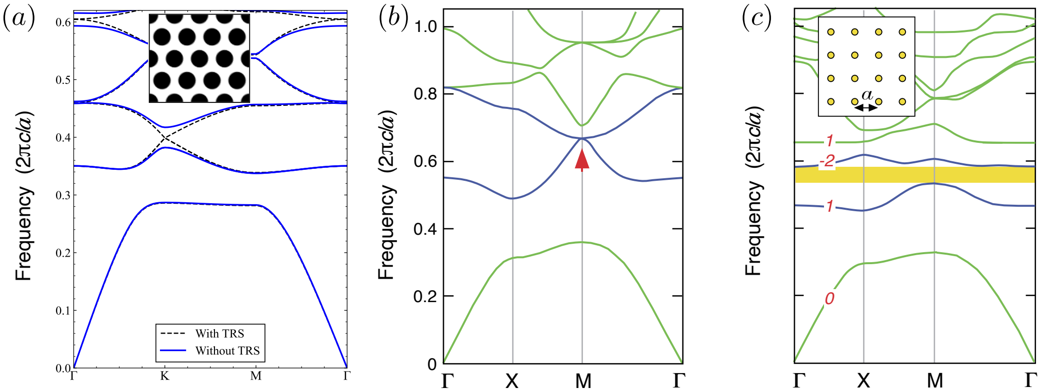

Figure 1.18: (a) Photonic band structure of the Raghu-Haldane model. When time-reversal symmetry is preserved, a Dirac cone appears (black dashed line). However, breaking time-reversal symmetry via the Faraday effect opens a gap (blue solid line). (b, c) The photonic analog of the quantum Hall effect proposed by Wang et al. The system corresponds to a photonic crystal realization of the Harper-Hofstadter model. Similar to the Raghu-Haldane model, a Dirac cone emerges when time-reversal symmetry is present (Figure (b)), while breaking time-reversal symmetry via the magneto-optical effect opens a gap (Figure (c)). These figure are cited from [88].

Topological photonic crystals can also be realized through methods beyond the quantum Hall insulator-like approach. A notable study in this context is the work of

Wu and Hu [28], who proposed a quantum pseudo-spin Hall insulator-like topological photonic crystal. The basic idea of this model can be understood in analogy with a tight-binding model discussed in Sec. 1.1.4: The proposed design begins with a two-dimensional photonic crystal consisting of dielectric rods arranged in a honeycomb lattice (see FIG. 1.19 (a)). This arrangement, due to its symmetry, results in the emergence of photonic Dirac cones at the K and K' points in the Brillouin zone. When adopting a hexagonal cluster of rods as the unit cell, the Dirac cones at K and K' fold back to the Γ point (see FIG. 1.19 (c)), similar to the behavior observed in tight-binding model. The next step involves modulating the positions of the dielectric rods. When the rods are shifted inward, closer to the center of the hexagonal cluster, this system corresponds to $t_0 > t_1$ case in the tight-binding model, which opens a trivial band gap at the Dirac point (see FIG. 1.19 (b, d)). Conversely, if the rods are shifted outward, away from the cluster center, this system corresponds to $t_0 < t_1$ case in the tight-binding model, leading to a band inversion and the opening of a nontrivial gap at the Dirac point. In this manner, quantum pseudo-spin states can also be generated in photonic crystals.

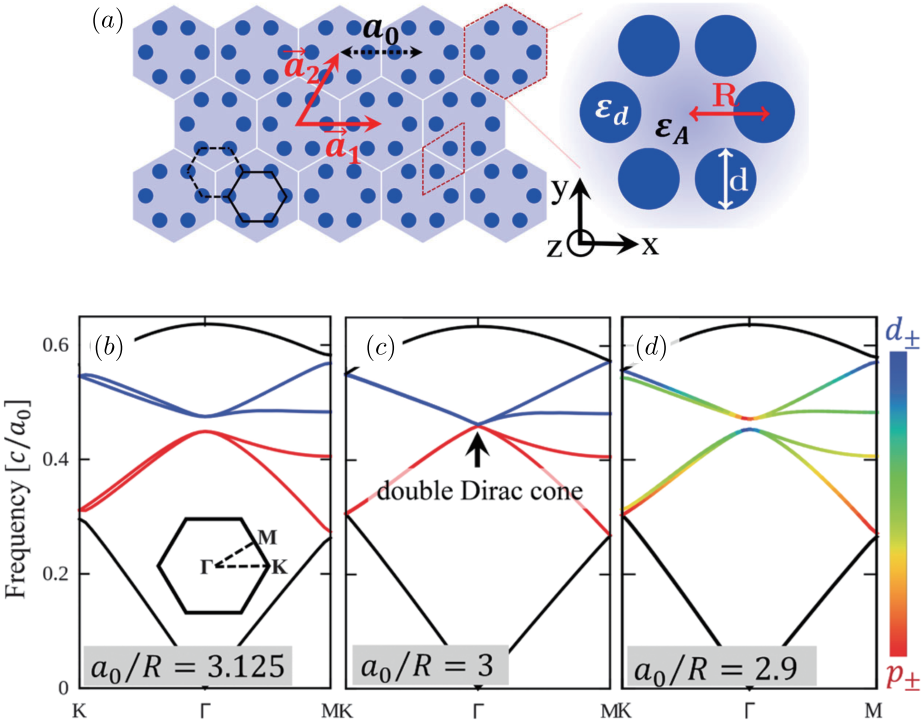

Figure 1.19: (a) Schematic illustration of the Wu-Hu model. Dielectric rods with $\epsilon_d = 11.7\epsilon_0$ are arranged in a honeycomb lattice. Here $\epsilon_A = \epsilon_0$. (b, c, d) Photonic band structures of the Wu-Hu model. A band inversion, similar to that in the tight-binding model, occurs. These figures are cited from [28].

The eigenmodes at the Γ point must form a basis for the irreducible representation of the point group $\mathrm{C}_{6\mathrm{v}}$. Indeed, the spatial distributions of these eigenmodes possess odd or even spatial parity, as shown in FIG. 1.20. Thus, similar to the tight-binding model, these modes can be used to construct pseudo-spin modes $p_\pm$ and $d_\pm$. In the tight-binding system, pseudo-spin-up (down) modes correspond to counterclockwise (clockwise) current flow, as discussed in Sec. 1.1.4. In the case of photonic crystals, the pseudo-spin-up (dowm) modes exhibit right-handed (left-handed) circular polarization, with the time average of the Poynting vector indicating counterclockwise (clockwise) flow (see FIG. 1.21).

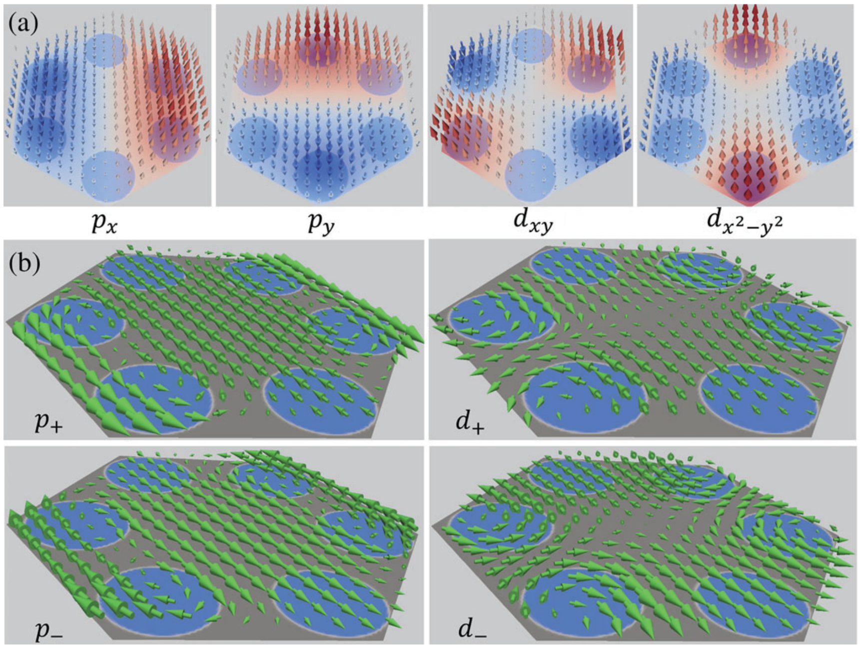

Figure 1.20: (a) Electric fields E_z of $p_x(p_y)$ and $d_{x^2-y^2}(d_{xy})$ photonic orbitals at the Γ point. (b) the corresponding magnetic fields associated with the pseudo spin modes $p_\pm$ and $d_\pm$. These figures are cited from [28].

The characteristics of these eigenmodes have a direct impact on transport at the interface. In other words, this enables selective excitation of pseudo-spin modes by injecting circularly polarized light at the edge of the system. Let us consider a system composed of two topologically distinct regions, with an external source placed at their interface to inject electromagnetic waves. When we place a harmonic source to inject linearly polarized light, both counterclockwise and clockwise modes are excited simultaneously, resulting in a symmetric distribution of electromagnetic energy along the interface (see FIG. 1.22). On the other hand, when we use circularly polarized light, either the counterclockwise or clockwise mode is selectively excited, leading to a

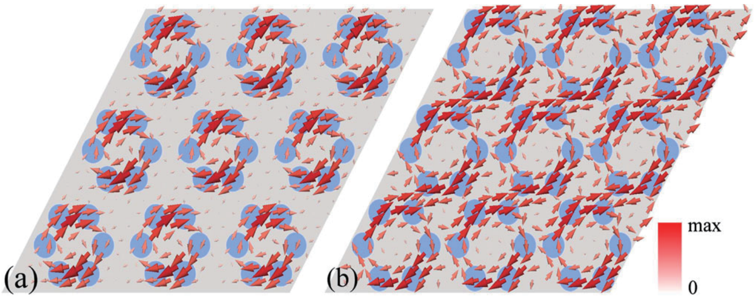

Figure 1.21: Real-space distributions of the time- averaged Poynting vector associated with the pseudospin-down state at the Γ point below the photonic gap: (a) $a_0/R = 3.125$ in the trivial regime and $a_0/R = 2.9$ in the topological regime. These figures are cited from [28].

unidirectional propagation of the excited electromagnetic wave along the interface (see FIG 1.22).

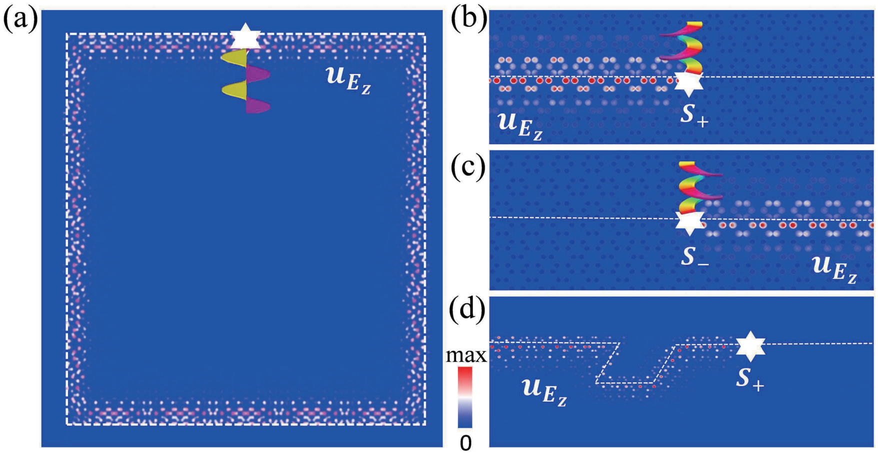

Figure 1.22: (a) Topological edge states excited by a harmonic source with linear polarization. (b) and (c) Unidirectional energy propagations excited by sources generating electromagnetic waves characterized by circular polarization. (d) Propagations of excited helical edge state along interfaces with sharp turning angles. These figures are cited from [28].

The Wu-Hu model offers several advantages for studying topological phases in photonic crystals, notably its theoretical versatility and experimental feasibility. The quantum Hall insulator-like approach requires breaking time-reversal symmetry, which often involves using gyromagnetic photonic crystals and specialized materials. In contrast, the Wu-Hu model only involves simple arrangements of dielectric rods, eliminating the need for exotic materials. This simplicity has enabled its implementation in various experimental platforms, including acoustic systems [90, 91], photonic systems [92, 93, 94], and microwave setups [95].

1.3 Motivation for the research in this thesis

We have reviewed topological phases in solid-state electronic systems and unconventional solids. Based on this foundation, the motivation behind the research presented in this dissertation can be summarized as follows:

- A key objective is to develop theoretical frameworks that are applicable to classical systems like photonic crystals. To this end, interactions unique to solid-state electronic systems, such as spin-orbit coupling, are deliberately excluded.
- Our research aims to propose models that are versatile and experimentally practical. Taking inspiration from the tight-binding model introduced by Wu and Hu, the focus is on systems incorporating only real-valued hopping terms. The ultimate goal is to design models that can be realized using simple experimental setups, such as arrays of dielectric rods.

1.4 Organization of this thesis

The rest of this thesis is organized as follows. In Chapter 2, we start with the theory of Wilson loops and topological invariants. We provide a review of how topological invariants have been formulated and utilized in previous research. In Chapter 3, as an extension of Wu-Hu model, we delve into our study on a chiral honeycomb lattice model. The proposed model is specifically designed with applications to soft matter systems in mind, and has features of sublattice and mirror symmetry breaking. Consequently, the resulting band topology exhibits notable differences from those presented in earlier works. In Chapter 4, we present the study on a classical system. By mapping the model introduced in Chapter 3 onto a classical system, one can analyze its classical dynamics. In this system, an asymmetric edge current can be excited. In Chapter 5, we focus on our study of HOTIs. By using an extra-site model, the topological quadrupole-like phase can be implimented. In Chapter 6, we summarize this thesis.

Chapter 2

Wilson loops and topological invariants

The Wilson loop is a powerful concept in solid-state physics, particularly in the study of topological properties of electronic bands. It originates from gauge theories in high-energy physics, but has found profound applications in the theory of Berry phases and topology in condensed matter systems. In this chapter, we shortly summarize the concept of Wilson loops and the related topological invariants. Throughout this chapter, we refer to and follow the discussions in [96, 97, 98].

2.1 Wilson loops

2.1.1 Definitions

In the context of solid-state physics, the Wilson loop refers to a path-ordered exponential of the Berry connection over a closed loop in momentum space. In general, to accommodate degenerate band structures, we define the Berry connection matrix $\boldsymbol{A}(\boldsymbol{k})$, which extends the concept of the Berry connection to multiple bands (see also Sec. 1.1.1). The elements of $\boldsymbol{A}(\boldsymbol{k})$ are given by

$$\boldsymbol{A}_{mn}(\boldsymbol{k}) := -i \langle u_m(\boldsymbol{k}) | \nabla_{\boldsymbol{k}} | u_n(\boldsymbol{k}) \rangle . \tag{2.1}$$

where $|u_m(\boldsymbol{k})\rangle$ and $|u_n(\boldsymbol{k})\rangle$ are the periodic part of the Bloch function. Using this Berry connection matrix, the Wilson loop is mathematically expressed as

$$W_C = \mathcal{P} \exp \left(i \oint_C \boldsymbol{A}(\boldsymbol{k}) \cdot d\boldsymbol{k} \right), \tag{2.2}$$

where $\mathcal{P}$ denotes path ordering, and C is a closed loop in momentum space.

In practice, the Wilson loop is computed by discretizing momentum space into a grid. Let us descretize the loop C into N small segments with $\boldsymbol{k}_i$ representing the discrete momentum points along the path, such that $i = 1, 2, \cdots, N$ and $\boldsymbol{k}_{N+1} = \boldsymbol{k}_1$.

We approximate the momentum difference $\Delta\boldsymbol{k}_i := \boldsymbol{k}_{i+1} - \boldsymbol{k}_i$ between adjacent points be small. For each small segment of the path from $\boldsymbol{k}_i$ to $\boldsymbol{k}_{i+1}$, the contribution to the Wilson loop reads

$$\exp\left(i\int_{\boldsymbol{k}_i\to\boldsymbol{k}_{i+1}} \boldsymbol{A}(\boldsymbol{k})\cdot d\boldsymbol{k}\right) \simeq \exp\left(i\boldsymbol{A}(\boldsymbol{k}_i)\cdot\Delta\boldsymbol{k}_i\right) \simeq I + i\boldsymbol{A}(\boldsymbol{k}_i)\cdot\Delta\boldsymbol{k}_i. \tag{2.3}$$

Here I is the identity matrix, and we neglect higher-order terms of $\Delta\boldsymbol{k}_i$. Furthermore, these contribution are calculated from the overlap between Bloch wavefunctions at neighboring points:

$$\begin{aligned}\left[\exp\left(i\boldsymbol{A}(\boldsymbol{k}_i)\cdot\Delta\boldsymbol{k}_i\right)\right]_{mn} &\simeq \delta_{mn} + i\boldsymbol{A}_{mn}(\boldsymbol{k}_i)\cdot\Delta\boldsymbol{k}_i \\ &= \langle u_m(\boldsymbol{k}_i)|u_n(\boldsymbol{k}_i)\rangle + \langle u_m(\boldsymbol{k}_i)|\,\nabla_{\boldsymbol{k}_i}\,|u_n(\boldsymbol{k}_i)\rangle\cdot\Delta\boldsymbol{k}_i \\ &\simeq \langle u_m(\boldsymbol{k}_i)|u_n(\boldsymbol{k}_{i+1})\rangle =: \left[M_{\boldsymbol{k}_i\to\boldsymbol{k}_{i+1}}\right]_{mn},\end{aligned} \tag{2.4}$$

where we have defined the overlap matrices $M_{\boldsymbol{k}_i\to\boldsymbol{k}_{i+1}}$. Therefore, over the entire path C, the path-ordered exponential becomes a product of these small contributions, i.e.

$$W_C \simeq \prod_{i=1}^{N} \exp\left(i\boldsymbol{A}(\boldsymbol{k}_i)\cdot\Delta\boldsymbol{k}_i\right) \simeq \prod_{i=1}^{N} M_{\boldsymbol{k}_i\to\boldsymbol{k}_{i+1}}. \tag{2.5}$$

2.1.2 Hybrid Wannier centers

The Wilson loop is a quantity related to the expectation value of the electron position. Let us briefly confirm this relationship. For simplicity, we take the path C to be a line along the k_x axis. Since we are working within the Brillouin zone, this path is periodic, forming a closed loop as required by the definition of the Wilson loop. In this case, the Wilson loop is computed as

$$W_{x,\vec{k}} := \prod_{i=1}^{N_x} M_{(k_x^0+(i-1)\Delta k_x,\vec{k})\to(k_x^0+i\Delta k_x,\vec{k})}, \tag{2.6}$$

where we define $\boldsymbol{k} = (k_x, \vec{k})$ and $\Delta k_x = 2\pi/N_x$, with N_x $(= N)$ being the number of unit cells along the x-axis, determining the discretization of k_x. Moreover, we assume that there are N_{occ} occupied bands, and thus the Wilson line elements are defined as

$$\left[M_{(k_x^0+(i-1)\Delta k_x,\vec{k})\to(k_x^0+i\Delta k_x,\vec{k})}\right]_{mn} = \langle u_m(k_x,\vec{k})|u_n(k_x+\Delta k_x,\vec{k})\rangle \;\; (m,n = 1,\cdots,N_{\text{occ}}), \tag{2.7}$$

considering only the occupied bands. We then diagonalize the Wilson loop as follows:

$$W_{x,\vec{k}}\left|\nu^j_{x,\vec{k}}\right\rangle = \exp\left(2\pi i\nu^j_x(\vec{k})\right)\left|\nu^j_{x,\vec{k}}\right\rangle. \tag{2.8}$$

Here the index j $(= 1, \cdots, N_{\text{occ}})$ labels the eigenstates of the Wilson loop, indicating the corresponding eigenvalues $\nu_x^j(\vec{k})$ and their associated states $\left|\nu_{x,\vec{k}}^j\right\rangle$. The eigenvalues of this Wilson loop correspond to the hybrid Wannier centers (the expectation values of the position operator for hybrid Wannier functions), as we shall see below. Using the eigenvectors of the Wilson loop, the hybrid Wannier function is defined as

$$\left|\Psi_{R_x,\vec{k}}^j\right\rangle = \frac{1}{\sqrt{N_x}} \sum_{n=1}^{N_{\text{occ}}} \sum_{k_x} \left|\psi_n(k_x, \vec{k})\right\rangle \left[\left|\nu_{x,\vec{k}}^j\right\rangle\right]^n e^{-ik_x R_x}, \tag{2.9}$$

where $\left|\psi_n(k_x, \vec{k})\right\rangle$ is the Bloch wave function. Here we denote the n-th element of vector $\left|\nu_{x,\vec{k}}^j\right\rangle$ as $\left[\left|\nu_{x,\vec{k}}^j\right\rangle\right]^n (n = 1, \cdots, N_{\text{occ}})$. In general, the hybrid Wannier function is localized around R_x in the x-direction but not localized in other directions[1][97, 98]. Furthermore, it is known that the hybrid Wannier centers are nothing but $\nu_x^j(\vec{k})$ [98]:

$$(\text{hybrid Wannier center}) := \left\langle \Psi_{R_x=0,\vec{k}}^j \middle| x \middle| \Psi_{R_x=0,\vec{k}}^j \right\rangle = \nu_x^j(\vec{k}). \tag{2.10}$$

By plotting $\nu_x^j(\vec{k})$ as a function of $\vec{k}$, we obtain the Wannier bands, which provide crucial insight into the topology of the system, as we will see in this chapter.

In particular, for a one-dimensional $\boldsymbol{k}$-space, one can construct the Wannier center and Wannier functions from the Wilson loop, which allows the calculation of physical quantities such as electric polarization. Indeed, according to the modern theory of electric polarization, in a one-dimensional system with a single occupied band ($j = 1$), the electric polarization p_x is given by

$$p_x = e\nu_x. \tag{2.11}$$

Here, since we are considering a one-dimensional system, the dependence on $\vec{k}$ disappears.

2.2 Sublattice symmetry and winding number

To make the above discussion concrete, let us consider the SSH model. As we will discuss in this section, SSH model exhibits sublattice symmetry, which plays a crucial role in the emergence of its topological phase, making it one of the simplest examples of such a system. In this section, the lattice constant is set to $a_0 = 1$.

2.2.1 Basics

To begin, we first examine the topology of general one-dimensional 2×2 Hermitian matrices as a preliminary discussion. Such matrices can be expressed using the Pauli

---

[1] In contrast, conventional Wannier functions are localized in all spatial directions.

matrices as follows:

$$H_{2\times 2}(k_x) = \boldsymbol{R}(k_x)\cdot\boldsymbol{\sigma} = R_x(k_x)\sigma_x + R_y(k_x)\sigma_y + R_z(k_x)\sigma_z, \tag{2.12}$$

where $\boldsymbol{R}(k_x) = (R_x(k_x), R_y(k_x), R_z(k_x))$ represents the coefficients of expansion. Since the term proportional to σ_0 does not affect the topology, it is neglected for simplicity. To study the topology of this system, we consider the trajectory of the normalized expansion coefficient $\hat{\boldsymbol{R}}(k_x) := \boldsymbol{R}(k_x)/|\boldsymbol{R}(k_x)|$ as k_x varies from $-\pi$ to π. This corresponds to considering continuous mappings from $k_x \in S^1 = [0, 2\pi)$ (Brillouin zone) to $\hat{\boldsymbol{R}}(k_x) \in S^2$ (the target space) and classifying them topologically.

Continuous mappings from S^1 to a target space are classified by the first homotopy group [99]. For the target space S^2, however, such mappings can always be continuously deformed to a single point, meaning only a trivial topological sector exists:

$$\pi_1(S^2) = 0. \tag{2.13}$$

As a result, one-dimensional lattice models without any symmetry are topologically equivalent, and there are no distinct topological phases.

When symmetries are imposed, however, they restrict the possible deformations of mappings, potentially leading to nontrivial topological sectors that cannot be connected as long as the symmetry is preserved. A notable example is the imposition of sublattice symmetry[2]. For 2 × 2 Hermitian matrices, the sublattice symmetry requires the anticommutation relation

$$\{H_{2\times 2}(k_x), \sigma_z\} = 0, \tag{2.14}$$

which eliminates the σ_z term from $H_{2\times 2}(k_x)$, i.e.,

$$H_{2\times 2}(k_x) = \begin{pmatrix} 0 & R_x(k_x) - iR_y(k_x) \\ R_x(k_x) + iR_y(k_x) & 0 \end{pmatrix} \tag{2.15}$$

and reduce the degrees of freedom of $\boldsymbol{R}(k_x)$. The resulting mapping now involves $k_x \in S^1$ to $\hat{\boldsymbol{R}}(k_x) = (R_x, R_y)/\sqrt{R_x^2 + R_y^2} \in S^1$, and thus its topological classification under sublattice symmetry is given by

$$\pi_1(S^1) = \mathbb{Z}. \tag{2.16}$$

This implies the existence of nontrivial topological sectors. In fact, these mappings are classified by the winding number, which represents the number of times $\hat{\boldsymbol{R}}(k_x)$ wraps around the origin. This winding number is expressed as

$$w = -\frac{1}{2\pi}\int_0^{2\pi} dk_x \left(\frac{d}{dk_x}\arg\left(q(k_x)\right)\right), \tag{2.17}$$

---

[2] In general, it is often referred to as chiral symmetry, which is a combination of time-reversal symmetry and particle-hole symmetry; however, in this thesis, we use "chiral" to describe mirror symmetry breaking, and the combination of time-reversal symmetry and particle-hole symmetry will not be discussed. Thus, we exclude its usage for the combination of time-reversal and particle-hole symmetries, and only discuss the sublattice symmetry.

where $q(k_x) := R_x(k_x) - iR_y(k_x)$.

This framework extends naturally to general one-dimensional $N \times N$ Hermitian matrices (where the N is even). In such cases, the Hamiltonian with sublattice symmetry can be written as

$$H_{N\times N}(k_x) = \begin{pmatrix} 0_{N/2\times N/2} & Q(k_x) \\ Q(k_x)^\dagger & 0_{N/2\times N/2} \end{pmatrix}, \tag{2.18}$$

with a suitable choice of basis. Here, $Q(k_x)$ is an $N/2 \times N/2$ complex matrix with a nonzero determinant. Then, the winding number is defined as

$$w = -\frac{1}{2\pi}\int_0^{2\pi} dk_x \left(\frac{d}{dk_x}\arg\left(\det Q(k_x)\right)\right). \tag{2.19}$$

2.2.2 Su-Schrieffer-Heeger model

As stated in Eq. (1.18), the Bloch Hamiltonian of SSH model is

$$H_{\mathrm{SSH}}(k_x) = \begin{pmatrix} 0 & t_1 + t_2 e^{-ik_x} \\ t_1 + t_2 e^{ik_x} & 0 \end{pmatrix} =: \begin{pmatrix} 0 & q(k_x) \\ q(k_x)^* & 0 \end{pmatrix}, \tag{2.20}$$

with eigenvalues and eigenstates given by

$$E_\pm(k_x) = \pm|q(k_x)|, \quad |u_\pm(k_x)\rangle = \frac{1}{\sqrt{2}}\begin{pmatrix} e^{i\arg(q(k_x))} \\ \pm 1 \end{pmatrix}. \tag{2.21}$$

The winding number can be calculated as

$$w = -\frac{1}{2\pi}\int_0^{2\pi} dk_x \left(\frac{d}{dk_x}\arg\left(q(k_x)\right)\right) = \begin{cases} 1 & \text{if } |t_1| < |t_2| \\ 0 & \text{if } |t_1| > |t_2| \end{cases}. \tag{2.22}$$

This can be intuitively understood by considering the case of $(t_1, t_2) = (0, 1)$, where the unsplit zero-energy edge modes emerge. In this case, $\arg(q(k_x)) = -k_x$, and thus $w = 1$.

The winding number can also be derived through the Wilson loop. For the half-filling case, the Wilson loop is expressed as

$$W_x = \prod_{i=1}^{N_x} M_{k_x+(i-1)\Delta k_x \to k_x + i\Delta k_x} \overset{\text{continuum limit}}{\rightarrow} \exp\left(i\int_0^{2\pi} A^x_{--}(k_x)dk_x\right). \tag{2.23}$$

where N_x represents the number of subdivisions of the Brillouin zone, with $\Delta k_x = 2\pi/N_x$, and the Berry connection reads

$$A^x_{--}(k_x) := -i\left\langle u_-(k_x)\right| \partial_{k_x}\left|u_-(k_x)\right\rangle. \tag{2.24}$$

By using Eq. (2.21), the Berry connection is readly derived as

$$A^x_{--}(k_x) = -\frac{1}{2}\frac{d}{dk_x}\arg(q(k_x)) \tag{2.25}$$

Therefore, the Wilson loop becomes

$$W_x = \exp\left(i\int_0^{2\pi} A^x_{--}(k_x)dk_x\right) = \exp\left(i2\pi\frac{w}{2}\right), \tag{2.26}$$

and the Wannier center is retrieved as $\nu_x = w/2$. Therefore, the topological nontriviality can also be detected by computing the Wilson loop and the associated Wannier centers. The related polarization reads

$$p_x = e\nu_x = \begin{cases} e/2 & \text{if } |t_1| < |t_2| \\ 0 & \text{if } |t_1| > |t_2| \end{cases}. \tag{2.27}$$

We note that, in the continuum limit, the electric polarization can be expressed as a Berry phase:

$$p_x = \frac{e}{2\pi}\int_0^{2\pi} A^x_{--}(k_x)dk_x. \tag{2.28}$$

2.3 Mirror symmetry and quadrupole moment

2.3.1 π-flux and mirror symmetry

Before delving into the discussion of topological quadrupole phase, let us examine the symmetries of a system where a π-flux is introduced in the plaquettes. For simplicity, we analyze a simple four-site model arranged at the vertices of a square, as shown in Figure 2.1. The Hamiltonian of this system can be written as

$$H_0 = \gamma\begin{pmatrix} 0 & 1 & -1 & 0 \\ 1 & 0 & 0 & 1 \\ -1 & 0 & 0 & 1 \\ 0 & 1 & 1 & 0 \end{pmatrix}. \tag{2.29}$$

Here we use atomic orbitals $\{|\psi_i\rangle\}_{i=1,2,3,4}$, as shown in FIG. 2.1 In this configuration, the hopping term for the bond between sites 1 and 3 has its sign flipped, which introduces π-flux per plaquettes. The system exhibits mirror symmetry with respect to $M_y : y \to -y$, i.e.

$$M_y := \begin{pmatrix} 0 & 0 & 1 & 0 \\ 0 & 0 & 0 & 1 \\ 1 & 0 & 0 & 0 \\ 0 & 1 & 0 & 0 \end{pmatrix}, \tag{2.30}$$

and $[H_0, M_y] = 0$. However, it does not retain symmetry under the mirror operation $M_x : x \to -x$, i.e.

$$M_x := \begin{pmatrix} 0 & 1 & 0 & 0 \\ 1 & 0 & 0 & 0 \\ 0 & 0 & 0 & 1 \\ 0 & 0 & 1 & 0 \end{pmatrix}, \tag{2.31}$$

and $[H_0, M_x] \neq 0$. In this sense, the system lacks conventional mirror symmetry about the y-axis. Nevertheless, if we consider a generalized mirror operation that includes a gauge transformation of the atomic orbitals, the system retains mirror symmetry. Specifically, as shown in Figure 2.1, applying the mirror operation followed by a gauge transformation, where $|\psi_2\rangle \to -|\psi_2\rangle$ and $|\psi_4\rangle \to -|\psi_4\rangle$, restores the system to its original state. This process is described as

$$\tilde{M}_x := \begin{pmatrix} 1 & 0 & 0 & 0 \\ 0 & -1 & 0 & 0 \\ 0 & 0 & 1 & 0 \\ 0 & 0 & 0 & -1 \end{pmatrix} \begin{pmatrix} 0 & 1 & 0 & 0 \\ 1 & 0 & 0 & 0 \\ 0 & 0 & 0 & 1 \\ 0 & 0 & 1 & 0 \end{pmatrix}. \tag{2.32}$$

Thus, systems with a π-flux exhibit generalized mirror symmetry that incorporates the gauge transformation.

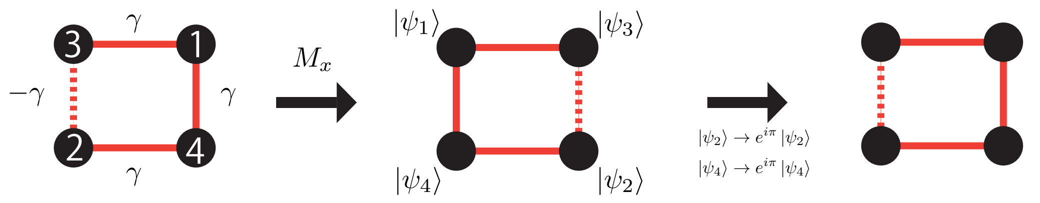

Figure 2.1: A four-site toy model. Under the mirror operation M_x, the locations where the sign flips occur are altered. However, by performing a gauge transformation on the atomic orbitals, the sign-flipped regions can be restored to their original positions. In this sense, when including gauge transformations of the atomic orbitals, the system retains mirror symmetry.

For these generalized mirror operations, it can be seen that they do not commute but instead anticommute, such that

$$\{\tilde{M}_x, M_y\} = 0. \tag{2.33}$$

The presence of such anticommuting mirror operations is a crucial feature for discussing the topological quadrupole phase in the BBH model [29]. In fact, it is known that a topological quadrupole moment cannot be realized if the mirror operations commute [29]. Moreover, the gap in the Wannier bands only opens when the mirror operations anticommute [29].

2.3.2 Benalcazar-Bernevig-Hughes model

Let us now characterize the topological quadrupole phase in the BBH model using the Wilson loop. The discussion in this subsection is based on the proposal by Benalcazar et al. [29]. In this section, the lattice constant is set to $a_0 = 1$.

For the bulk Bloch Hamiltonian, assuming the band gap is open and the system is at half-filling, the occupied bands correspond to the two bands below the band gap, denoted as $|u_m(\boldsymbol{k})\rangle \quad (m = 1, 2)$ (see Sec. 1.1.5). The Wilson loop can be constructed in the same manner of Eq. (2.6) and (2.7) (see FIG. 2.2 (a)), and diagonalized as

$$W_{x,k_y} = \sum_{j=\pm} \exp\left(2\pi i \nu_x^j(k_y)\right) \left|\nu_{x,k_y}^j\right\rangle \left\langle \nu_{x,k_y}^j\right| \tag{2.34}$$

with eigenvalues $\exp\left(2\pi i \nu_x^j(k_y)\right)$ and the corresponding eigenvectors $\left|\nu_{x,k_y}^j\right\rangle$ (Here we choose the labeling of j such that $\nu_x^-(k_y) \leq \nu_x^+(k_y)$). If the system is invariant under the mirror operation M_y, the eigenvalues satisfy the constraint $\nu_x^-(k_y) = -\nu_x^+(k_y)$, as shown in FIG. 2.2 (b).

When the Wannier bands are gapped, it becomes possible to decompose the Bloch wavefunctions into separate Wannier band sectors. The revised wavefunctions $\left|w_{x,k_y}^\pm(k_x, k_y)\right\rangle$ is then defined as

$$\left|w_{x,k_y}^\pm(k_x, k_y)\right\rangle := \sum_{n=1,2} |u_n(k_x, k_y)\rangle \left[|\nu_{x,k_y}^\pm\rangle\right]^n. \tag{2.35}$$

Here we denote the n-th element of vector $|\nu_{x,k_y}^\pm\rangle$ as $\left[|\nu_{x,k_y}^\pm\rangle\right]^n$ $(n = 1, 2)$. The Wilson loop can be recalculated for each Wannier sector as

$$\tilde{W}_{y,k_x}^\pm := \prod_{i=1}^{N_y} \tilde{M}_{(k_x,k_y+(i-1)\Delta k_y)\to(k_x,k_y+i\Delta k_y)}^\pm. \tag{2.36}$$

Here, the matrix $\tilde{M}_{(k_x,k_y)\to(k_x,k_y+\Delta k_y)}^\pm$ is defined as

$$\tilde{M}_{(k_x,k_y)\to(k_x,k_y+\Delta k_y)}^\pm := \langle w_{x,k_y}^\pm(k_x, k_y)|w_{x,k_y+\Delta k_y}^\pm(k_x, k_y + \Delta k_y)\rangle. \tag{2.37}$$

From this, the "polarization" for each Wannier sector, which is an analogy to polarization Eq. (2.28) in SSH model, can be determined as

$$p_y^{\nu_x^\pm} = -\frac{i}{2\pi}\frac{1}{N_x}\sum_{k_x} \mathrm{Log}\left[\tilde{W}_{y,k_x}^\pm\right] \xrightarrow{\text{continuum limit}} \frac{1}{(2\pi)^2}\int_{\mathrm{BZ}} \tilde{A}_{y,k_x}^\pm(k_x, k_y) d^2k. \tag{2.38}$$

Here we define the Berry connection $\tilde{A}_{y,k_x}^\pm(k_x, k_y) := -i \langle w_{x,k_y}^\pm(k_x, k_y)| \partial_{k_y} |w_{x,k_y}^\pm(k_x, k_y)\rangle$. The same procedure can also be applied to the y-direction. Furthermore, the BBH model possesses generalized mirror symmetries $\tilde{M}_x$, M_y, as well as inversion symmetry

$I = \tilde{M}_x M_y$, and thus these symmetries impose the constraints on the polarizations of the Wannier band subspace, i.e.,

$$p_y^{\nu_x^+} \overset{\tilde{M}_x}{=} p_y^{\nu_x^-}, \quad p_y^{\nu_x^\pm} \overset{M_y}{=} -p_y^{\nu_x^\pm}, \quad p_y^{\nu_x^+} \overset{I}{=} -p_y^{\nu_x^-} \quad \text{mod } 1, \tag{2.39}$$

which ensures that the polarization is quantized as

$$p_y^{\nu_x^\pm}, p_x^{\nu_y^\pm} \overset{I,\tilde{M}_x,M_y}{=} 0 \ \text{ or } \ 1/2. \tag{2.40}$$

This quantization enables a $\mathbb{Z}_2 \times \mathbb{Z}_2$ classification of the system using $(p_y^{\nu_x^\pm}, p_x^{\nu_y^\pm})$. In fact, in the nontrivial phase $|\gamma| < |\lambda|$, the polarization values are $(p_y^{\nu_x^\pm}, p_x^{\nu_y^\pm}) = (1/2, 1/2)$, while in the trivial phase, they are $(p_y^{\nu_x^\pm}, p_x^{\nu_y^\pm}) = (0, 0)$ (see FIG. 2.2 (c)). As a result, the topological quadrupole invariant reads

$$q_{x,y} = 2e p_x^{\nu_y^\pm} p_y^{\nu_x^\pm} = \begin{cases} e/2 & \text{if } |\gamma| < |\lambda| \\ 0 & \text{if } |\gamma| > |\lambda| \end{cases}. \tag{2.41}$$

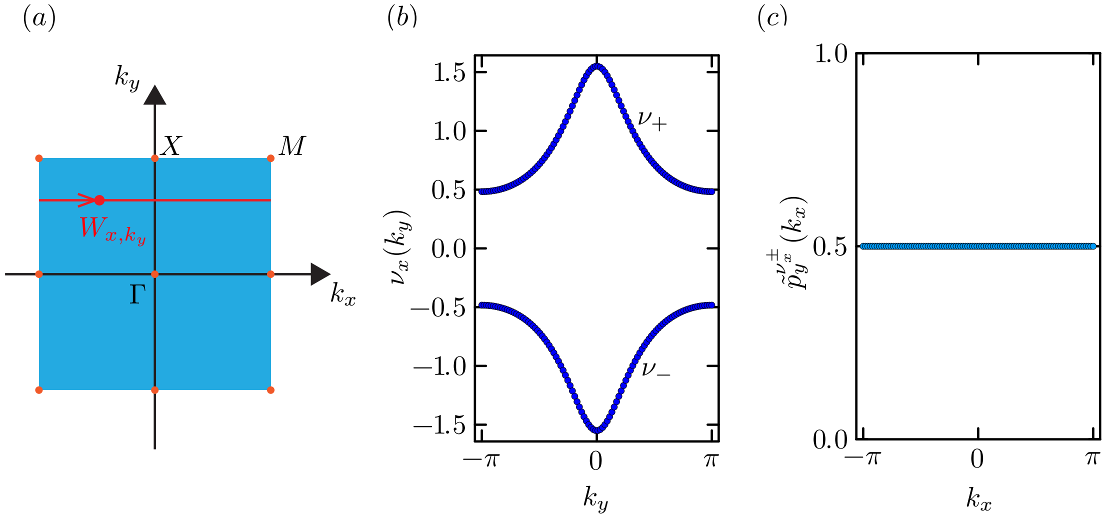

Figure 2.2: (a) The calculation of the Wilson loop W_{x,k_y}. We specify a path along k_x-axis in $2D$ Brillouin zone. (b) Wannier band structures. A Wannier band gap opens as a consequence of mirror symmetry. (c) Calculation of the $\mathbb{Z}_2$ invariant. The "polarization" is computed using Wannier functions and is quantized to 1/2 due to symmetry constraints.

2.4 Mirror winding number

The edge states of the Wu-Hu model discussed in Sec. 1.1.4 can also be analyzed by combining the winding number, as discussed in the context of the SSH model, and mirror symmetry. In this section, we interpret the Wu-Hu model as a honeycomb lattice model with bond modulation, based on a minimal graphene model, and review the work of Kariyado et al. [27], which characterizes the topological edge states using a mirror winding number.

2.4.1 Edge states in honeycomb lattice model

Let us first revisit the case without bond modulation, where $t_0 = t_1$ (see FIG. 2.3 (b)). This simple tight-binding model has been extensively studied in the context of graphene research, as it is the minimal model of graphene. When a zigzag edge is considered and open boundary conditions are imposed, flat bands appear as edge states in the band structure, plotted as a function of the wavevector $k_{||}$ along the edge (see FIG. 2.3 (b)). When bond modulation $t_0 \neq t_1$ is induced, the Dirac mass term arises, opening a bulk bandgap (see FIG. 2.3 (c)). However, the edge states persist due to the preservation of sublattice symmetry under the bond modulation. Furthermore, when systems with different signs of the mass term are joined together, edge states localized at the interface emerge, corresponding to quantum pseudo-spin states (see Sec. 1.1.4 and FIG. 2.3 (d, e)).

2.4.2 Topological characterization of Wu-Hu model

Let us now characterize these edge states using a topological index. In this section, we adopt the choice of unit cell as shown in FIG. 2.3(a, b), and define the unit vectors as $\boldsymbol{a}_1 = (3a_0, 0)$, $\boldsymbol{a}_2 = (3a_0/2, \sqrt{3}a_0/2)$. Then, the Hamiltonian can be written as

$$H_{\mathrm{Wu-Hu}}(\boldsymbol{k}) = \begin{pmatrix} 0 & D(\boldsymbol{k}) \\ D^{\dagger}(\boldsymbol{k}) & 0 \end{pmatrix}, \tag{2.42}$$

$$D(\boldsymbol{k}) = \begin{pmatrix} t_1 XY^* & t_0 & t_0 \\ t_0 & t_1 X^* & t_0 Y^* \\ t_0 & t_0 & t_1 \end{pmatrix}, \tag{2.43}$$

where $X := e^{i\boldsymbol{k}\cdot\boldsymbol{a}_1}$ and $Y := e^{i\boldsymbol{k}\cdot\boldsymbol{a}_2}$. This Hamiltonian still possesses the sublattice symmetry, i.e.,

$$\{H_{\mathrm{Wu-Hu}}(\boldsymbol{k}), \Gamma\} = 0, \quad \Gamma = \begin{pmatrix} 1_{3\times3} & 0 \\ 0 & -1_{3\times3} \end{pmatrix}, \tag{2.44}$$

which enables the introduction of a winding number as

$$w_{k_{||}} = -\frac{1}{2\pi}\int_0^{2\pi} dk_2 \left(\frac{d}{dk_2}\arg\left(\det(D(k_{||}, k_2))\right)\right). \tag{2.45}$$

Here we use the formula Eq. (2.19). We denote the momentum parallel to the edge as $k_{||}$, and treat it as a free parameter.

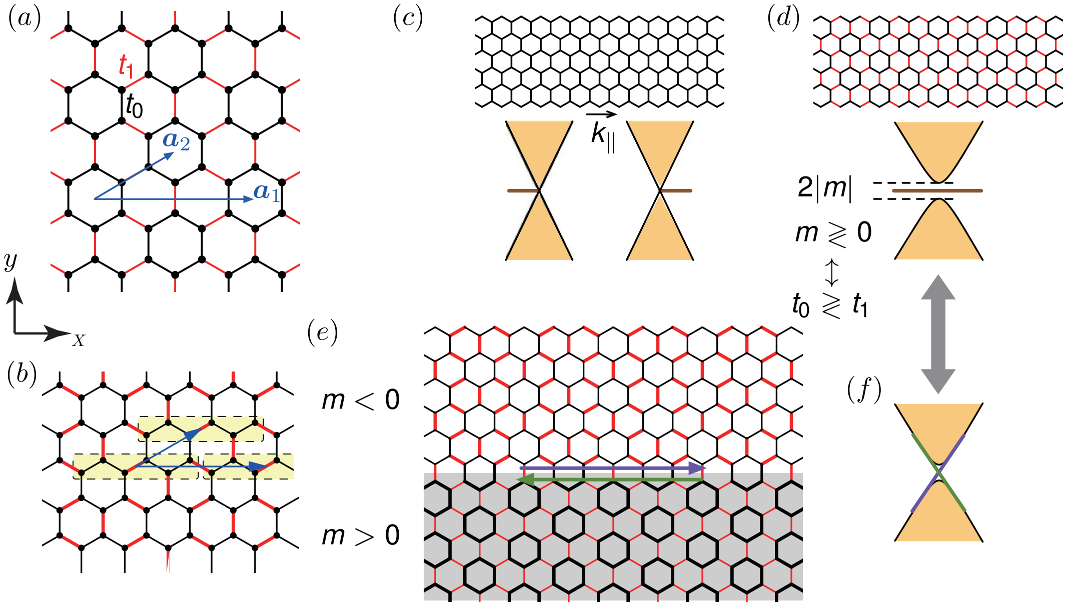

Figure 2.3: (a) The tight-binding model proposed by Wu and Hu [24] and the unit vectors in the present discussion. The choice of basis vectors is illustrated schematically. (b) The choice of unit cell (the region enclosed by the yellow square) adopted in the present discussion. (c) Schematic illustration of edge band structure with $t_0 = t_1$. (d) Schematic illustration of edge band structure with $t_0 \neq t_1$. (e) Schematic pictures for decorated edge and interface with different Dirac masses of opposite sign. (f) Schematic illustration of edge band structure with different Dirac masses. All figures are cited from [27].

At $k_{||} = 0$, in addition to the sublattice symmetry, the system also possesses mirror symmetry under the mirror operation $M_x : x \to -x$, satisfying

$$[\Gamma, M_x] = 0. \tag{2.46}$$

This is due to the fact that the mirror symmetry with respect to the plane perpendicular to the zigzag edge is preserved even in the bond modulation ($t_0 \neq t_1$) bond modulation. Furthermore, for $H_{\mathrm{Wu-Hu}}(k_{||}, k_2)$, it can be confirmed that

$$\left[H_{\mathrm{Wu-Hu}}(k_{||} = 0, k_2), M_x\right] = 0. \tag{2.47}$$

From these commutation relations, the Hamiltonian $H_{\mathrm{Wu-Hu}}(k_{||} = 0, k_2)$ can be decomposed into subspaces with even and odd parities under the mirror operation, while maintaining sublattice symmetry within each subspace. Consequently, winding numbers can be defined separately for these subspaces at $k_{||} = 0$, denoted as (w_+, w_-), which are referred to as mirror winding numbers. Specifically, in the case of graphene with zigzag edges, the matrix $D(\boldsymbol{k})$ in Eq. (2.43) an be decomposed into

$$D^+_{k_\perp} = \begin{pmatrix} t_1 Y^* & \sqrt{2}t_0 \\ \sqrt{2}t_0 & t_1 + t_0 Y^* \end{pmatrix}, D^-_{k_\perp} = t_1 - t_0 Y^*, \tag{2.48}$$

leading to the mirror winding numbers as

$$(w_+, w_-) = \begin{cases} (1,0) & \text{if} \quad |t_0| < |t_1| \\ (0,1) & \text{if} \quad |t_0| > |t_1| \end{cases}. \tag{2.49}$$

Here we define $Y := e^{i\boldsymbol{k}\cdot\boldsymbol{a}_2}$. This indicates that as the system transitions from $|t_0| < |t_1|$ to $|t_0| > |t_1|$, the mirror winding numbers change from $(1,0)$ to $(0,1)$, and these two phases are topologically distinct, which is consistent with the analysis based on the Dirac equation (see FIG. 2.4).

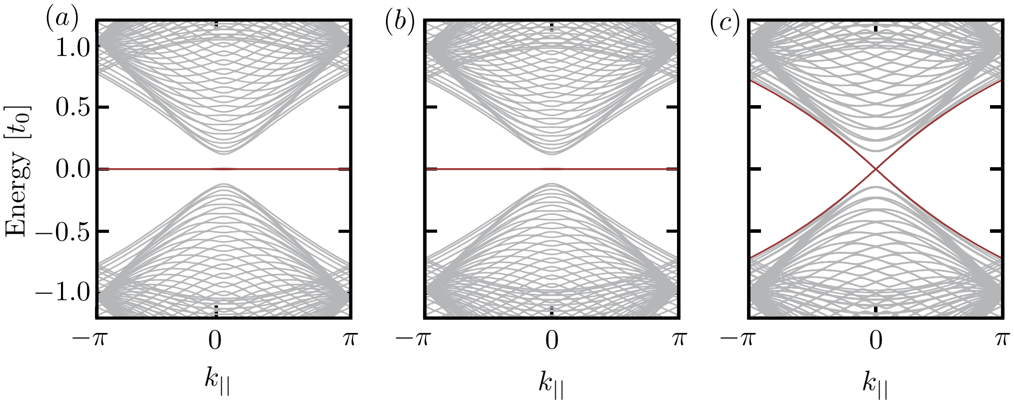

Figure 2.4: (a) The band structures for a ribbon of graphene-zigzag edge with $t_1 = 1.1t_0$. The corresponding winding number is $(1,0)$. (b) The band structures for a ribbon of graphene-zigzag edge with $t_1 = 0.9t_0$. The corresponding winding number is $(0,1)$. (c) The band structure for the interface between two regions $t_1 = 1.1t_0$ and $t_1 = 0.9t_0$ with graphene-zigzag type boundary. All figures are cited from [27].

Chapter 3

$\mathbb{Z}_2$ phase in a chiral honeycomb lattice

In this chapter, we discuss the topological phases of a model on a chiral honeycomb lattice, characterized by broken mirror symmetry, as a natural extension of the Wu-Hu model. When attempting to introduce mirror symmetry breaking in a Hermitian manner to the Wu-Hu model, one must inevitably break sublattice symmetry (Sec. 3.2). As a result, the argument based on the mirror winding number, which combines mirror and sublattice symmetries, discussed in the previous section, can no longer be applied. However, even in such cases, band inversion and edge states (Sec. 3.3, 3.4) emerge, and a topological invariant can still be introduced by incorporating C_2T symmetry (Sec. 3.5). The contents in this Chapter have been published in Ref. [100].

3.1 Introduction

First, let us clarify the usage of the term “chiral” in this thesis. An object is referred to as “chiral” if it cannot be superimposed onto its mirror image, and this geometric property is known as “chirality.” A familiar example of chirality is our hands. As shown in FIG. 3.1, a right hand subjected to a mirror operation becomes a left hand, but the left and right hands cannot be superimposed. In this sense, our hands are chiral objects.

Chirality and its associated physical phenomena frequently appear, especially in classical systems such as soft matter. For example, in bacterial colonies, a representative case of active matter, individual bacteria are chiral objects due to their rotation at the head and tail. This chirality manifests as directed flows in cylindrical boundary conditions, as confirmed experimentally and theoretically [101, 102]. Similarly, in the blue phase of liquid crystals, chiral vortex-like alignment structures called half-skyrmions spontaneously form hexagonal lattices with C_6 symmetry on the scale of hundreds of nanometers [103].

Furthermore, topological phases are expected to emerge in principle even in these systems. For instance, in active matter systems, artificial structures called topologi-

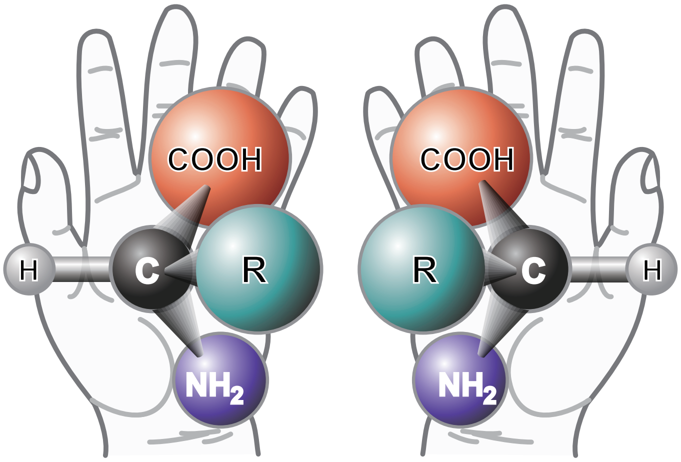

Figure 3.1: Schematic illustration of chirality. Two enantiomers of a generic amino acid that are chiral, as well as our hands. This figure is cited from Wikipedia.

cal active metamaterials that break time-reversal symmetry have been proposed, using lattice channels filled with spontaneously flowing active liquids [104]. Although these systems do not explicitly break mirror symmetry, their study reveals new topological functionalities. In liquid crystals, while studies on topological phases are limited, electromagnetic analyses of periodic structures in nematic and blue phases-conducted mainly in the context of display design-hint at the potential realization of topological photonic crystal phases [105].

With this context in mind, we have investigated topological phases on a chiral honeycomb lattice as an extension of the Wu-Hu model. Our focus is on topological phases in systems where mirror symmetry is broken. Typically, when considering band topology in classical setups, lattice models corresponding to such systems implicitly assume mirror symmetry, and it makes them unsuitable for discussing topological phases in chiral classical systems. Thus, our research has focused on how to implement a minimal model that describes chiral classical systems.

Breaking mirror symmetry is not only crucial for exploring classical systems but also for addressing a fundamental issue inherent in the Wu-Hu model: how sublattice symmetry breaking influences topological phases. As we will see below, breaking mirror symmetry in a Hermitian framework minimally requires introducing next-nearest-neighbor hopping in lattice models, which also breaks sublattice symmetry. Consequently, our proposed model cannot be topologically trivial extension from the Wu-Hu model that was understood through a combination of sublattice and mirror symmetries, as discussed in Sec. 2.4. This viewpoint is significant when discussing the Wu-Hu model in real materials, as sublattice symmetry is generally broken in reality. Thus, characterizing topological phases based on the sublattice symmetry is insufficient. We address how these issues are resolved by employing the Dirac equation and Wilson loop analysis.

3.2 Model

We first consider a two-dimensional tight-binding model on a honeycomb lattice with NN and NNN hoppings. Figure 3.2 presents the schematic illustration of the model and the geometry. Due to the modulation in hoppings, the primitive unit cell is a hexagon containing six sites instead of two in the pristine honeycomb lattice model. Then, the unit vectors for the modulated honeycomb lattice are $\boldsymbol{a}_1 = (3a_0/2, \sqrt{3}a_0/2)^T$ and $\boldsymbol{a}_2 = (-3a_0/2, \sqrt{3}/2)^T$, where a_0 is the lattice constant for the pristine case. The Hamiltonian reads

$$H = \sum_{\langle i,j \rangle} t_{ij} c_i^\dagger c_j + \sum_{\langle\langle i',j' \rangle\rangle} t_{i'j'} c_{i'}^\dagger c_{j'}. \tag{3.1}$$

Here $\langle i, j\rangle$ denotes nearest neighbors, and $\langle\langle i', j'\rangle\rangle$ denotes next nearest neighbors. As NN hoppings, we consider both intrahexagon hopping t_0 and interhexagon hopping t_1, as depicted in FIG.3.2 by black bonds and red bonds respectively. On the other hand, as NNN hoppings, we only consider interhexagon hopping. Furthermore, we classify the interhexagon hoppings into two types, and respectively assign t_2 and t_3 to introduce chirality on the system. The two types of hoppings are illustrated as green and orange bonds in FIG.3.2.

The reflection symmetry breaking can be introduced by setting t_2 unequal to t_3. Indeed, as depicted in FIG.3.3, the green bonds are the mirror image of the orange bonds, where the reflection plane is on the blue line. This means that the system becomes chiral when $t_2 \neq t_3$, because the role of t_2 and t_3 are swapped before and after the reflection operation.

In the following, we limit ourselves to the case with the real-valued hopping t_0, t_1, t_2, t_3, unlike Haldane model [9]. This makes it straightforward to realize the model in any artificial systems like photonic crystals. Without complex-valued hoppings, the time-reversal symmetry is preserved in our setup. We emphasize that we handle the case of $t_2 \neq t_3$, in which the system becomes chiral.

3.3 Band structures and effective Hamiltonian

To elucidate the topological properties of our chiral model given by Hamiltonian Eq. (3.1), we calculate its energy dispersion. By Fourier transforming Eq. (3.1), the

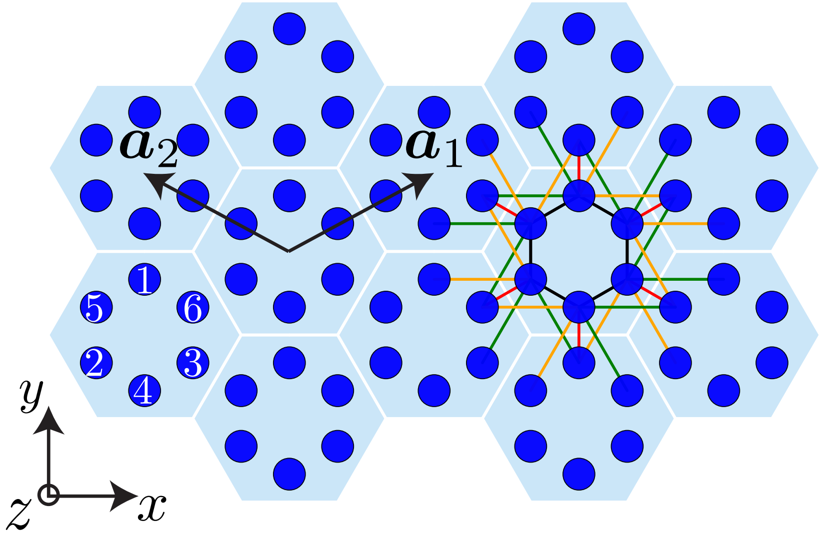

Figure 3.2: Schematic illustration of the tight-binding model treated in this article. The NN hoppings inside unit cells are denoted by t_0 (black solid lines), and the NN hoppings between unit cells are denoted by t_1 (red solid lines). The NNN hoppings are also introduced as t_2 (green solid lines) and t_3 (orange solid lines).

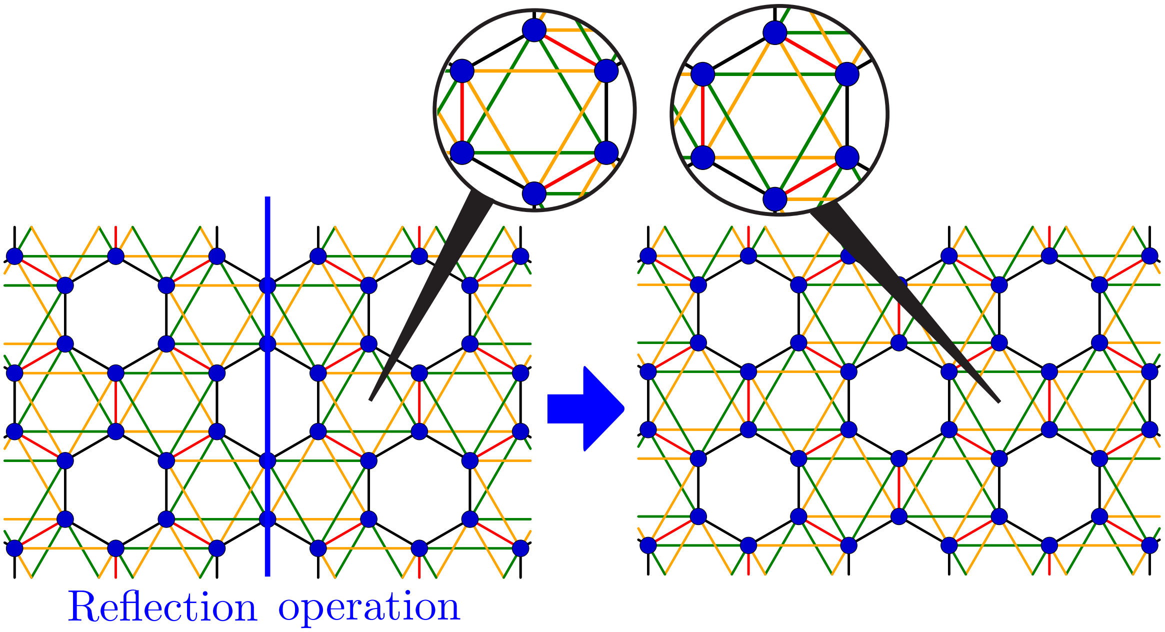

Figure 3.3: The system after the reflection operation. Due to the existence of NNN hoppings t_2 and t_3 the reflected system can not be superposed onto the original one.

Hamiltonian as a function of mementum $\boldsymbol{k}$ yields

$$H(\boldsymbol{k}) = \begin{pmatrix} F(\boldsymbol{k}) & D(\boldsymbol{k}) \\ D(\boldsymbol{k})^\dagger & F(\boldsymbol{k})^T \end{pmatrix},$$

$$D(\boldsymbol{k}) = \begin{pmatrix} t_1 e_1^*(\boldsymbol{k}) e_2^*(\boldsymbol{k}) & t_0 & t_0 \\ t_0 & t_1 e_1(\boldsymbol{k}) & t_0 \\ t_0 & t_0 & t_1 e_2(\boldsymbol{k}) \end{pmatrix}, \tag{3.2}$$

$$F(\boldsymbol{k}) = \begin{pmatrix} 0 & t_2 e_1^*(\boldsymbol{k}) + t_3 e_1^*(\boldsymbol{k}) e_2^*(\boldsymbol{k}) & t_2 e_1^*(\boldsymbol{k}) e_2^*(\boldsymbol{k}) + t_3 e_2^*(\boldsymbol{k}) \\ t_2 e_1(\boldsymbol{k}) + t_3 e_1(\boldsymbol{k}) e_2(\boldsymbol{k}) & 0 & t_2 e_2^*(\boldsymbol{k}) + t_3 e_1(\boldsymbol{k}) \\ t_2 e_1(\boldsymbol{k}) e_2(\boldsymbol{k}) + t_3 e_2(\boldsymbol{k}) & t_2 e_2(\boldsymbol{k}) + t_3 e_1^*(\boldsymbol{k}) & 0 \end{pmatrix}, \tag{3.3}$$

where $e_l(\boldsymbol{k}) = e^{i\boldsymbol{k}\cdot\boldsymbol{a}_l}$ $(l = 1, 2)$.

Figure 3.4 shows plots of the energy dispersion for the Hamiltonian Eq. (3.3) by setting the hopping energies t_0, t_1, t_2, t_3 to several typical values. Importantly, a band inversion occurs by changing the value of t_1 appropriately. This can be confirmed by plotting the values of $|\langle u_{\boldsymbol{k}}^n | d_+ \rangle|$ as line colors, where $|u_{\boldsymbol{k}}^n\rangle$ is the periodic part of Bloch function labeled by index n and Bloch wave vector $\boldsymbol{k}$. We see that the colors of the band edges near $E = 0$ at the Γ-point are exchanged between Figs. 3.4(a) and 3.4(c). For the system with $t_1 = t_0$ [Fig. 3.4(b)], double Dirac cones appear at $E = 0$.

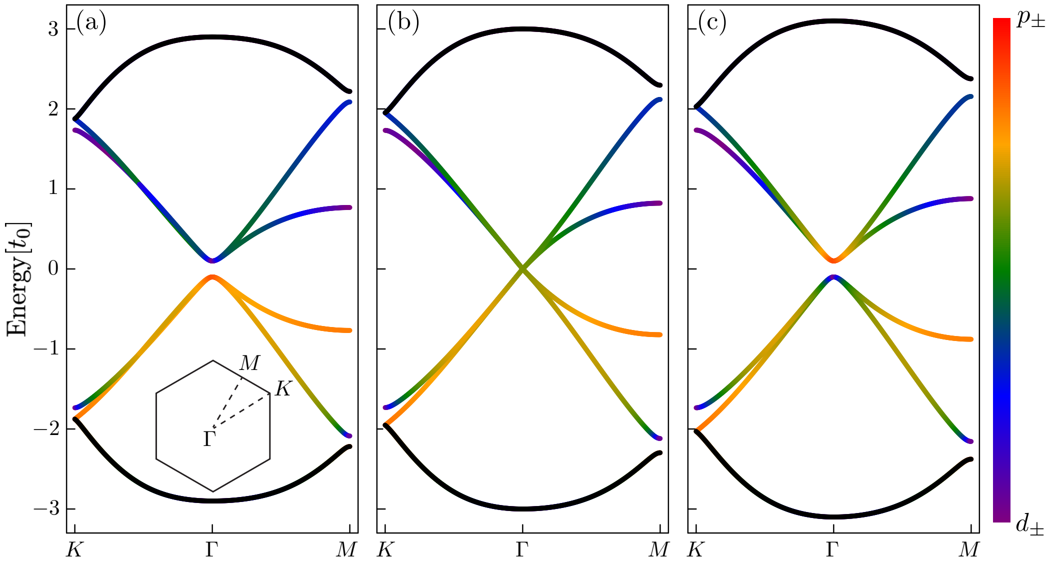

Figure 3.4: Energy dispersions for the system given by Eq.(3.3). In all panels, we set $t_2 = 0.3t_0$ and $t_3 = -0.3t_0$: (a) $t_1 = 0.9t_0$, (b) $t_1 = t_0$, (c) $t_1 = 1.1t_0$. The color maps are for the values of $|\langle u_{\boldsymbol{k}}^n | d_+ \rangle|$. $|p_\pm\rangle$ and $|d_\pm\rangle$ are pseudo-spin modes.

In the low energy region around the Γ point, the effective Hamiltonian can be derived as

$$\mathcal{H}^{(\mathrm{eff})}(k_x,k_y) \simeq \begin{pmatrix} H_+(k_x,k_y) & 0 \\ 0 & H_-(k_x,k_y) \end{pmatrix}, \tag{3.4}$$

where

$$H_\pm(k_x,k_y) = -(t_2+t_3)I + (t_0-t_1)\sigma_z + \frac{t_1|\boldsymbol{a}_1|}{2}(\pm k_x\sigma_x + k_y\sigma_y). \tag{3.5}$$

The derivation is given in Appendix A. This Dirac Hamiltonian Eq. (3.5) clarifies the origin of the band inversion in FIG. 3.4, where the band inversion is induced by varing the hopping energy t_1. In the context of the Dirac Hamiltonian, the sign of the Dirac mass $m := t_0 - t_1$ can be flipped by changing t_1, which explains the origin of the gap and infers that the two states in Figs. 3.4(a) and 3.4(c) are topologically distinct with each other. We note that, in this expansion up to first order in the wavevectors, t_2 and t_3 only result in a constant energy shift and do not contribute to the band inversion.

For simplicity, we focus on the sign of the mass term m to pick up topological characters of the system, namely we say two states with the opposite signs of m topologically distinct. Strictly speaking, a topological index often requires information of global structure of Bloch wave functions in the entire Brillouin zone (as the Chern number), not only information of the band order at a single momentum (Γ-point in this case). However, a description by a Dirac equation with spatial modulation in its mass term gives a universal understanding of topologically protected edge/interface states. This will be confirmed in the following analysis.

We note that a complementary view can be given by further analysis using C_2T symmetry. It has been shown that in crystals with C_2T symmetry, the Wannier band can be utilized to define a $\mathbb{Z}_2$ index [106]. While next-nearest-neighbor hopping terms break sublattice symmetry in our model, C_2T symmetry remains intact. Therefore, rigorous $\mathbb{Z}_2$ classification can still be applied. We have included a discussion on Wilson loops in Sec. 3.5.

3.4 Topological edge states

In this section, we analyze localized states at the boundary between two regions with distinct topology. We begin with the analytical approach using the low-energy effective Dirac theory. Let us consider a case where the periodic boundary condition is imposed only in the x direction. There is a boundary normal to the y direction where the sign of the mass term switches: $t_0 - t_1 = m_0 > 0$ for $y > 0$ and $t_0 - t_1 = -m_0$ for $y < 0$. In the x direction, k_x is a good quantum number because of the existence of the periodic boundary condition. In the y direction, however, we apply a continuous approximation by replacing k_y with $-i\partial_y$ to take into account the spatial dependence of m. The eigenvalue equation of $H_+(k_x,k_y)$ then becomes

$$\begin{pmatrix} -(t_2+t_3)+m_0\mathrm{sgn}(y) & v(k_x-\partial_y) \\ v(k_x+\partial_y) & -(t_2+t_3)-m_0\mathrm{sgn}(y) \end{pmatrix}\begin{pmatrix}\phi_1\\ \phi_2\end{pmatrix} = E\begin{pmatrix}\phi_1\\ \phi_2\end{pmatrix}, \tag{3.6}$$

where $v := t_1|\boldsymbol{a}_1|/2$. Rewriting this equation in a new basis $\phi_\pm = \phi_1 \pm \phi_2$, the eigenvalue equation yields

$$\begin{pmatrix} -(t_2+t_3)+vk_x & m_0\mathrm{sgn}(y)+v\partial_y \\ m_0\mathrm{sgn}(y)-v\partial_y & -(t_2+t_3)-vk_x \end{pmatrix} \begin{pmatrix} \phi_+ \\ \phi_- \end{pmatrix} = E \begin{pmatrix} \phi_+ \\ \phi_- \end{pmatrix}. \tag{3.7}$$

When $m_0/v > 0$, the solution obtained under the conditions that the wavefunction converges at $y = \pm\infty$ and is continuous at $y = 0$ is

$$E_+ = -(t_2+t_3) - vk_x, \begin{pmatrix} \phi_+ \\ \phi_- \end{pmatrix} \propto \begin{pmatrix} 0 \\ \exp(-(m_0/v)|y|) \end{pmatrix}. \tag{3.8}$$

The eigenvalue equation for H_- is obtained by simply replacing k_x of Eq.(3.7) by $-k_x$. The eigenenergy and states become

$$E_- = -(t_2+t_3) + vk_x, \begin{pmatrix} \phi_+ \\ \phi_- \end{pmatrix} \propto \begin{pmatrix} 0 \\ \exp(-(m_0/v)|y|) \end{pmatrix}. \tag{3.9}$$

Thus, by solving the eigenvalue equations of $\mathcal{H}^{(\mathrm{eff})}$, one obtains the solutions such that the eigenenergies $E_\pm$ intersect linearly at $E_0 := -(t_2+t_3)$. In addition, the corresponding eigenstates are exponentially localized at the boundary $y = 0$. These localized states are protected by the difference of topology, i.e. the difference of the sign of mass term in Eq. (3.5), which confirms the usefulness of the mass-term based topological classificaiton.

Next, we move on to the numerical approach using the tight-binding model. In order to discuss boundary states, we consider a system where a region of $t_1 = 1.1t_0$ is sandwiched between two regions of $t_1 = 0.9t_0$ as shown in FIG. 3.5(a). Note that $\boldsymbol{a}_1$ direction is horizontal in FIG. 3.5(a). Then, periodic boundary conditions are imposed on $\boldsymbol{a}_1$ and $\boldsymbol{a}_2$ directions, respectively. With this construction of the interface, $\boldsymbol{a}_2$ remains to be a unit vector, i.e., there is no superstructure in $\boldsymbol{a}_2$ direction, and we can calculate energy dispersion as a function of the momentum along the interface $k_\parallel$. The calculated dispersion is in FIG. 3.5(b), showing new states in the bulk gap that intersect linearly at $k_\parallel = 0$, which is consistent with the analytical discussions above. Plotting the square norm of the corresponding wave function (FIG. 3.5(c)) also shows that it is localized at the boundaries.

3.5 Berry bands and $\mathbb{Z}_2$ index

In this section, we present a complementary perspective to the Dirac equation-based analysis developed in the previous sections, by discussing the Berry bands using the Wilson loop framework. We consider a closed path $\mathcal{L}$ in momentum space, and define the Wilson loop operator for $\mathcal{L}$ as

$$\hat{W}_{\mathcal{L}}^{\{n\}}(\boldsymbol{k_1}) := \hat{P}(\boldsymbol{k}_1)\hat{P}(\boldsymbol{k}_N)\cdots\hat{P}(\boldsymbol{k}_2)\hat{P}(\boldsymbol{k}_1), \tag{3.10}$$

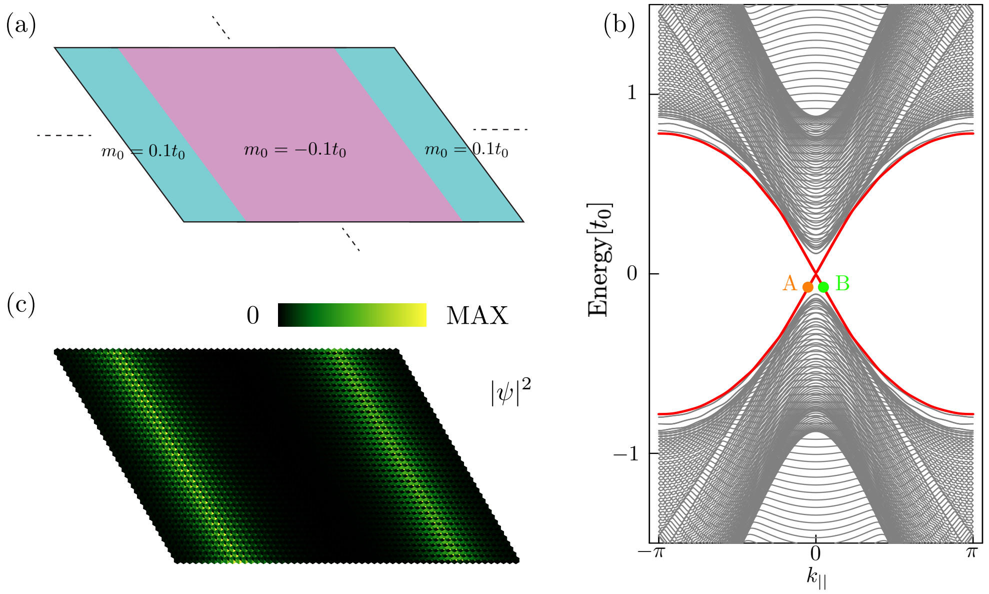

Figure 3.5: The hopping enegies of chirality are set to $t_2 = 0.3t_0$ and $t_3 = -0.3t_0$. (a) Schematic illustration of the system being simulated, with a region of $t_1 = 1.1t_0$ bounded by two regions of $t_1 = 0.9t_0$. (b) energy dispersions (c) The square of wave functions corresponding to A and B in (b). They have the same value because of time reversal symmetry.

where $\hat{P}(\boldsymbol{k}_i)$ is a projection operator onto a chosen subspace$\{n\}$:

$$\hat{P}(\boldsymbol{k}_i) := \sum_{n\in\{n\}} |u_n(\boldsymbol{k}_i)\rangle \langle u_n(\boldsymbol{k}_i)| \,. \tag{3.11}$$

Here, the sequence $\{\boldsymbol{k}_i\}_{i=1}^N$ represents closely spaced points along $\mathcal{L}$. The definition of the Wilson loop operator used here is consistent with the one introduced in Chapter 2. Indeed, in Chapter 2, we have discussed the matrix representation of the Wilson loop operator.

The eigenvalues and engenstates of the Wilson loop operator are obtained as follows. By using Bloch wave functions on the initial momentum $\boldsymbol{k}_1$, we can express it as a unitary matrix:

$$[W^{\{n\}}(\boldsymbol{k}_1)]_{ij} := \langle u_i(\boldsymbol{k}_1)| \hat{W}_{\mathcal{L}}^{\{n\}}(\boldsymbol{k}_1) |u_j(\boldsymbol{k}_1)\rangle \,. \tag{3.12}$$

The matrix $W^{\{n\}}(\boldsymbol{k}_1)$ can be diagonalized by a unitary matrix $V(\boldsymbol{k}_1)$, which satisfies

$$[V^\dagger(\boldsymbol{k}_1)W^{\{n\}}(\boldsymbol{k}_1)V(\boldsymbol{k}_1)]_{ij} = \delta_{ij}\exp(i\gamma_i), \tag{3.13}$$

where γ_i is a gauge-invariant geometric phase, also known as a Berry phase. Therefore, the eigenstates of the Wilson loop are

$$|\tilde{u}_i(\boldsymbol{k}_1)\rangle = \sum_l [V(\boldsymbol{k}_1)]_{il} |u_l(\boldsymbol{k}_1)\rangle \,, \tag{3.14}$$

with the corresponding eigenvalue being $\exp(i\gamma_i)$.

3.5.1 Berry bands

Let us now consider Wilson loops around an infinitesimally small path $\mathcal{L}'$ which enclose a point $\boldsymbol{k}$. Hereafter, to elucidate the topological nature of our system, we focus on the valence bands. First, we construct the Wilson loops as:

$$\hat{W}^{\mathrm{val}}_{\mathcal{L}'}(\boldsymbol{k}) := \hat{P}_{\mathrm{val}}(\boldsymbol{k}_1)\hat{P}_{\mathrm{val}}(\boldsymbol{k}_N)\cdots\hat{P}_{\mathrm{val}}(\boldsymbol{k}_2)\hat{P}_{\mathrm{val}}(\boldsymbol{k}_1). \tag{3.15}$$

Here we denote closely spaced points along the path $\mathcal{L}'$ as $\{\boldsymbol{k}_i\}_{i=1}^{N}$s, and $\hat{P}_{\mathrm{val}}(\boldsymbol{k}_i)$ is the projection operator onto the full valence band space.

Since the Wilson loop operator is unitary, we can define an associated Hermitian operator $\hat{H}_{\mathcal{F}}(\boldsymbol{k})$, given by

$$\hat{H}_{\mathcal{F}}(\boldsymbol{k}) := \lim_{A\to 0}\left[\frac{-i\log\hat{W}^{\mathrm{val}}_{\mathcal{L}'}(\boldsymbol{k})}{A}\right], \tag{3.16}$$

where A is the area enclosed by $\mathcal{L}'$. The matrix form of this Hermitian operator is

$$[H_{\mathcal{F}}(\boldsymbol{k})]_{ij} = \langle u_i(\boldsymbol{k})|\,\hat{H}_{\mathcal{F}}(\boldsymbol{k})\,|u_i(\boldsymbol{k})\rangle = \lim_{A\to 0}\left[\frac{-i[\log W^{\mathrm{val}}(\boldsymbol{k})]_{ij}}{A}\right], \tag{3.17}$$

where

$$[W^{\mathrm{val}}(\boldsymbol{k})]_{ij} := \langle u_i(\boldsymbol{k})|\,\hat{W}^{\mathrm{val}}_{\mathcal{L}'}(\boldsymbol{k})\,|u_i(\boldsymbol{k})\rangle\,. \tag{3.18}$$

This matrix $H_{\mathcal{F}}(\boldsymbol{k})$ is Hermitian, and can be diagonalized by a unitary matrix $U(\boldsymbol{k})$ satisfying

$$[U^{\dagger}(\boldsymbol{k})H_{\mathcal{F}}(\boldsymbol{k})U(\boldsymbol{k})]_{ij} = \delta_{ij}\mathcal{F}_i(\boldsymbol{k}), \tag{3.19}$$

where $\mathcal{F}_i(\boldsymbol{k})$ is the non-Abelian Berry curvature. Thus, the eigenvalue problem reads

$$\hat{H}_{\mathcal{F}}(\boldsymbol{k})\,|\tilde{u}'_i(\boldsymbol{k})\rangle = \mathcal{F}_i(\boldsymbol{k})\,|\tilde{u}'_i(\boldsymbol{k})\rangle\,, \tag{3.20}$$

and

$$|\tilde{u}'_i(\boldsymbol{k})\rangle = \sum_l [U(\boldsymbol{k})]_{il}\,|u_l(\boldsymbol{k})\rangle\,. \tag{3.21}$$

Following Ref [106], we refer to these states as Berry bands.

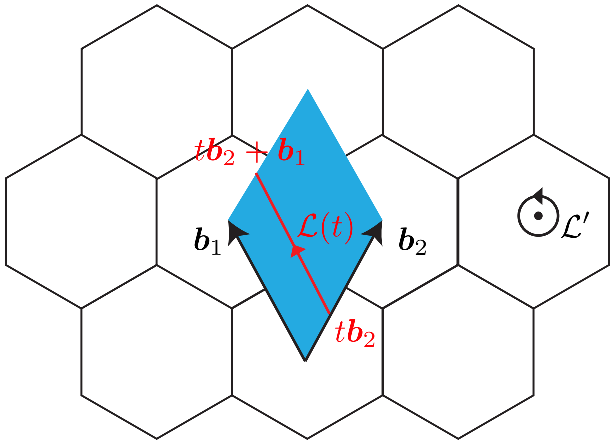

Figure 3.6: Schematic illustration of a path $\mathcal{L}(t)$ where Wilson loops are made on a series of these paths. These paths sweep the Brillouin zone (shaded blue region) as $t : 0 \to 1$.

3.5.2 C_2T-protected $\mathbb{Z}_2$ phase

We first consider the Wannier band structures[1] of the Wilson loop built from projectors onto the three-dimensional valence bands in our model. We have calculated the Wilson loops along a sequence of parallel paths, $\mathcal{L}(t)$, as depicted in FIG. 3.6, where these paths gradually traverse the Brillouin zone as t progresses from $t : 0 \to 1$.

The Wannier band structure, as shown in FIG.3.7, indicate that the total winding of the Wannier band are zero. As mentioned in ref [106, 107], the total Chern number of the valence bands is equivalent to the total spectral winding of Wannier bands, and this result is consistent with the time-reversal symmetry. We note that even in time-reversal symmetric systems, it is known that in topologically nontrivial cases—such as the Kane-Mele model, where the spin degree of freedom is taken into account—the spectral windings of the Wannier bands, modulo 2, correspond to the $\mathbb{Z}_2$ topological invariant [97].

Alternatively, we can utilize the Berry bands introduced in the previous section. In C_2T-symmetric crystals[2], the Hermitian operator $\hat{H}_{\mathcal{F}}(\boldsymbol{k})$ obeys the relation

$$(C_2T)\hat{H}_{\mathcal{F}}(\boldsymbol{k})(C_2T)^{-1} = -\hat{H}_{\mathcal{F}}(\boldsymbol{k}), \tag{3.22}$$

which implies that each Berry curvature in a C_2T-symmetric crystal is either zero or forms a positive/negative pair, as depicted in FIG.3.8. This constraints allows for the $\mathbb{Z}_2$ classification in C_2T-symmetric systems [106].

---

[1] Here, the term "Wannier bands" refers to the flow of hybrid Wannier centers in momentum space, as introduced in Chapter 2.

[2] In the present context, we consider a spinless electronic system. Accordingly, the time-reversal operator T is represented by complex conjugation, that is, $T = K$.

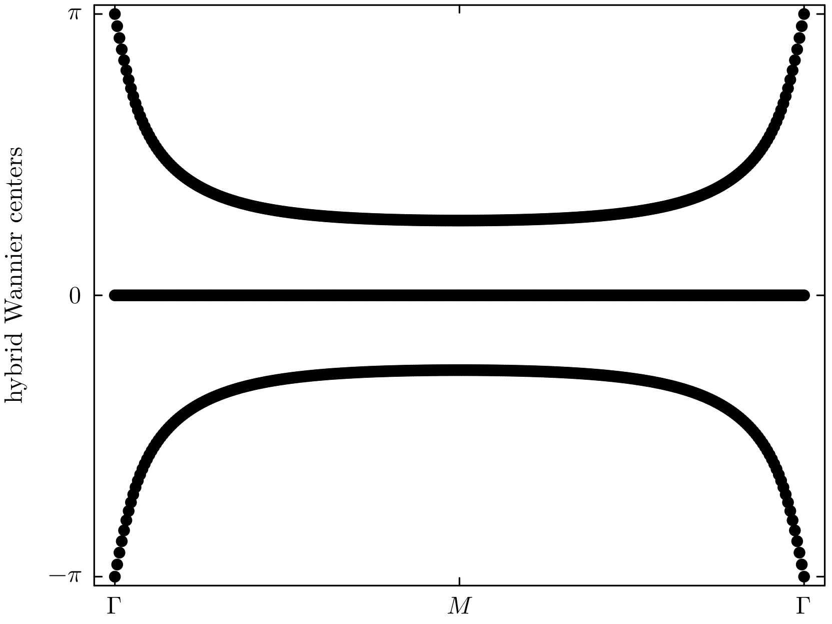

Figure 3.7: Wannier band structures for the topological region made through the valence bands. The total windings of these spectra are zero, as expected from time-reversal symmetry.

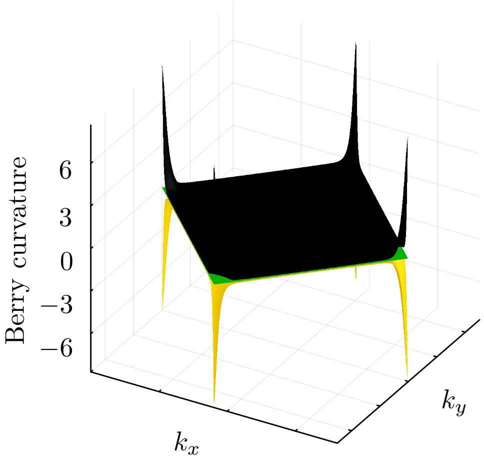

Figure 3.8: Berry curvature derived from the eigenvalue problem Eq.(3.20). As a result of C_2T symmetry, these values are either zero or occur as positive/negative pairs.

Figure 3.9(a) shows the Wannier band structures of the Wilson loop made separately through $\{|\tilde{u}'_i(\boldsymbol{k})\rangle\}_{i=1}^{3}$ for the same parameters as in FIG.3.7. The blue/red markers correspond to the positive/negative parts of the Berry band, while the black markers represent the zero part of the Berry band. There is no mixing, and the windings of the individual spectra are $\{w_{\text{negative}}, w_{\text{zero}}, w_{\text{positive}}\} = \{-1, 0, +1\}$ mod 2. On the other hand, for the trivial region, the windings are $\{w_{\text{negative}}, w_{\text{zero}}, w_{\text{positive}}\} = \{0, 0, 0\}$ mod 2, as indicated in FIG.3.9(b).

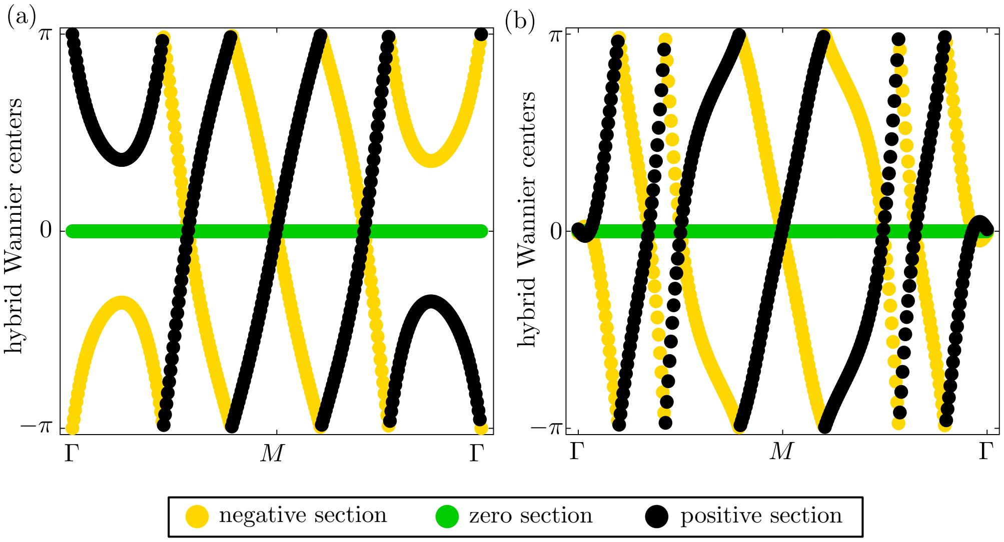

Figure 3.9: (a) Wannier band structure for the topological region made through the Berry bands. These spectra present well-defined nontrivial windings. The corresponding Z$_2$ index is shown to be protected by C_2T symmetry. (b) Wannier band structure for the trivial region made through the Berry bands. These spectra present trivial zero windings.

3.6 Short summary

We propose a novel tight-binding model to describe chiral systems and study its properties using both analytical and numerical methods. First, we numerically compute the bulk energy dispersion and demonstrate that band inversion occurs as the model parameter, i.e., the hopping amplitude, is varied. By performing a perturbative expansion of the Hamiltonian up to the first order in momentum, we show that the band inversion can be understood as a sign change in the mass term of the Dirac equation.

Next, we consider a system composed of two regions with different topological properties and numerically demonstrate the emergence of topological states at their boundary. Furthermore, for a system with a boundary, we analytically confirm the presence of topological states using an effective model based on the Dirac equation.

Finally, as a complementary approach to the Dirac equation analysis, we discussed the $\mathbb{Z}_2$ topological invariant using the Wilson loop formalism. In the present case, the system possesses C_2T symmetry, which allows for a formulation based on Berry bands. We demonstrated that the winding of the hybrid Wannier centers yields the appropriate $\mathbb{Z}_2$ invariant.

Chapter 4

Interface transport in the chiral honeycomb lattice

In Chapter 3, we have proposed a chiral honeycomb lattice model and discussed its topological phases, demonstrating that a $\mathbb{Z}_2$ topological phase can emerge even when mirror symmetry and sublattice symmetry are broken. However, the remaining question concerns how chirality influences physical responses. This is because, in the discussions in Chapter 3, the effect of chirality was limited to inducing a constant shift in the energy eigenvalues. In this chapter, we address this issue by mapping the tight-binding model to a classical system and investigating interface transport phenomena. The contents in this Chapter have been published in Ref. [100]

4.1 Introduction

To begin, we discuss how spring-mass systems can be associated with tight-binding models. For simplicity, let us consider a coupled oscillation system with two masses. We denote the spring constant of the spring connecting the masses as k_1, and the spring constant of the springs connecting each mass to a fixed wall as k_0. The equation of motion is given by

$$\frac{d^2}{d\tau^2}\begin{pmatrix} x_1(\tau) \\ x_2(\tau) \end{pmatrix} = -\begin{pmatrix} k_0+k_1 & -k_1 \\ -k_1 & k_0+k_1 \end{pmatrix}\begin{pmatrix} x_1(\tau) \\ x_2(\tau) \end{pmatrix} =: -\Gamma \begin{pmatrix} x_1(\tau) \\ x_2(\tau) \end{pmatrix}, \tag{4.1}$$

where the mass of the particles is normalized to $m = 1$. Here we denote the position coordinate of the particle as x_i $(i = 1, 2)$, and τ represents time. To determine the normal modes and natural frequencies of this system, we assume a solution of the form $x_i(\tau) = e^{i\omega\tau}\tilde{x}_i$ $(i = 1, 2)$, which yields

$$\Gamma \begin{pmatrix} \tilde{x}_1 \\ \tilde{x}_2 \end{pmatrix} = \omega^2 \begin{pmatrix} \tilde{x}_1 \\ \tilde{x}_2 \end{pmatrix}. \tag{4.2}$$

If we make the correspondence $\Gamma \leftrightarrow H$, $E \leftrightarrow \omega^2$ $\psi_i \leftrightarrow \tilde{x}_i$ $(i = 1, 2)$, this equation can be interpreted as the Hamiltonian of the tight-binding model in quantum systems:

$$H \begin{pmatrix} \psi_1 \\ \psi_2 \end{pmatrix} = E \begin{pmatrix} \psi_1 \\ \psi_2 \end{pmatrix}. \tag{4.3}$$

This correspondence indicates that spring-mass systems provide an excellent platform for simulating lattice models in classical systems. Indeed, they are an effective tool for discussing band topology. For example, lattice models such as the SSH model can be implemented relatively easily [44]. Moreover, by introducing perturbations that break time-reversal symmetry, such as Coriolis forces, one can realize topological phases characterized by the Chern number, analogous to quantum Hall insulators [108]. While we introduced the spring-mass system here for its intuitive simplicity, it is also worth noting that if we reinterpret the position of the masses as the charge stored in capacitors and the spring constants as inductance, the system can also be viewed as an LC circuit system [109].

4.2 Model

Let us now generalize the discussion of Sec. 4.1. Here we specifically consider a mass-spring system in which potential energy can be written as

$$V\{\boldsymbol{x}\} = \frac{1}{2}\sum_i \sum_{j>i} k_{ij}(x_i - s_{ij}x_j)^2 + \frac{1}{2}\sum_i \epsilon_i x_i^2, \tag{4.4}$$

as a function of dynamical variables $\boldsymbol{x}$. The number of components in $\boldsymbol{x}$ corresponds to the number of degrees of freedom in a given system. The first term represents couplings between different degrees of freedom, with spring constants $k_{ij} > 0$ and s_{ij} being $+1$ or -1. The way to choose ± 1 for s_{ij}s in a spring-mass model is explained in FIG. 4.1. When a spring stores elastic energy for anti-phase motion of two connected mass points, $s_{ij} = 1$ for this spring, while when it stores elastic energy for in-phase motion of two connected mass points, $s_{ij} = -1$ for this spring. The second term, introduced for later convenience, is a local term that, in a spring-mass model, can be understood as a connection between the mass and the ground. Here ϵ_i is positive. The dynamical matrix of the system is given by

$$\Gamma_{ij} = \frac{\partial^2 V}{\partial x_i \partial x_j} = \left(\epsilon_i + \sum_l k_{il}\right)\delta_{ij} - s_{ij}k_{ij}. \tag{4.5}$$

By appropriately choosing ϵ_is, k_{ij}s and s_{ij}s such that $\epsilon_i + \sum_l k_{il}$ is equal to a constant ϵ independent of i, and that $s_{ij}k_{ij}$, which can be positive or negative, is equal to the hopping energies of the quantum counterpart, the dynamical matrix Γ can be written as

$$\Gamma_{ij} = \epsilon\delta_{ij} - h_{ij}, \tag{4.6}$$

where h_{ij} is hopping energies in the Hamiltonian. By setting ϵ to be sufficiently large, Γ can be positive definite. Thus, one can construct a classical system where its dynamical matrix Γ is equal to H (with a constant shift of ϵ).

After establishing the mapping of Eq. (4.6), the band structure of the Hamiltonian (3.1) has two interpretations: the energy spectra in the quantum system and the spectra of the square of the frequency (modified by the constant shift ϵ) in the classical system. For convenience, we have investigated the topological properties (see Chapter 3) by using the Hamiltonian H, whereas we discuss the interface transport on a classical ribbon structure with the dynamical matrix Γ (Sec. 4.3), since the coupling with external forces can be understood more intuitively in classical systems.

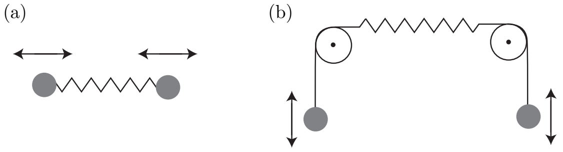

Figure 4.1: The physical meaning of s_{ij} in a spring-mass model. (a)$s_{ij} = +1$. The masses are connected by a spring directly, then the spring acquires elastic energy for *anti*-phase oscillation. (b)$s_{ij} = -1$. The pulleys change the coordinate axes, and s_{ij} is now negative. In this case the spring acquires elastic energy for *in*-phase oscillation.

4.3 Interface transport

So far we have seen that the effect of chirality does not manifest itself in the topological classification or the existence of topological edge states, because unequal t_2 and t_3 just lead to the constant shift of the eigenvalues of the effective Hamiltonian. In this section, we discuss how chirality affects the interface transport by considering the dynamics of a classical harmonic-oscillator system with boundaries at which energy is injected [109]. One reason for using a classical system rather than a quantum one is that the meaning of the energy injection can be much more intuitively caught in a classical system as shown below (the energy injection is simply modeled by forced oscillation). Another reason is that the study of modulated honeycomb lattice model has been greatly developed in the context of classical systems like photonic crystals.

To calculate the interface transport, we denote dynamical variables by $\boldsymbol{x} = \{x_i\}$. The equation of motion with respect to time τ is written as

$$\frac{d^2\boldsymbol{x}(\tau)}{d\tau^2} = -\Gamma\boldsymbol{x}(\tau) + \boldsymbol{f}^c \cos\Omega\tau. \tag{4.7}$$

Here Γ is a positive-definite dynamical matrix. An external force $\boldsymbol{f}^c \cos\Omega\tau$ is applied to the system with a frequency Ω, and the phase of the force is set to be the same at all sites. One can consider a variety of systems including spring-mass systems and

LC-circuit systems, and the variables $\boldsymbol{x}$ and τ and the parameters are set dimensionless after rescaling of the length and time according to the specific system to be considered.

To facilitate the physical interpretation, let us solve Eq. (4.7) by using the normal mode decomposition [109]. By introducing an orthogonal matrix O that diagonalizes Γ, Eq. (4.7) becomes

$$\frac{d^2\tilde{\boldsymbol{x}}(\tau)}{d\tau^2} = -G\tilde{\boldsymbol{x}}(\tau) + \tilde{\boldsymbol{f}}^{(c)} \cos\Omega\tau, \tag{4.8}$$

where $G = O^T\Gamma O$, $\tilde{\boldsymbol{x}}(\tau) = O^T\boldsymbol{x}(\tau)$ and $\tilde{\boldsymbol{f}}^{(c)} = O^T\boldsymbol{f}^{(c)}$. The expression of Eq. (4.8) in component form becomes

$$\frac{d^2\tilde{x}_l(\tau)}{d\tau^2} = -\omega_l^2\tilde{x}_l(\tau) + \tilde{f}_l^{(c)} \cos\Omega\tau, \tag{4.9}$$

where we label the normal modes by an integer l. The solution of Eq. (4.9) for the initial condition $\boldsymbol{x}(\tau_{\text{init}}) = d\boldsymbol{x}(\tau_{\text{init}})/d\tau = 0$ is

$$\tilde{x}_l(\tau) = a_l^{(c)} \cos\Omega\tau + b_l^{(c)} \cos\omega_l\tau, \tag{4.10}$$

where

$$a_l^{(c)} = \frac{\tilde{f}_l^{(c)}}{\omega_l^2 - \Omega^2}, b_l^{(c)} = -a_l^{(c)}. \tag{4.11}$$

By reconstructing $\boldsymbol{x}(\tau)$ from these $\tilde{x}_l(\tau)$, one can understand the dynamics of the system.

Now, let us return to the interface transport, and consider a specific system illustrated in FIG. 4.2. We consider a ribbon structure of 10 hexagonal unit cells with $t_1 = 1.2$ cladded from both sides by 5 hexagonal unit cells with $t_1 = 0.8$. We also set $t_2 = -t_3 = 0.3$ in all region. To analyze the dynamics, we construct the dynamical matrix of this ribbon structure by the procedure Eq. (4.6), and calculate time evolutions of the intensity at each site i defined as

$$I_i = \frac{1}{2}\Big[\Omega^2 x_i^2 + \left(\frac{dx_i}{d\tau}\right)^2\Big], \tag{4.12}$$

using Eq. (4.7). Equation (4.12) is designed to eliminate the fast oscillation and focus on effective propagation of energy in a long time scale. We also choose $\epsilon = 3.1$ and $\Omega = \sqrt{\epsilon}$. This choice makes Γ positive definite, and Ω is in the bulk gap of the dynamical matrix Γ.

The obtained results are shown in FIG. 4.3. In FIG. 4.3(a), the lines labeled by 1-5 correspond to the intensities in the unit cells 1-5 defined in FIG. 4.2. The energy is injected at the unit cell 1, and the unit cells 2 and 3 (and also 4 and 5) are located at equal distances from the unit cell 1. The obtained difference between the intensities

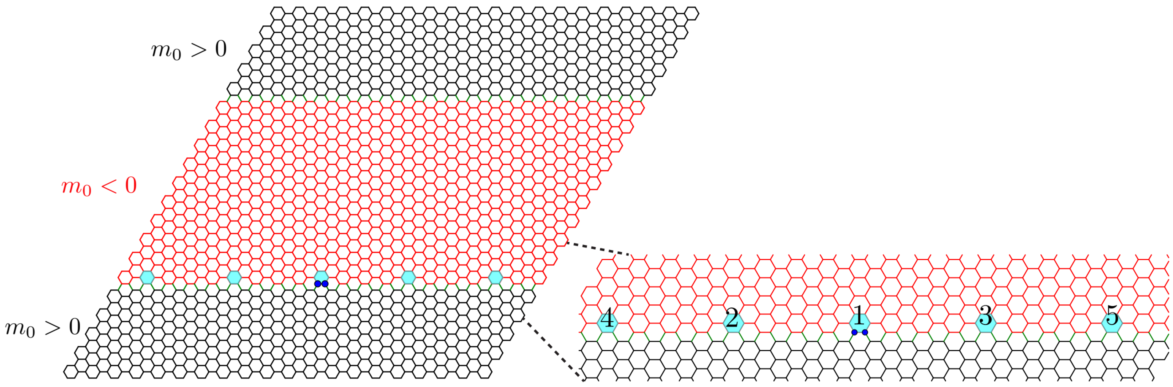

Figure 4.2: Schematic illustration of the system consisting of regions with different topology. we set $t_2 = -t_3 = 0.3$ in all region. For the mass term part, we set $m_0 = -0.2$ for the $m_0 < 0$ region and $m_0 = 0.2$ for the $m_0 > 0$ region. 20 unit cells are lined up in the $\boldsymbol{a}_1$ and $\boldsymbol{a}_2$ directions with periodic boundary condition. We apply the external force $\boldsymbol{f}^{(c)}$ at the points of the boundary indicated by blue dots with the amplitude $f_0 = 1$.

at 2 and 3 (4 and 5) reveals an asymmetric energy propagation caused by the effect of chirality. This novel asymmetry is prohibited in the achiral case $t_2 = t_3 = 0$. It should be noted that t_2 and t_3 are parameters that control the asymmetry. If the values of t_2 and t_3 are interchanged, an asymmetric energy propagation in the opposite direction is observed. In addition, as can be seen from Eqs. (4.10) and (4.11), the contribution of the modes with ω_l close to the frequency Ω dominates the energy propagation. The chirality effects of t_2 and t_3 manifest themselves in $\boldsymbol{x}(\tau)$ and intensity I_i as a linear combination of these multiple modes.

In the achiral case found in the literature, to select right-moving or left-moving interface states, the phase shifts are required in input terminals [110]. Indeed, in photonic crystals, it is necessary to input circularly polarized light in order to selectively excite the pseudospin modes, as discussed in Sec. 1.2.3. In our case, no phase shift is assumed in the forced oscillation term, which gives another way to control energy propagation.

4.4 Short summary and discussion

We numerically compute the energy flow by mapping our system to a classical system, and have discovered a novel asymmetric edge current induced without any phase tuning at input terminals. These considerations could be a building block in exploring chiral topological materials.

As noted in Sec. 4.3, experimental realization of the system proposed in the present study would be more promising in classical systems because the fabrication of the system and the tuning of the interactions will be easier than for quantum systems. Photonic crystal of a dielectric material [28, 111] could be one direction, and top-down fabrication

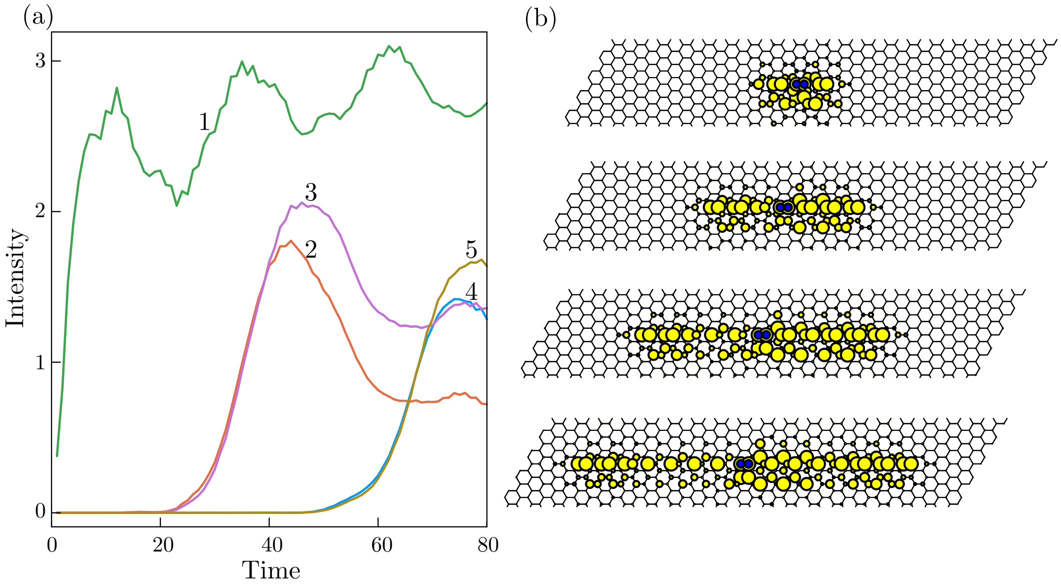

Figure 4.3: (a) Time evolution of Intensity. The labels 1 to 5 correspond to those in FIG.4.2. Intensity in this figure is the sum over the six sites in the blue hexagon in FIG.4.2. (b) Real space plot of the propagation of Intensity I_i. We show snapshots at $\tau = 15, 30, 45, 60$. An asymmetric propagation is achieved due to chirality.

techniques now enable the realization of topological photonics in the visible wavelength regime [112]. Careful fabrication of chiral structures would provide an ideal platform for the experimental verification of the asymmetric transport discussed in Sec. 4.3. Self-organization of chiral soft materials could also be used for the preparation of systems that allows the investigation of chiral transport phenomena, and their ideal conditions could be achieved by the tunability of the structural properties of the soft material by external stimuli. Recently self-assembly of bowtie-shaped nanoparticles has been shown to exhibit tunable chiral photonic properties [113]. Chiral liquid crystals [114] can also offer a platform for self-organized tunable chiral structures, and a hexagonal lattice of skyrmions exhibited by a chiral liquid crystal [103] could host asymmetric transport phenomena in the visible wavelength regime. Classical mechanics of course provides a clue to the realization of systems for chiral topological transport phenomena, such as mass-spring systems discussed in Sec.4.3 [115], and spinning top systems [108]. We hope that the present study will stimulate experimental studies towards the realization and observation of asymmetric topological transport phenomena in a system with time-reversal symmetry.

Chapter 5

Topological quadrupole-like phase in an extra-site model

In this chapter, we discuss a perturbative method to realize the topological quadrupole phase. In the BBH model, discussed in Sec. 1.1.5 and Sec. 2.3.2, the sign flip of hopping terms plays a critical role in the emergence of the topological quadrupole phase. Here, we demonstrate how introducing extra sites can effectively induce such sign flip, thereby pseudo-replicating the characteristics of the topological quadrupole phase.

5.1 Introduction

A general scheme for inducing local sign flips of the hopping amplitudes is often regarded as important in the study of topological insulators. This is because implementing sign flips allows, in principle, the construction of models in which a π-flux is effectively inserted into specific plaquettes using only real hopping terms. Such plaquettes with inserted π-flux act as zero-dimensional defects and are known to be useful for distinguishing between different topological phases [116].

From the perspective of inserting π-fluxes by flipping the signs of hopping terms, the BBH model discussed in Sec. 1.1.5 can be viewed as a model in which all plaquettes are threaded by a π-flux. As discussed in Sec. 2.3.2, the sign flip of the hopping terms is essential for the emergence of the topological quadrupole phase. Realizing such a model, which intrinsically involves both positive and negative hopping amplitudes, poses significant challenges in conventional solid-state systems. However, various platforms beyond traditional electronic systems—such as photonic crystals [117], optical resonators [118], acoustic systems [119], microwave setups [120], and electrical circuits [121]—offer flexible means to implement sign flips, thereby enabling experimental realizations of the BBH model.

Although these methods effectively invert hopping signs, they often rely heavily on the symmetry of the underlying model. For example, in studies implementing the BBH model in photonic crystals [117], the symmetry of the square lattice of the system has been fully utilized by mixing of orbitals with distinct parity representations, such as s and p orbitals.

In this work, we propose a different approach by introducing extra sites between the target sites where the hopping sign needs to be reversed. This method leverages perturbative corrections to achieve sign inversion. A notable advantage of this approach is that it does not depend on specific symmetries of the system, making it a more general and systematic method. In the following sections, we apply this framework to the BBH model and evaluate whether it can exhibit behavior similar to the topological quadrupole phase.

5.2 Model

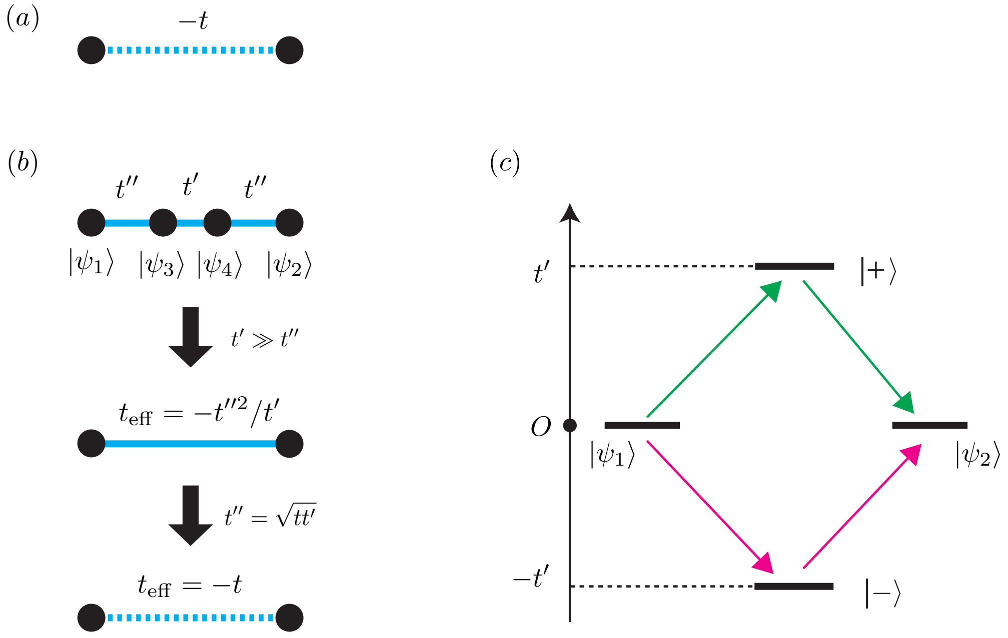

Figure 5.1: The basic idea of the Extra-site model. (a) The desired hopping configuration, where the hopping sign locally flips. (b) Insertion of extra-sites: When the hopping t' is significantly larger than t'', perturbation theory applies, leading to an effective sign inversion of the hopping. (c) Second-order perturbation process: The hopping occurs via either a bonding or an antibonding orbital as an intermediate state.

We start by outlining the fundamental concept of the extra-site model. Suppose we aim to implement a hopping term $-t$ between two sites, labeled as 1 and 2. To achieve the sign flip without directly flipping the sign of the bare hoppings, we consider the following scheme: let us introduce two extra sites, labeled as sites 3 and 4, and set the hopping term between them as t'. The eigenstates of this two-site system split into bonding and antibonding states, with eigenvalues:

$$E_{\pm} = \pm t', \quad |\pm\rangle = \frac{1}{\sqrt{2}}(|\psi_3\rangle \pm |\psi_4\rangle) \tag{5.1}$$

Here, we denote the antibonding and bonding states as $|+\rangle$ and $|-\rangle$, respectively. Next, we place the original sites 1 and 2 to the left of site 3 and to the right of site 4, respectively, and weakly couple them with $t'' \ll t'$. Using second-order perturbation theory, the effective hopping t_{ij} $(i, j = 1, 2)$ can be evaluated as

$$t_{11} = \sum_{\alpha=\pm} \frac{\langle\psi_1| H_{\text{system}} |\alpha\rangle \langle\alpha| H_{\text{system}} |\psi_1\rangle}{E_1 - E_\alpha} = \frac{t''^2}{2(-t')} + \frac{t''^2}{2t'} = 0, \tag{5.2}$$

$$t_{12} = \sum_{\alpha=\pm} \frac{\langle\psi_1| H_{\text{system}} |\alpha\rangle \langle\alpha| H_{\text{system}} |\psi_2\rangle}{E_1 - E_\alpha} = \frac{t''^2}{2(-t')} + \frac{-t''^2}{2t'} = -\frac{t''^2}{t'}, \tag{5.3}$$

$$t_{21} = \sum_{\alpha=\pm} \frac{\langle\psi_2| H_{\text{system}} |\alpha\rangle \langle\alpha| H_{\text{system}} |\psi_1\rangle}{E_1 - E_\alpha} = \frac{t''^2}{2(-t')} + \frac{-t''^2}{2t'} = -\frac{t''^2}{t'}, \tag{5.4}$$

$$t_{22} = \sum_{\alpha=\pm} \frac{\langle\psi_2| H_{\text{system}} |\alpha\rangle \langle\alpha| H_{\text{system}} |\psi_1\rangle}{E_1 - E_\alpha} = \frac{t''^2}{2(-t')} + \frac{t''^2}{2t'} = 0. \tag{5.5}$$

For the on-site hopping terms t_{11}, t_{22}, the contributions from the bonding and antibonding orbitals cancel each other out, resulting in zero. Furthermore, for the inter-site hopping, with fine-tuning such that $t' = \sqrt{tt''}$, the effective hopping term becomes

$$t_{\text{eff}} := t_{12} = t_{21} \simeq -t. \tag{5.6}$$

Thus, we can achieve an effective sign flip of the hopping term.

We now apply this concept to the BBH model. In this case, extra sites are inserted between sites connected by bonds with hopping amplitude $-\gamma$ and $-\lambda$. As depicted in FIG. 5.2, for bonds with $-\gamma$, we add extra sites and assign hopping terms γ'', γ', and γ'' with $\gamma' = \sqrt{\gamma\gamma''}$. Similarly, for bonds with $-\lambda$, we also add extra sites and assign hopping terms λ'', λ', and λ'' with $\lambda' = \sqrt{\lambda\lambda''}$. Based on the above analysis, this model is expected to effectively induce the inversion of hopping signs, thereby pseudo-replicating the topological quadrupole phase.

Here, we note the symmetry of this modified model. The original BBH model is invariant under generalized mirror operations $\tilde{M}_x$ and M_y, including the freedom of gauge transformations. As discussed in Chapter 2, this symmetry guarantee the emergence of the topological quadrupole phase, characterized by a $\mathbb{Z}_2 \times \mathbb{Z}_2$ classification. When extra sites are added, however, the system no longer remains invariant under the mirror operation $\tilde{M}_x$. As a result, the original $\mathbb{Z}_2 \times \mathbb{Z}_2$ classification is no longer applicable. Nevertheless, the mirror symmetry M_y remains intact, and the structure of the Wilson spectrum is preserved (see Sec. 5.5).

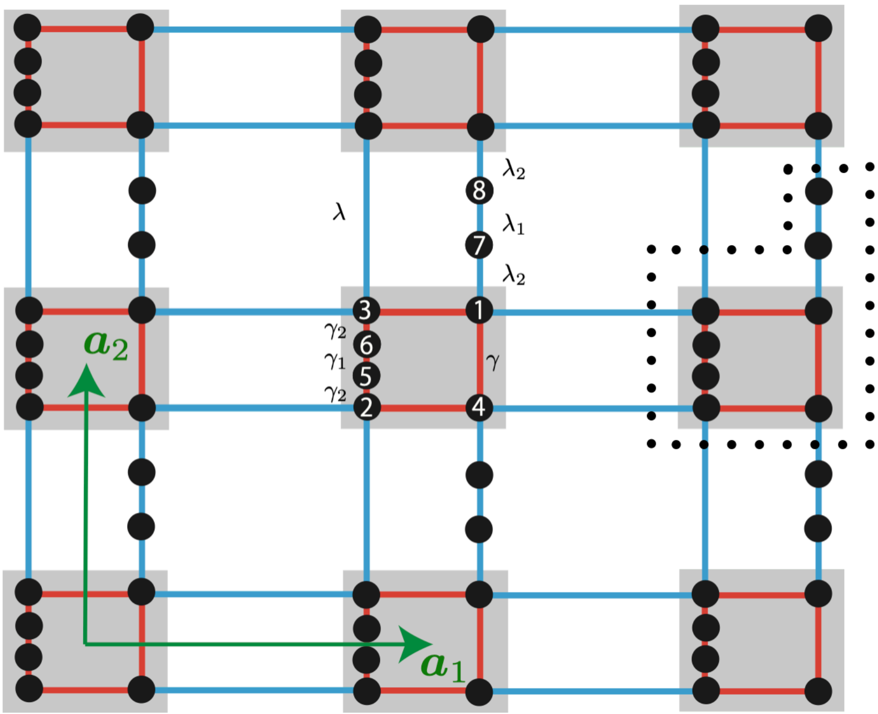

Figure 5.2: BBH model based on the extra-site framework. The unit cell consists of eight sites. The intra-square hoppings are denoted by γ, γ', γ'' , while the inter-square hoppings are represented by λ, λ', λ'''. The region enclosed by the gray rectangle represents the unit cell of the original BBH model, while the region enclosed by the black dashed lines corresponds to the unit cell of our model.

5.3 Band structures

We begin by discussing the structure of the bulk energy dispersions. Unlike the original BBH model, our model contains eight sites per unit cell, resulting in eight energy bands. Figure 5.3 shows the energy dispersion for the parameter set $\gamma = 0.8\lambda$, $\gamma' = 100\gamma$ and $\lambda' = 100\lambda$. With this choice of parameters, the low-energy region successfully reproduces the energy dispersions of the original BBH model (in fact, in the plot of Fig. 5.3, the dispersions overlap to the extent that they are visually indistinguishable). This indicates that the chosen parameter regime lies well within the domain where perturbation theory remains valid.

Let us now explore whether the extra-site model we propose exhibits topological properties. Figure 5.3 shows the energy dispersion of this Hamiltonian. In this plot, the parameters are chosen such that the perturbative regime is valid: specifically, $\gamma' = 100\gamma$ and $\lambda' = 100\lambda$. We present energy dispersions for three cases: (a) $\gamma = 1.2\lambda$, (b) $\gamma = \lambda$, (c) $\gamma = 0.8\lambda$, which correspond to the regime where the original BBH model undergoes a topological phase transition. As shown in Figure 5.3, the bandgap closes at $\gamma/\lambda = 1$, and reopens on for $\gamma/\lambda \neq 1$, confirming the reproduction of the topological phase transition.

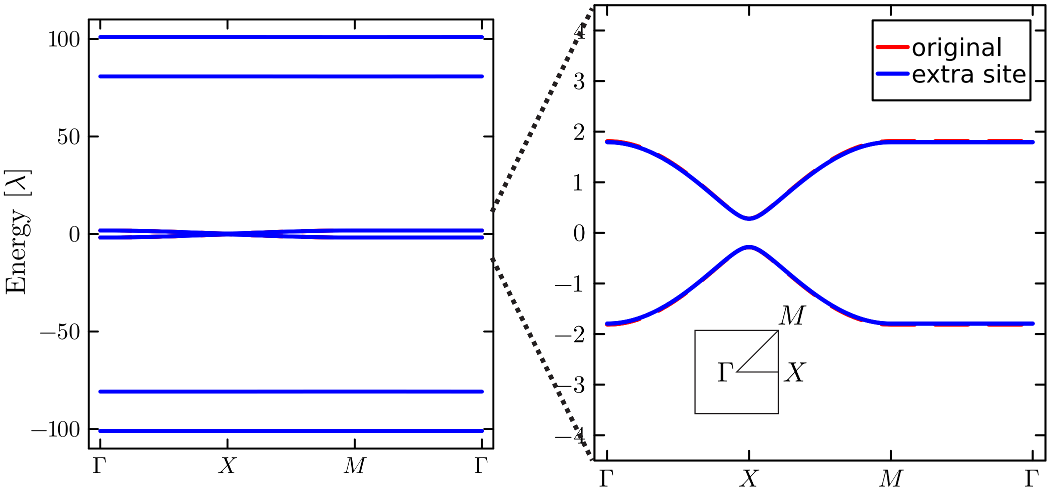

Figure 5.3: Band structure of the extra-site model. Reflecting the presence of eight sites per unit cell, eight bands appear. The parameters are set as $\gamma = 0.8\lambda$, $\gamma' = 100\gamma$ and $\lambda' = 100\lambda$. The red dashed lines indicate the band structure of the original BBH model for comparison.

Interestingly, even when the parameters γ' and λ' are chosen outside the perturbative regime, the closure of the bandgap at γ/λ remains consistent (see FIG. 5.5, 5.6, 5.7). For instance, as demonstrated in Figure 5.7, we computed the energy dispersion for

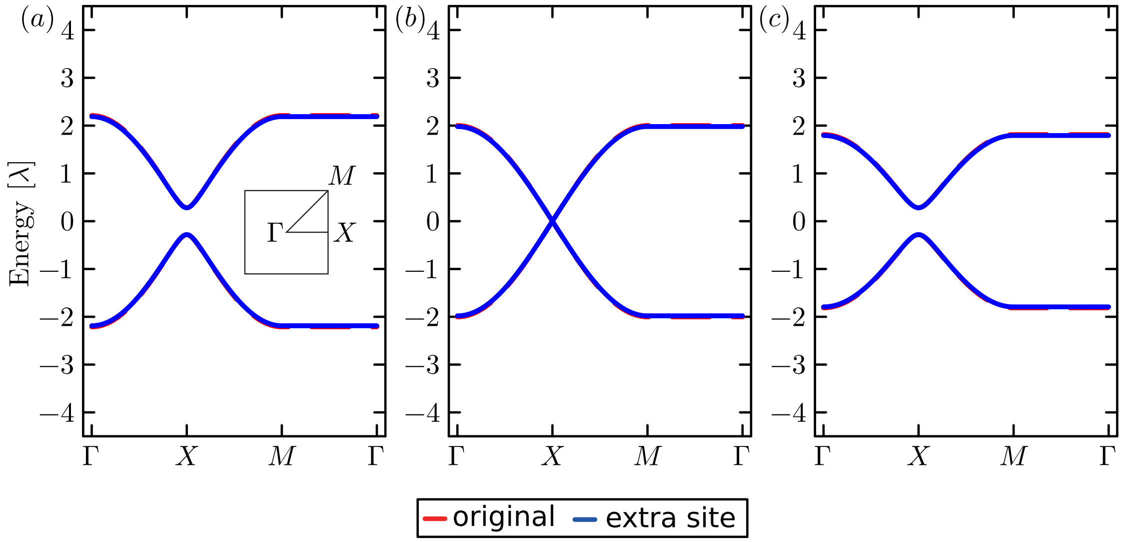

Figure 5.4: Topological phase transition of the extra-site model. The parameters are set as $\gamma' = 100\gamma$ and $\lambda' = 100\lambda$. The red dashed lines indicate the band structure of the original BBH model for comparison. (a) $\gamma = 1.2\lambda$. (b) $\gamma = \lambda$. (c) $\gamma = 0.8\lambda$.

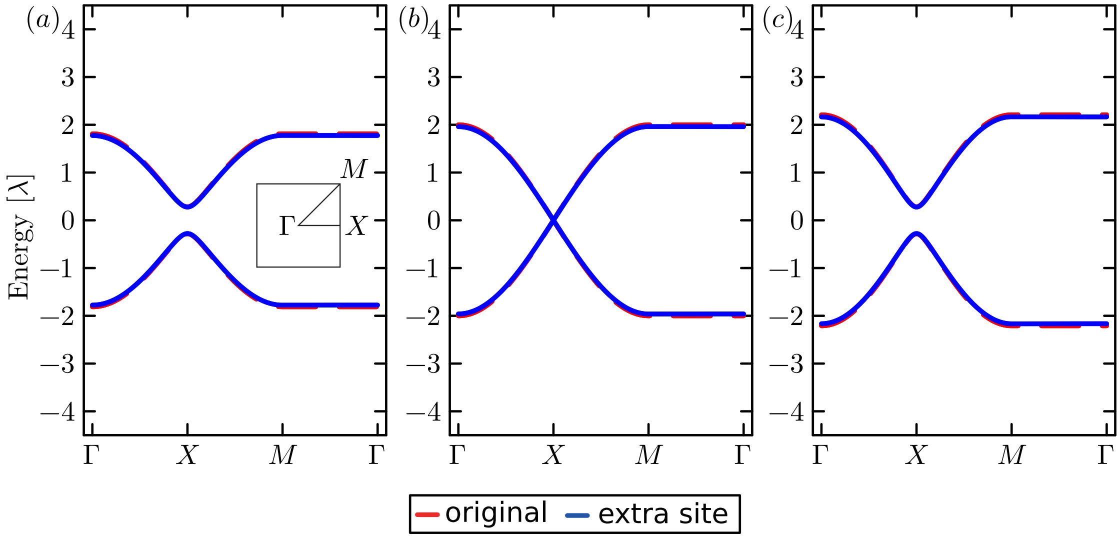

Figure 5.5: Topological phase transition of the extra-site model. The parameters are set as $\gamma' = 50\gamma$ and $\lambda' = 50\lambda$. The red dashed lines indicate the band structure of the original BBH model for comparison. (a) $\gamma = 1.2\lambda$. (b) $\gamma = \lambda$. (c) $\gamma = 0.8\lambda$.

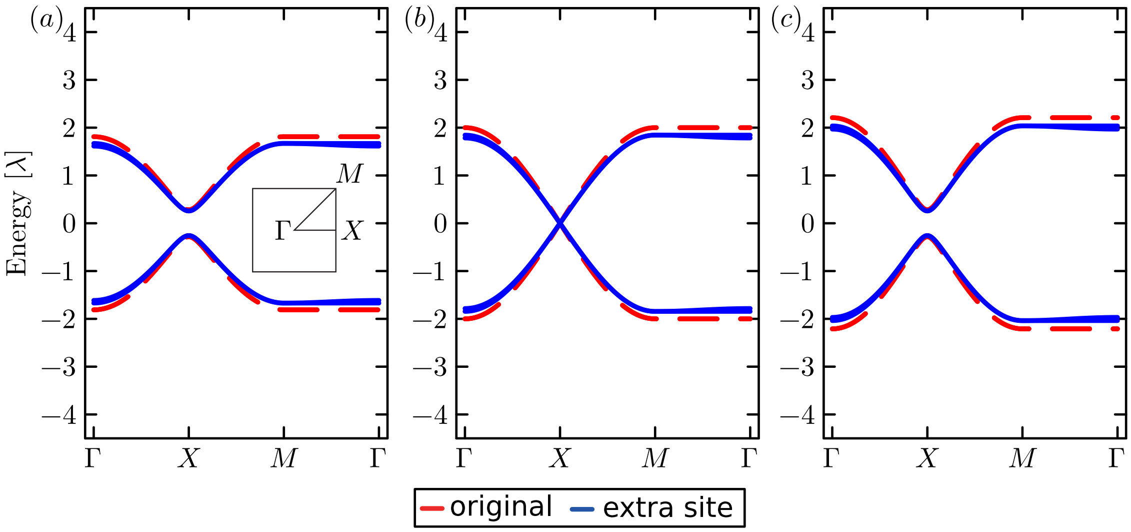

Figure 5.6: Topological phase transition of the extra-site model. The parameters are set as $\gamma' = 10\gamma$ and $\lambda' = 10\lambda$. The red dashed lines indicate the band structure of the original BBH model for comparison. (a) $\gamma = 1.2\lambda$. (b) $\gamma = \lambda$. (c) $\gamma = 0.8\lambda$.

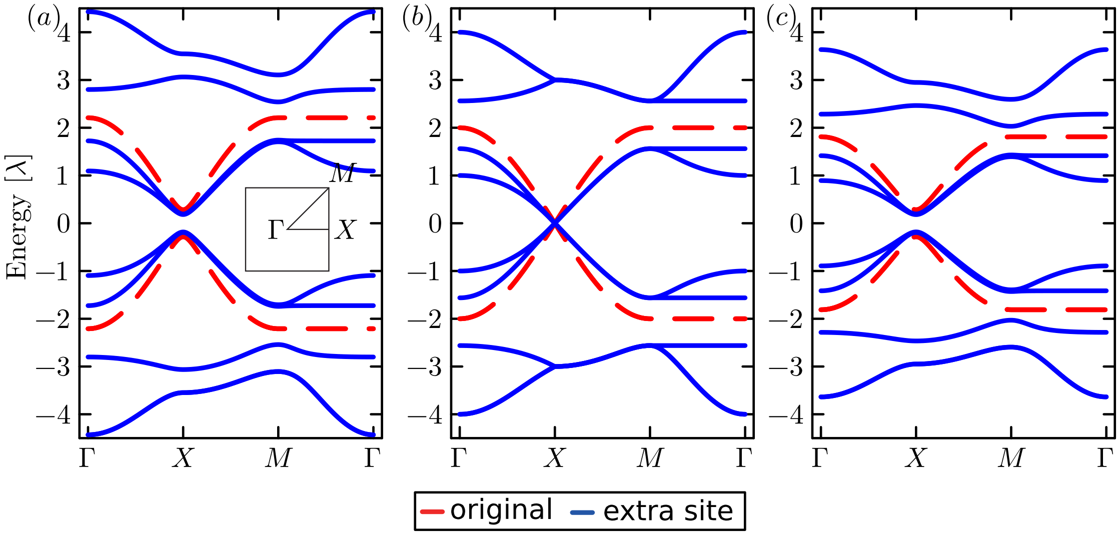

Figure 5.7: Topological phase transition of the extra-site model. The parameters are set as $\gamma' = 2\gamma$ and $\lambda' = 2\lambda$. The red dashed lines indicate the band structure of the original BBH model for comparison. (a) $\gamma = 1.2\lambda$. (b) $\gamma = \lambda$. (c) $\gamma = 0.8\lambda$.

$\gamma' = 2\gamma$ and $\lambda' = 2\lambda$, considering the same three cases. The results again show that the bandgap closes at $\gamma/\lambda = 1$, consistently reproducing the topological phase transition.

To better understand why the bandgap closes at $\gamma/\lambda = 1$, we analyze the system using the Brillouin-Wigner formalism. In the unit cell, the sites can be categorized into α-type sites, originating from the original BBH model, and β-type sites, which are the extra sites we introduced. Using the label of atomic sites in FIG. 5.2, the Hamiltonian can then be written as

$$H_{\mathrm{extra-site}}(\boldsymbol{k}) = \begin{pmatrix} H_{\alpha\alpha}(\boldsymbol{k}) & H_{\alpha\beta}(\boldsymbol{k}) \\ H_{\beta\alpha}(\boldsymbol{k}) & H_{\beta\beta}(\boldsymbol{k}) \end{pmatrix}, \tag{5.7}$$

where

$$\begin{aligned}
H_{\alpha\alpha}(\boldsymbol{k}) &= \begin{pmatrix} 0 & 0 & \gamma + \lambda z_1 & \gamma + \lambda z_2 \\ 0 & 0 & 0 & \gamma + \lambda \overline{z_1} \\ \gamma + \lambda \overline{z_1} & 0 & 0 & 0 \\ \gamma + \lambda \overline{z_2} & \gamma + \lambda z_1 & 0 & 0 \end{pmatrix}, \\
H_{\beta\beta}(\boldsymbol{k}) &= \begin{pmatrix} 0 & \gamma' & 0 & 0 \\ \gamma' & 0 & 0 & 0 \\ 0 & 0 & 0 & \lambda' \\ 0 & 0 & \lambda' & 0 \end{pmatrix}, \\
H_{\alpha\beta}(\boldsymbol{k}) &= \begin{pmatrix} 0 & 0 & 0 & 0 \\ \gamma'' & 0 & 0 & \lambda'' \overline{z_2} \\ 0 & \gamma'' & \lambda'' & 0 \\ 0 & 0 & 0 & 0 \end{pmatrix}, \\
H_{\beta\alpha}(\boldsymbol{k}) &= H_{\alpha\beta}(\boldsymbol{k})^{\dagger}.
\end{aligned} \tag{5.8}$$

Here we define $z_1 := e^{i\boldsymbol{k}\cdot\boldsymbol{a}_1}$ and $z_2 := e^{i\boldsymbol{k}\cdot\boldsymbol{a}_2}$. The unit vectors are $\boldsymbol{a}_1 = a_0(1,0)^T$ and $\boldsymbol{a}_2 = a_0(0,1)^T$ (see FIG. 5.2). We then consider projecting the Hamiltonian onto the subspace spanned by the atomic orbitals belonging to the α-sector. The projected Hamiltonian takes the form

$$H^{\mathrm{eff}}(z_1, z_2, \epsilon) = H_{\alpha\alpha} + H_{\alpha\beta}(\epsilon - H_{\beta\beta})^{-1} H_{\beta\alpha}. \tag{5.9}$$

Here, ϵ represents the energy eigenvalue, and it directly enters the second term of the Hamiltonian due to the projection onto the subspace. We denote this dependency in the arguments of H^{eff}. The eigenenergies are obtained as solutions of

$$H^{\mathrm{eff}}(z_1, z_2, \epsilon) \left|\psi\right\rangle = \epsilon \left|\psi\right\rangle, \tag{5.10}$$

where we denote the eigenfunction as $\left|\psi\right\rangle$. Thus, zero-energy solutions must satisfy

$$H^{\mathrm{eff}}(z_1, z_2, 0) \left|\psi\right\rangle = 0, \tag{5.11}$$

or equivalently,

$$\det\left(H^{\mathrm{eff}}(z_1, z_2, 0)\right) = 0. \tag{5.12}$$

Now, let us consider the case of $\gamma/\lambda = 1$, which we aimed to discuss. Note that the hopping parameters are introduced following the scheme $\gamma' = \sqrt{\gamma\gamma''}$ and $\lambda' = \sqrt{\lambda\lambda''}$. For $\boldsymbol{k} = (\pi, 0)$, we have

$$H^{\mathrm{eff}}(z_1, z_2, 0) = 0_{4\times 4}, \quad \text{i.e.,}\ \det(H^{\mathrm{eff}}(z_1, z_2, 0)) = 0. \tag{5.13}$$

Therefore, it follows that as long as the hopping scheme $\gamma' = \sqrt{\gamma\gamma''}$ and $\lambda' = \sqrt{\lambda\lambda''}$ is adopted, the bandgap generally closes at $\gamma/\lambda = 1$ for $\boldsymbol{k} = (\pi, 0)$, even in parameter regimes where perturbation theory breaks down. This indicates that the phase transition universally occurs in our extra-site model without parameter dependence.

5.4 Corner states and electron density

Next, we discuss the emergence of corner states. By imposing open boundary conditions along both the x- and y-axes, we calculated the energy eigenvalues and eigenstates. Since the unit cell is chosen as shown in FIG. 5.2, the system with open boundary conditions exhibits a structure with dangling sites at the edges, as illustrated in FIG. 5.9(a). Figure 5.8 indicates that, even in our extra-site model, zero-energy states localized at the corners appear within the bandgap when $|\gamma/\lambda| < 1$. We note that these corner states persist even in parameter regimes where perturbation theory breaks down, such as $\gamma' = 2\gamma$ and $\lambda' = 2\lambda$, with zero-energy eigenstates emerging within the bandgap.

A distinguishing feature of our model compared to the original BBH model is the electron density profile. In the parameter regime where perturbation theory is valid (see FIG. 5.9), the electron density is well-localized at the corners, accurately reproducing the behavior of the topological quadrupole phase. However, in parameter regimes where perturbation theory fails (see FIG. 5.10, 5.11, 5.12), the electron density exhibits "leakage" from the corners into the bulk. This behavior is consistent with the absence of mirror symmetry along M_x in this system, which prevents a $\mathbb{Z}_2 \times \mathbb{Z}_2$ classification.

Thus, while the topological quadrupole phase picture breaks down in certain parameter regimes, the occurrence of band inversion and the emergence of zero-energy eigenstates remain robust across all parameter regimes. This robustness suggests that such features can be relatively easily realized in metamaterial setups, such as photonic crystals.

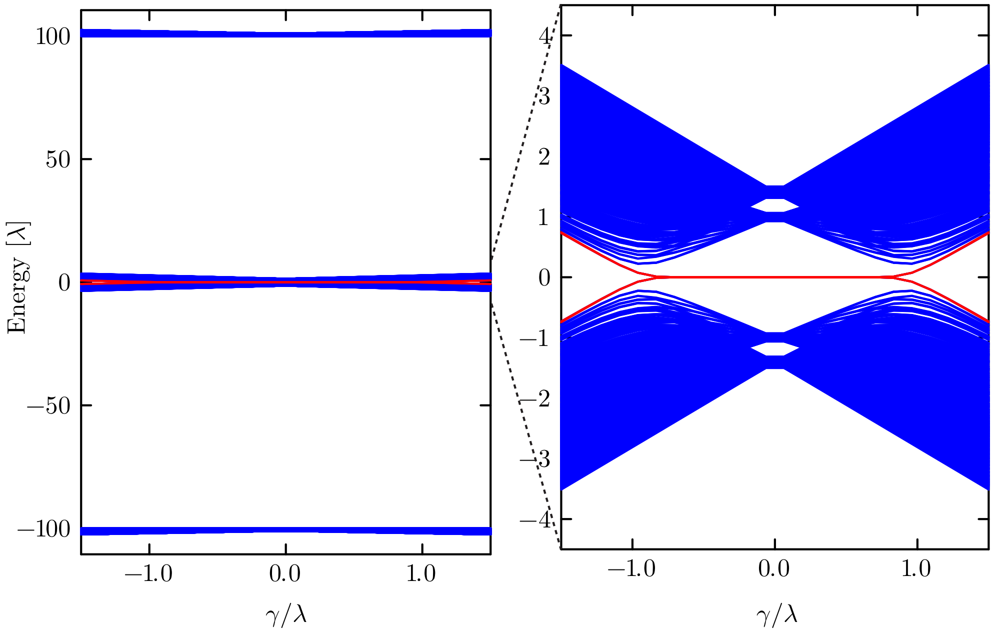

Figure 5.8: The energy spectrum of the BBH model with open boundaries, plotted as a function of γ/λ. The parameters are set as $\gamma' = 100\gamma$ and $\lambda' = 100\lambda$. The calculation is performed for a 20×20 unit cell system.

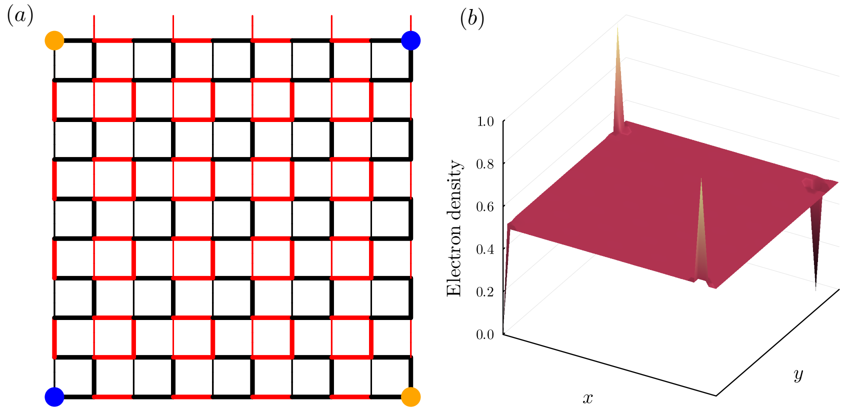

Figure 5.9: The spatial distribution of the electron density at $\gamma = 10^{-3}\lambda$. The parameters are set as $\gamma' = 100\gamma$ and $\lambda' = 100\lambda$. The calculation is performed for a 5×5 unit cell system. (a) A 2D plot of the electron density. Bonds containing extra-sites are represented by thin lines. The circle size corresponds to the magnitude of the electron density, with orange circles indicating positive values and blue circles indicating negative values. (b) The corresponding 3D plot of the electron density.

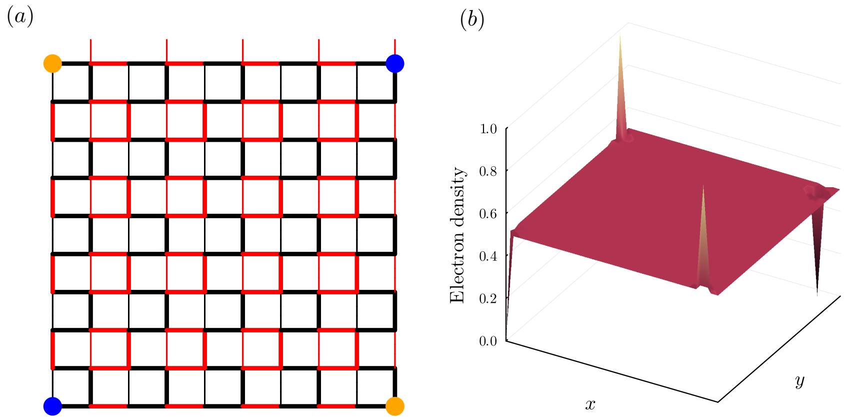

Figure 5.10: The spatial distribution of the electron density at $\gamma = 10^{-3}\lambda$. The parameters are set as $\gamma' = 50\gamma$ and $\lambda' = 50\lambda$. The calculation is performed for a 5×5 unit cell system. (a) A 2D plot of the electron density. Bonds containing extra-sites are represented by thin lines. The circle size corresponds to the magnitude of the electron density, with orange circles indicating positive values and blue circles indicating negative values. (b) The corresponding 3D plot of the electron density.

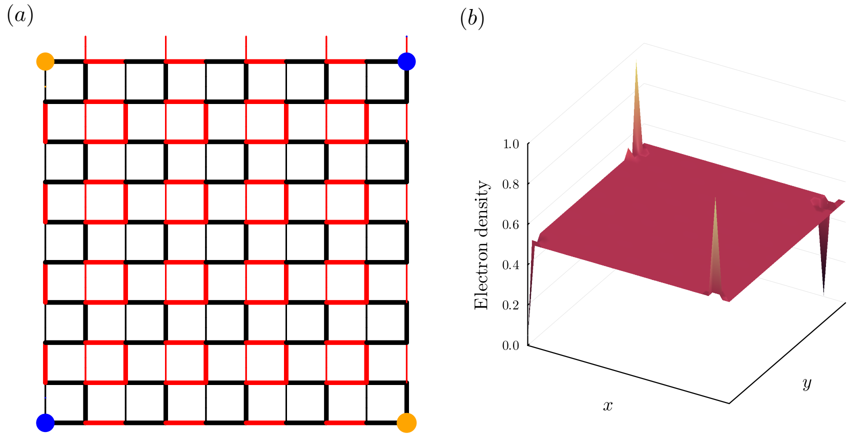

Figure 5.11: The spatial distribution of the electron density at $\gamma = 10^{-3}\lambda$. The parameters are set as $\gamma' = 10\gamma$ and $\lambda' = 10\lambda$. The calculation is performed for a 5×5 unit cell system. (a) A 2D plot of the electron density. Bonds containing extra-sites are represented by thin lines. The circle size corresponds to the magnitude of the electron density, with orange circles indicating positive values and blue circles indicating negative values. (b) The corresponding 3D plot of the electron density.

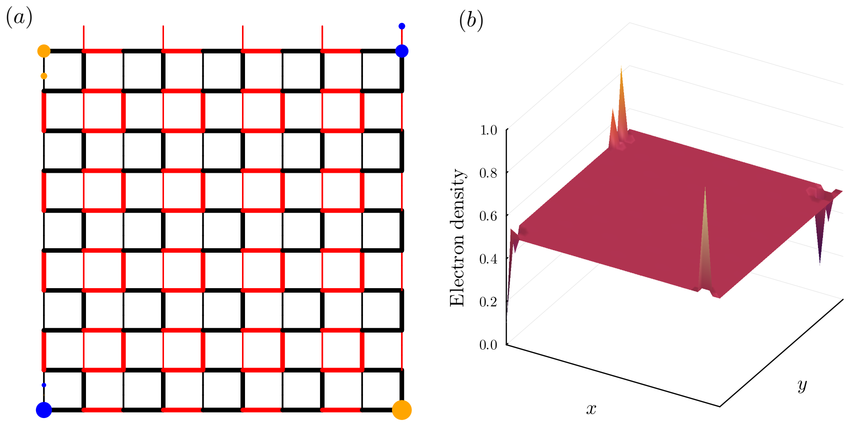

Figure 5.12: The spatial distribution of the electron density at $\gamma = 10^{-3}\lambda$. The parameters are set as $\gamma' = 2\gamma$ and $\lambda' = 2\lambda$. The calculation is performed for a 5×5 unit cell system. (a) A 2D plot of the electron density. Bonds containing extra-sites are represented by thin lines. The circle size corresponds to the magnitude of the electron density, with orange circles indicating positive values and blue circles indicating negative values. (b) The corresponding 3D plot of the electron density.

5.5 Wannier bands

Finally, we characterize the Wannier band structure of this system. As discussed in the previous sections, the system lacks invariance under mirror symmetry M_x. However, it retains invariance under mirror symmetry M_y. As a result, a constraint still applies to the hybrid Wannier centers:

$$\nu_x^+(k_y) = -\nu_x^+(k_y). \tag{5.14}$$

This implies that the Wannier bands must consist of sectors where (i) positive and negative values appear in pairs, denoted by $\nu_\pm$, or (ii) the values remain zero, denoted by $\nu_\emptyset$. Indeed, as shown in Figure 5.5, the Wannier band structures reveal both $\nu_\pm$ and $\nu_\emptyset$ sectors. We note that the sector $\nu_\emptyset$ originates from the additional energy bands associated with the extra sites introduced in our model, and not from the bands near the zero-energy region that are relevant to the topological phase transition. Therefore, the topological features near zero energy are still captured by $\nu_\pm$, and, by focusing on the Wannier band structure $\nu_\pm$ originating from the bands near the zero-energy region, we find that the gapped Wannier band structure is preserved even in the presence of the extra sites in our model.

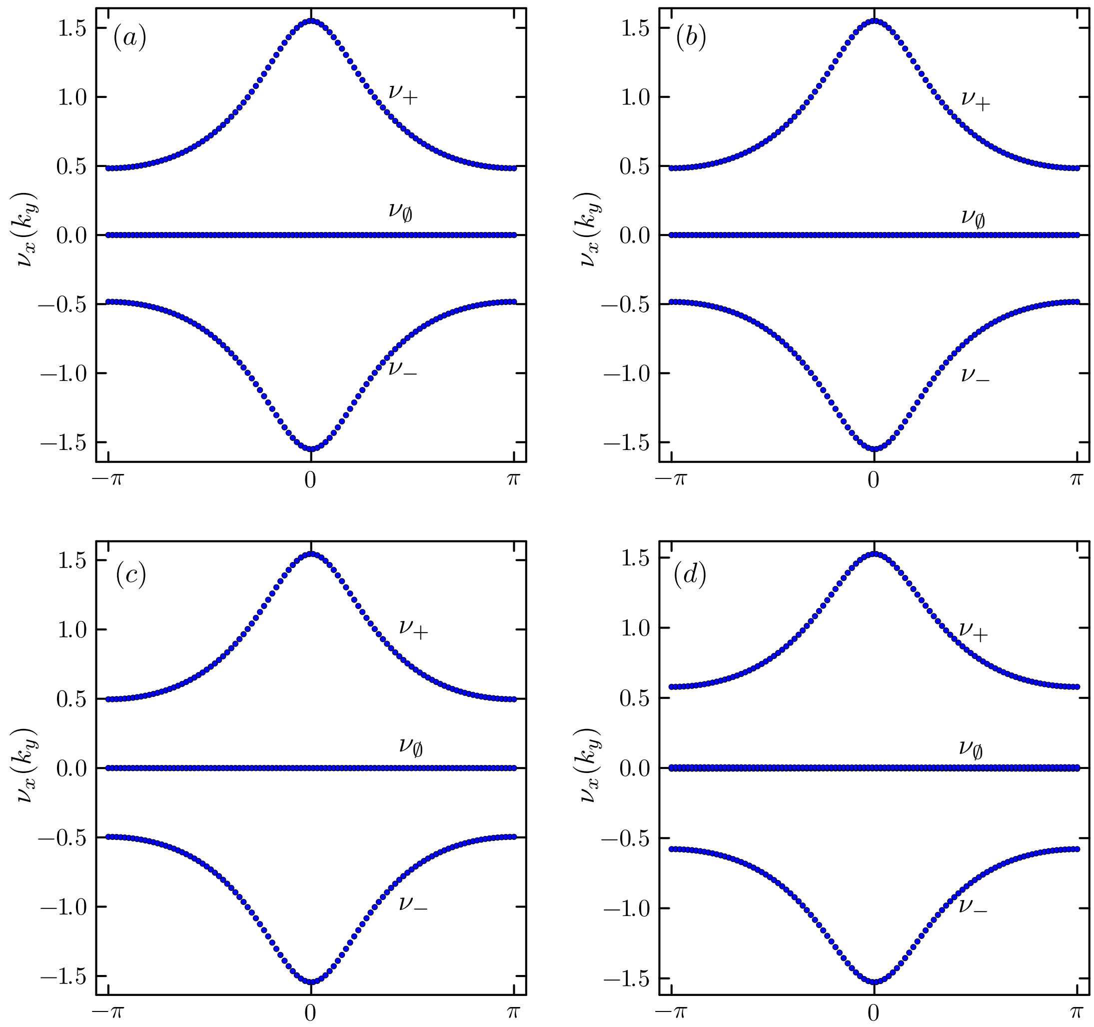

Figure 5.13: Plots of the Wannier bands for the extra-site model. (a)$\gamma' = 100\gamma$ and $\lambda' = 100\lambda$. (b)$\gamma' = 50\gamma$ and $\lambda' = 50\lambda$. (c) $\gamma' = 10\gamma$ and $\lambda' = 10\lambda$. (d) $\gamma' = 2\gamma$ and $\lambda' = 2\lambda$.

5.6 Short summary and future perspectives

We adopt the extra-site model, where sign inversion is implemented by introducing additional sites, and study its properties as a higher-order topological insulator using both analytical and numerical methods. First, we numerically compute the bulk energy dispersion and demonstrate the occurrence of band inversion, which contributes to the band topology. We also perform numerical calculations of the Wannier band structure, showing that a gap opens in the Wannier bands even in the extra-site model. Furthermore, by conducting numerical simulations for a finite system with open boundary conditions, we confirm the emergence of corner states, a hallmark feature of higher-order topological insulators. We have also demonstrated that, unlike the original BBH model, the absence of mirror symmetry in our model leads to leakage of the electronic density from the corners in the regime where perturbation theory breaks down.

While this study focused on the properties of the BBH model in the presence of a uniform π-flux through each plaquette, it is natural to expect that the formulation developed here will also be useful for analyzing models with local π-flux insertions. As mentioned in Sec. 5.1, such local flux insertions have been shown to host in-gap states that can serve as probes of the bulk topology. Therefore, extending our analysis to systems where a π-flux is inserted as a defect would be a promising future direction. Moreover, from an experimental perspective, especially in the context of topological metamaterials, our scheme provides a systematic approach to implementing sign flips in hopping amplitudes using only real parameters.

Chapter 6

Conclusion

In this work, we have explored the rich landscape of topological crystalline insulators, emphasizing the role of crystalline symmetries in defining novel topological phases. Through the study of Wilson loops, winding numbers, and other topological invariants, we have provided a detailed characterization of various models that exhibit nontrivial topology. Our works are summarized as follows:

Chiral honeycomb lattice model

We propose a novel tight-binding model to describe chiral systems and study its properties using both analytical and numerical methods. First, we numerically compute the bulk energy dispersion and demonstrate that band inversion occurs as the model parameter, i.e., the hopping amplitude, is varied. By performing a perturbative expansion of the Hamiltonian up to the first order in momentum, we show that the band inversion can be understood as a sign change in the mass term of the Dirac equation. We also discuss the topological nontriviality of our system using the framework of the Wilson loop. In addition, we consider a system composed of two regions with different topological properties and numerically demonstrate the emergence of topological states at their boundaries. Furthermore, for a system with a boundary, we analytically confirm the presence of topological states using an effective model based on the Dirac equation.

Furthermore, we numerically compute the energy flow by mapping our system to a classical system, and have discovered a novel asymmetric edge current induced without any phase tuning at input terminals. These consideration could be a building block in exploring chiral topological materials.

Extra-site model for HOTIs

We adopt the extra-site model, where sign inversion is implemented by introducing additional sites, and study its properties as a higher-order topological insulator using both analytical and numerical methods. First, we numerically compute the bulk energy dispersion and demonstrate the occurrence of band inversion, which contributes to the band topology. We also perform numerical calculations of the Wannier band structure, showing that a gap opens in the Wannier bands even in the extra-site model. Furthermore, by conducting numerical simulations for a finite system with open boundary conditions, we confirm the emergence of corner states, a hallmark feature of higher-order topological insulators.

Acknowledgement

I would like to express my deepest gratitude to my supervisor, Professor Jun-ichi Fukuda, for granting me the freedom to pursue my research in an open and intellectually stimulating environment. His guidance and encouragement have been invaluable throughout my doctoral studies.

I am particularly indebted to Dr. Toshikaze Kariyado, my co-author and collaborator, whose technical expertise and insightful discussions have been fundamental to the progress of my research. It is without a doubt that this work would not have come to fruition were it not for his steadfast support and invaluable contributions.

I am also grateful to Professor Xiao Hu and his laboratory members, as well as Professor Kentaro Nomura, for their invaluable feedback and constructive discussions. Their insightful comments have significantly contributed to the refinement of my research.

I would also like to thank Dr. Hiroaki Ishizuka, with whom I had the privilege of working during the latter part of my doctoral studies. While our research could not be included in this thesis, our collaboration was profoundly meaningful, and I look forward to continuing our work with the aim of publishing it as an academic paper.

Furthermore, I wish to extend my appreciation to my friends, whose encouragement has been instrumental in sustaining my motivation throughout the course of my doctoral studies. In particular, my fellow doctoral students, my high school friends, and those whom I encountered in less conventional circumstances, non-academic contexts have provided unwavering moral support, for which I am profoundly thankful.

I am also deeply grateful to my family for their unconditional support and encouragement throughout my academic journey. Their patience, understanding, and belief in me have been a constant source of strength, allowing me to pursue my research with confidence and determination.

Finally, I extend my heartfelt gratitude to all those who have supported me, directly or indirectly, throughout this journey. Their generosity, encouragement, and belief in my abilities have been essential in bringing this thesis to completion.

Appendix A

Derivation of the effective Hamiltonian

To derive the effective Hamiltonian Eq. (3.5), we focus on the eigenstates at the Γ point, i.e. $\boldsymbol{k}_\Gamma = \boldsymbol{0}$. The following derivation is in parallel with the supplementary materials of the previous study [26], but any terms with t_2 and t_3 are new. The eigenstates of $H(\boldsymbol{k} = \boldsymbol{k}_\Gamma)$ are given by

$$\begin{aligned}
|f_{y(3x^2-y^2)}\rangle &= (-1,-1,-1,1,1,1)^T/\sqrt{6}, \\
|p_x\rangle &= (0,-1,1,0,1,-1)^T/2, \\
|p_y\rangle &= (2,-1,-1,-2,1,1)^T/2\sqrt{3}, \\
|d_{x^2-y^2}\rangle &= (-2,1,1,-2,1,1)^T/2\sqrt{3}, \\
|d_{xy}\rangle &= (0,1,-1,0,1,-1)^T/2, \\
|s\rangle &= (1,1,1,1,1,1)^T/\sqrt{6}. \qquad \text{(A.1)}
\end{aligned}$$

We use the conventional notation of s, p, d and f atomic orbitals. The corresponding eigenenergies are $E_{f_{y(3x^2-y^2)}} = -2t_0 - t_1 + 2t_2 + 2t_3$, $E_{p_x,p_y} = t_0 - t_1 - t_2 - t_3$, $E_{d_{x^2-y^2},d_{xy}} = t_1 - t_0 - t_2 - t_3$ and $E_s = 2t_0 + t_1 + 2t_2 + 2t_3$, respectively. In the following, we consider the case $E_{f_{y(3x^2-y^2)}} < E_{p_x,p_y,d_{x^2-y^2},d_{xy}} < E_s$. Based on these eigenstates, one can construct a low-energy effective Hamiltonian around the Γ point. Since we focus on the neighborhood of the Γ point where the bands are dominated by p and d states, it is sufficient to use $\{|p_x\rangle, |p_y\rangle, |d_{x^2-y^2}\rangle, |d_{xy}\rangle\}$ as the basis in calculating the effective Hamiltonian. By using these four eigenstates, we define the following pseudo-spin modes:

$$|p_\pm\rangle = \frac{1}{\sqrt{2}}(|p_x\rangle \pm i\,|p_y\rangle), \qquad \text{(A.2)}$$

$$|d_\pm\rangle = \frac{1}{\sqrt{2}}(|d_{x^2-y^2}\rangle \pm i\,|d_{xy}\rangle). \qquad \text{(A.3)}$$

In order to consider the effective Hamiltonian, it is convenient to introduce the following basis:

$$|u_\pm\rangle = \frac{1}{\sqrt{2}}(\mp i\,|p_\pm\rangle - |d_\mp\rangle), \tag{A.4}$$

$$|l_\pm\rangle = \frac{1}{\sqrt{2}}(i\,|p_\pm\rangle \mp |d_\mp\rangle). \tag{A.5}$$

Here, the explicit expression of $\{|u_-\rangle, |u_+\rangle, |l_-\rangle, |l_+\rangle\}$ is

$$|u_\pm\rangle = \begin{pmatrix} |\pm\rangle \\ 0 \end{pmatrix}, |l_\pm\rangle = \begin{pmatrix} 0 \\ \pm\,|\pm\rangle \end{pmatrix}, \tag{A.6}$$

where

$$|\pm\rangle = \begin{pmatrix} 1 \\ \omega_\pm \\ \omega_\mp \end{pmatrix}, \omega_\pm = -\frac{1}{2} \pm \frac{\sqrt{3}}{2} i. \tag{A.7}$$

Now, let us first calculate the low-energy effective Hamiltonian by using $\{|u_-\rangle, |u_+\rangle, |l_-\rangle, |l_+\rangle\}$. Indeed, if we expand the Hamiltonian in the basis, the effective Hamiltonian becomes

$$\mathcal{H}^{(\mathrm{eff})}(k_x,k_y) = \begin{pmatrix} \langle -|\,F\,|-\rangle & \langle -|\,F\,|+\rangle & -\langle -|\,D\,|-\rangle & \langle -|\,D\,|+\rangle \\ \langle +|\,F\,|-\rangle & \langle +|\,F\,|+\rangle & -\langle +|\,D\,|-\rangle & \langle +|\,D\,|+\rangle \\ -\langle -|\,D^\dagger\,|-\rangle & -\langle -|\,D^\dagger\,|+\rangle & \langle -|\,F^T\,|-\rangle & \langle -|\,F^T\,|+\rangle \\ \langle +|\,D^\dagger\,|-\rangle & \langle +|\,D^\dagger\,|+\rangle & \langle +|\,F^T\,|-\rangle & \langle +|\,F^T\,|+\rangle \end{pmatrix}. \tag{A.8}$$

Then, we perform the Taylor expansion up to the first order of the wavevectors. The effective Hamiltonian is approximated as

$$\mathcal{H}^{(\mathrm{eff})}(k_x,k_y) \simeq -(t_2+t_3) I \otimes I + (t_0 - t_1)\sigma_x \otimes \sigma_z + \frac{t_1|\boldsymbol{a}_1|}{2}\sigma_x \otimes (\boldsymbol{k}\cdot\boldsymbol{\sigma}), \tag{A.9}$$

where I is the identity matrix and $\sigma_i (i = x, y, z)$ is the Pauli matrices. We denote the Kronecker product as $\otimes$. It is shown that Eq.(A.9) can be written as the Dirac Hamiltonian by introducing the following new basis:

$$|1\rangle = i\,|p_-\rangle = \frac{|u_-\rangle + |l_-\rangle}{\sqrt{2}}, \tag{A.10}$$

$$|2\rangle = -\,|d_-\rangle = \frac{|u_+\rangle + |l_+\rangle}{\sqrt{2}}, \tag{A.11}$$

$$|3\rangle = -i\,|p_+\rangle = \frac{|u_+\rangle - |l_+\rangle}{\sqrt{2}}, \tag{A.12}$$

$$|4\rangle = -\,|d_+\rangle = \frac{|u_-\rangle - |l_-\rangle}{\sqrt{2}}. \tag{A.13}$$

Using these new bases, the effective Hamiltonian is rewritten as

$$\mathcal{H}^{(\mathrm{eff})}(k_x, k_y) \simeq \begin{pmatrix} H_+(k_x, k_y) & 0 \\ 0 & H_-(k_x, k_y) \end{pmatrix}, \tag{A.14}$$

where

$$H_\pm(k_x, k_y) = -(t_2 + t_3)I + (t_0 - t_1)\sigma_z + \frac{t_1|\boldsymbol{a}_1|}{2}(\pm k_x\sigma_x + k_y\sigma_y). \tag{A.15}$$

Thus, we obtain the Dirac Hamiltonian Eq.(A.15) with the constant energy shift $-(t_2 + t_3)$.

Bibliography

[1] K. v. Klitzing, G. Dorda, and M. Pepper. New method for high-accuracy determination of the fine-structure constant based on quantized Hall resistance. *Phys. Rev. Lett.*, 45:494–497, Aug 1980.

[2] R. E. Prange and S. M. Girvin. *The Quantum Hall Effect.* Springer, 1987.

[3] M. Nakahara. *Geometry, Topology and Physics.* Hilger, 1990.

[4] D. J. Thouless, M. Kohmoto, M. P. Nightingale, and M. den Nijs. Quantized Hall conductance in a two-dimensional periodic potential. *Phys. Rev. Lett.*, 49:405–408, Aug 1982.

[5] Mahito Kohmoto. Topological invariant and the quantization of the hall conductance. *Annals of Physics*, 160(2):343–354, 1985.

[6] M. V. Berry. Quantal phase factors accompanying adiabatic changes. *Proceedings of the Royal Society of London. Series A, Mathematical and Physical Sciences*, 392(1802):45–57, 1984.

[7] Yasuhiro Hatsugai. Chern number and edge states in the integer quantum hall effect. *Phys. Rev. Lett.*, 71:3697–3700, Nov 1993.

[8] Yasuhiro Hatsugai. Edge states in the integer quantum hall effect and the riemann surface of the bloch function. *Phys. Rev. B*, 48:11851–11862, Oct 1993.

[9] F. D. M. Haldane. Model for a quantum Hall effect without Landau levels: Condensed-matter realization of the "parity anomaly". *Phys. Rev. Lett.*, 61:2015–2018, Oct 1988.

[10] C. L. Kane and E. J. Mele. Z_2 topological order and the quantum Spin hall effect. *Phys. Rev. Lett.*, 95:146802, Sep 2005.

[11] C. L. Kane and E. J. Mele. Quantum spin Hall effect in graphene. *Phys. Rev. Lett.*, 95:226801, Nov 2005.

[12] B. Andrei Bernevig, Taylor L. Hughes, and Shou-Cheng Zhang. Quantum spin Hall effect and topological phase transition in HgTe quantum wells. *Science*, 314(5806):1757–1761, 2006.

[13] Markus König, Steffen Wiedmann, Christoph Brüne, Andreas Roth, Hartmut Buhmann, Laurens W Molenkamp, Xiao-Liang Qi, and Shou-Cheng Zhang. Quantum spin hall insulator state in hgte quantum wells. *Science*, 318(5851):766–770, Nov 2007.

[14] Liang Fu, C. L. Kane, and E. J. Mele. Topological insulators in three dimensions. *Phys. Rev. Lett.*, 98:106803, Mar 2007.

[15] Liang Fu and C. L. Kane. Topological insulators with inversion symmetry. *Phys. Rev. B*, 76:045302, Jul 2007.

[16] Haijun Zhang, Chao-Xing Liu, Xiao-Liang Qi, Xi Dai, Zhong Fang, and Shou-Cheng Zhang. Topological insulators in $\mathrm{Bi_2Se_3}$, $\mathrm{Bi_2Te_3}$ and $\mathrm{Sb_2Te_3}$ with a single Dirac cone on the surface. *Nature Physics*, 5(6):438–442, June 2009.

[17] D. Hsieh, Y. Xia, D. Qian, L. Wray, F. Meier, J. H. Dil, J. Osterwalder, L. Patthey, A. V. Fedorov, H. Lin, A. Bansil, D. Grauer, Y. S. Hor, R. J. Cava, and M. Z. Hasan. Observation of time-reversal-protected single-dirac-cone topological-insulator states in $\mathrm{bi_2te_3}$ and $\mathrm{sb_2te_3}$. *Phys. Rev. Lett.*, 103:146401, Sep 2009.

[18] Y L Chen, J G Analytis, J-H Chu, Z K Liu, S-K Mo, X L Qi, H J Zhang, D H Lu, X Dai, Z Fang, S C Zhang, I R Fisher, Z Hussain, and Z-X Shen. Experimental realization of a three-dimensional topological insulator, bi2te3. *Science*, 325(5937):178–181, Jul 2009.

[19] Y. Xia, D. Qian, D. Hsieh, L. Wray, A. Pal, H. Lin, A. Bansil, D. Grauer, Y. S. Hor, R. J. Cava, and M. Z. Hasan. Observation of a large-gap topological-insulator class with a single dirac cone on the surface. *Nature Physics*, 5(6):398–402, 2009.

[20] W. P. Su, J. R. Schrieffer, and A. J. Heeger. Solitons in polyacetylene. *Phys. Rev. Lett.*, 42:1698–1701, Jun 1979.

[21] Liang Fu. Topological crystalline insulators. *Phys. Rev. Lett.*, 106:106802, Mar 2011.

[22] Timothy H. Hsieh, Hsin Lin, Junwei Liu, Wenhui Duan, Arun Bansil, and Liang Fu. Topological crystalline insulators in the snte material class. *Nature Communications*, 3(1):982, 2012.

[23] Y. Tanaka, Zhi Ren, T. Sato, K. Nakayama, S. Souma, T. Takahashi, Kouji Segawa, and Yoichi Ando. Experimental realization of a topological crystalline insulator in snte. *Nature Physics*, 8(11):800–803, 2012.

[24] Long-Hua Wu and Xiao Hu. Topological properties of electrons in honeycomb lattice with detuned hopping energy. *Scientific Reports*, 6(1):24347, 2016.

[25] Tetsuro Inui, Yukito Tanabe, and Yositaka Onodera. *Group Theory and Its Applications in Physics*. Shokabo, 1996.

[26] Toshikaze Kariyado and Robert-Jan Slager. π-fluxes, semimetals, and flat bands in artificial materials. *Phys. Rev. Res.*, 1:032027, Nov 2019.

[27] Toshikaze Kariyado and Xiao Hu. Topological states characterized by mirror winding numbers in graphene with bond modulation. *Scientific Reports*, 7(1):16515, 2017.

[28] Long-Hua Wu and Xiao Hu. Scheme for achieving a topological photonic crystal by using dielectric material. *Phys. Rev. Lett.*, 114:223901, Jun 2015.

[29] Wladimir A. Benalcazar, B. Andrei Bernevig, and Taylor L. Hughes. Quantized electric multipole insulators. *Science*, 357(6346):61–66, 2017.

[30] Frank Schindler, Ashley M. Cook, Maia G. Vergniory, Zhijun Wang, Stuart S. P. Parkin, B. Andrei Bernevig, and Titus Neupert. Higher-order topological insulators. *Science Advances*, 4(6):eaat0346, 2018.

[31] Yang Peng, Yimu Bao, and Felix von Oppen. Boundary green functions of topological insulators and superconductors. *Phys. Rev. B*, 95:235143, Jun 2017.

[32] Josias Langbehn, Yang Peng, Luka Trifunovic, Felix von Oppen, and Piet W. Brouwer. Reflection-symmetric second-order topological insulators and superconductors. *Phys. Rev. Lett.*, 119:246401, Dec 2017.

[33] Zhida Song, Zhong Fang, and Chen Fang. $(d-2)$-dimensional edge states of rotation symmetry protected topological states. *Phys. Rev. Lett.*, 119:246402, Dec 2017.

[34] Wladimir A. Benalcazar, B. Andrei Bernevig, and Taylor L. Hughes. Electric multipole moments, topological multipole moment pumping, and chiral hinge states in crystalline insulators. *Phys. Rev. B*, 96:245115, Dec 2017.

[35] Mao Lin and Taylor L. Hughes. Topological quadrupolar semimetals. *Phys. Rev. B*, 98:241103, Dec 2018.

[36] Frank Schindler, Zhijun Wang, Maia G. Vergniory, Ashley M. Cook, Anil Murani, Shamashis Sengupta, Alik Yu. Kasumov, Richard Deblock, Sangjun Jeon, Ilya Drozdov, Hélène Bouchiat, Sophie Guéron, Ali Yazdani, B. Andrei Bernevig, and Titus Neupert. Higher-order topology in bismuth. *Nature Physics*, 14(9):918–924, 2018.

[37] Motohiko Ezawa. Higher-order topological insulators and semimetals on the breathing kagome and pyrochlore lattices. *Phys. Rev. Lett.*, 120:026801, Jan 2018.

[38] Motohiko Ezawa. Minimal models for wannier-type higher-order topological insulators and phosphorene. *Phys. Rev. B*, 98:045125, Jul 2018.

[39] Motohiko Ezawa. Magnetic second-order topological insulators and semimetals. *Phys. Rev. B*, 97:155305, Apr 2018.

[40] Motohiko Ezawa. Topological switch between second-order topological insulators and topological crystalline insulators. *Phys. Rev. Lett.*, 121:116801, Sep 2018.

[41] Tomoki Ozawa, Hannah M. Price, Alberto Amo, Nathan Goldman, Mohammad Hafezi, Ling Lu, Mikael C. Rechtsman, David Schuster, Jonathan Simon, Oded Zilberberg, and Iacopo Carusotto. Topological photonics. *Rev. Mod. Phys.*, 91:015006, Mar 2019.

[42] C. J. Pethick and H. Smith. *Bose-Einstein Condensation in Dilute Gases*. Cambridge University Press, 2nd edition, 2008.

[43] Lev Pitaevskii and Sandro Stringari. *Bose-Einstein Condensation and Superfluidity*, volume 164 of *International Series of Monographs on Physics*. Oxford University Press, 2016.

[44] Tomoki Ozawa. Quantum simulation and topological phases in artificial quantum materials. Lecture note, 2022. Lecture on June 9, 2022. Accessed: February 28, 2024.

[45] M. H. Anderson, J. R. Ensher, M. R. Matthews, C. E. Wieman, and E. A. Cornell. Observation of bose-einstein condensation in a dilute atomic vapor. *Science*, 269(5221):198–201, 1995.

[46] B. DeMarco and D. S. Jin. Onset of fermi degeneracy in a trapped atomic gas. *Science*, 285(5434):1703–1706, 1999.

[47] Andrew G. Truscott, Kevin E. Strecker, William I. McAlexander, Guthrie B. Partridge, and Randall G. Hulet. Observation of fermi pressure in a gas of trapped atoms. *Science*, 291(5513):2570–2572, 2001.

[48] G. Modugno, G. Ferrari, G. Roati, R. J. Brecha, A. Simoni, and M. Inguscio. Bose-einstein condensation of potassium atoms by sympathetic cooling. *Science*, 294(5545):1320–1322, 2001.

[49] Rudolf Grimm, Matthias Weidemüller, and Yurii B. Ovchinnikov. Optical dipole traps for neutral atoms. volume 42 of *Advances In Atomic, Molecular, and Optical Physics*, pages 95–170. Academic Press, 2000.

[50] Nicolas Schlosser, Georges Reymond, Igor Protsenko, and Philippe Grangier. Sub-poissonian loading of single atoms in a microscopic dipole trap. *Nature*, 411(6841):1024–1027, 2001.

[51] Markus Greiner, Olaf Mandel, Tilman Esslinger, Theodor W. Hänsch, and Immanuel Bloch. Quantum phase transition from a superfluid to a mott insulator in a gas of ultracold atoms. *Nature*, 415(6867):39–44, 2002.

[52] Immanuel Bloch. Ultracold quantum gases in optical lattices. *Nature Physics*, 1(1):23–30, 2005.

[53] D. Jaksch, C. Bruder, J. I. Cirac, C. W. Gardiner, and P. Zoller. Cold bosonic atoms in optical lattices. *Phys. Rev. Lett.*, 81:3108–3111, Oct 1998.

[54] Steven Chu. Nobel lecture: The manipulation of neutral particles. *Rev. Mod. Phys.*, 70:685–706, Jul 1998.

[55] Dan-Wei Zhang, Yan-Qing Zhu, Y. X. Zhao, Hui Yan, and Shi-Liang Zhu. Topological quantum matter with cold atoms. *Advances in Physics*, 67(4):253–402, 10 2018.

[56] Marcos Atala, Monika Aidelsburger, Julio T. Barreiro, Dmitry Abanin, Takuya Kitagawa, Eugene Demler, and Immanuel Bloch. Direct measurement of the zak phase in topological bloch bands. *Nature Physics*, 9(12):795–800, 2013.

[57] Eric J. Meier, Fangzhao Alex An, and Bryce Gadway. Observation of the topological soliton state in the su–schrieffer–heeger model. *Nature Communications*, 7(1):13986, 2016.

[58] M. Lohse, C. Schweizer, O. Zilberberg, M. Aidelsburger, and I. Bloch. A thouless quantum pump with ultracold bosonic atoms in an optical superlattice. *Nature Physics*, 12(4):350–354, 2016.

[59] Shuta Nakajima, Takafumi Tomita, Shintaro Taie, Tomohiro Ichinose, Hideki Ozawa, Lei Wang, Matthias Troyer, and Yoshiro Takahashi. Topological thouless pumping of ultracold fermions. *Nature Physics*, 12(4):296–300, 2016.

[60] M. Aidelsburger, M. Atala, M. Lohse, J. T. Barreiro, B. Paredes, and I. Bloch. Realization of the hofstadter hamiltonian with ultracold atoms in optical lattices. *Phys. Rev. Lett.*, 111:185301, Oct 2013.

[61] Hirokazu Miyake, Georgios A. Siviloglou, Colin J. Kennedy, William Cody Burton, and Wolfgang Ketterle. Realizing the harper hamiltonian with laser-assisted tunneling in optical lattices. *Phys. Rev. Lett.*, 111:185302, Oct 2013.

[62] Gregor Jotzu, Michael Messer, Rémi Desbuquois, Martin Lebrat, Thomas Uehlinger, Daniel Greif, and Tilman Esslinger. Experimental realization of the topological haldane model with ultracold fermions. *Nature*, 515(7526):237–240, 2014.

[63] N. Goldman, I. Satija, P. Nikolic, A. Bermudez, M. A. Martin-Delgado, M. Lewenstein, and I. B. Spielman. Realistic time-reversal invariant topological insulators with neutral atoms. *Phys. Rev. Lett.*, 105:255302, Dec 2010.

[64] Shi-Liang Zhu, Baigeng Wang, and L.-M. Duan. Simulation and detection of dirac fermions with cold atoms in an optical lattice. *Phys. Rev. Lett.*, 98:260402, Jun 2007.

[65] Brandon M. Anderson, Gediminas Juzeliūnas, Victor M. Galitski, and I. B. Spielman. Synthetic 3d spin-orbit coupling. *Phys. Rev. Lett.*, 108:235301, Jun 2012.

[66] Leticia Tarruell, Daniel Greif, Thomas Uehlinger, Gregor Jotzu, and Tilman Esslinger. Creating, moving and merging dirac points with a fermi gas in a tunable honeycomb lattice. *Nature*, 483(7389):302–305, 2012.

[67] Tena Dubček, Colin J. Kennedy, Ling Lu, Wolfgang Ketterle, Marin Soljačić, and Hrvoje Buljan. Weyl points in three-dimensional optical lattices: Synthetic magnetic monopoles in momentum space. *Phys. Rev. Lett.*, 114:225301, Jun 2015.

[68] Jing-Min Hou and Wei Chen. Weyl semimetals in optical lattices: moving and merging of weyl points, and hidden symmetry at weyl points. *Scientific Reports*, 6(1):33512, 2016.

[69] Takashi Oka and Hideo Aoki. Photovoltaic Hall effect in graphene. *Phys. Rev. B*, 79:081406, Feb 2009.

[70] Takuya Kitagawa, Takashi Oka, Arne Brataas, Liang Fu, and Eugene Demler. Transport properties of nonequilibrium systems under the application of light: Photoinduced quantum Hall insulators without Landau levels. *Phys. Rev. B*, 84:235108, Dec 2011.

[71] N. Goldman and J. Dalibard. Periodically driven quantum systems: Effective hamiltonians and engineered gauge fields. *Phys. Rev. X*, 4:031027, Aug 2014.

[72] Marin Bukov, Luca D'Alessio, and Anatoli Polkovnikov. Universal high-frequency behavior of periodically driven systems: from dynamical stabilization to floquet engineering. *Advances in Physics*, 64(2):139–226, 03 2015.

[73] André Eckardt and Egidijus Anisimovas. High-frequency approximation for periodically driven quantum systems from a floquet-space perspective. *New Journal of Physics*, 17(9):093039, sep 2015.

[74] N. Goldman, J. Dalibard, M. Aidelsburger, and N. R. Cooper. Periodically driven quantum matter: The case of resonant modulations. *Phys. Rev. A*, 91:033632, Mar 2015.

[75] Takahiro Mikami, Sota Kitamura, Kenji Yasuda, Naoto Tsuji, Takashi Oka, and Hideo Aoki. Brillouin-wigner theory for high-frequency expansion in periodically driven systems: Application to floquet topological insulators. *Phys. Rev. B*, 93:144307, Apr 2016.

[76] H. A. Haus and W. Huang. Coupled-mode theory. *Proceedings of the IEEE*, 79(10):1505–1518, 1991.

[77] A. Celi, P. Massignan, J. Ruseckas, N. Goldman, I. B. Spielman, G. Juzeliūnas, and M. Lewenstein. Synthetic gauge fields in synthetic dimensions. *Phys. Rev. Lett.*, 112:043001, Jan 2014.

[78] M. Mancini, G. Pagano, G. Cappellini, L. Livi, M. Rider, J. Catani, C. Sias, P. Zoller, M. Inguscio, M. Dalmonte, and L. Fallani. Observation of chiral edge states with neutral fermions in synthetic hall ribbons. *Science*, 349(6255):1510–1513, 2015.

[79] B. K. Stuhl, H.-I. Lu, L. M. Aycock, D. Genkina, and I. B. Spielman. Visualizing edge states with an atomic bose gas in the quantum hall regime. *Science*, 349(6255):1514–1518, 2015.

[80] Luqi Yuan, Yu Shi, and Shanhui Fan. Photonic gauge potential in a system with a synthetic frequency dimension. *Opt. Lett.*, 41(4):741–744, Feb 2016.

[81] Tomoki Ozawa, Hannah M. Price, Nathan Goldman, Oded Zilberberg, and Iacopo Carusotto. Synthetic dimensions in integrated photonics: From optical isolation to four-dimensional quantum hall physics. *Phys. Rev. A*, 93:043827, Apr 2016.

[82] John D. Joannopoulos, Steven G. Johnson, Joshua N. Winn, and Robert D . Meade. *Photonic Crystals.* PRINCETON UNIVERSITY PRESS, second edition, 2008.

[83] Kazuaki Sakoda. *Optical Properties of Photonic Crystals*, volume 80 of *Springer Series in Optical Sciences.* Springer, Berlin, Heidelberg, 2nd edition, 2005.

[84] Kazuaki Sakoda. *Photonic Crystals, Second Edition.* Morikita Publishing, Tokyo, 2022. In Japanese.

[85] John D. Joannopoulos, Steven G. Johnson, Joshua N. Winn, and Robert D. Meade. *Photonic Crystals: Molding the Flow of Light.* Princeton University Press, Princeton, NJ, second edition, 2008.

[86] F. D. M. Haldane and S. Raghu. Possible realization of directional optical waveguides in photonic crystals with broken time-reversal symmetry. *Phys. Rev. Lett.*, 100:013904, Jan 2008.

[87] S. Raghu and F. D. M. Haldane. Analogs of quantum-hall-effect edge states in photonic crystals. *Phys. Rev. A*, 78:033834, Sep 2008.

[88] Zheng Wang, Y. D. Chong, John D. Joannopoulos, and Marin Soljačić. Reflection-free one-way edge modes in a gyromagnetic photonic crystal. *Phys. Rev. Lett.*, 100:013905, Jan 2008.

[89] Zheng Wang, Yidong Chong, J. D. Joannopoulos, and Marin Soljačić. Observation of unidirectional backscattering-immune topological electromagnetic states. *Nature*, 461(7265):772–775, 2009.

[90] Si-Yuan Yu, Cheng He, Zhen Wang, Fu-Kang Liu, Xiao-Chen Sun, Zheng Li, Hai-Zhou Lu, Ming-Hui Lu, Xiao-Ping Liu, and Yan-Feng Chen. Elastic pseudospin transport for integratable topological phononic circuits. *Nature Communications*, 9(1):3072, 2018.

[91] Rajesh Chaunsali, Chun-Wei Chen, and Jinkyu Yang. Experimental demonstration of topological waveguiding in elastic plates with local resonators. *New Journal of Physics*, 20(11):113036, 2018.

[92] Simon Yves, Romain Fleury, Thomas Berthelot, Mathias Fink, Fabrice Lemoult, and Geoffroy Lerosey. Crystalline metamaterials for topological properties at subwavelength scales. *Nature Communications*, 8(1):16023, 2017.

[93] Sabyasachi Barik, Aziz Karasahin, Christopher Flower, Tao Cai, Hirokazu Miyake, Wade DeGottardi, Mohammad Hafezi, and Edo Waks. A topological quantum optics interface. *Science*, 359(6376):666–668, 2018.

[94] Jiho Noh, Wladimir A. Benalcazar, Sheng Huang, Matthew J. Collins, Kevin P. Chen, Taylor L. Hughes, and Mikael C. Rechtsman. Topological protection of photonic mid-gap defect modes. *Nature Photonics*, 12(7):408–415, 2018.

[95] Yuan Li, Yong Sun, Weiwei Zhu, Zhiwei Guo, Jun Jiang, Toshikaze Kariyado, Hong Chen, and Xiao Hu. Topological lc-circuits based on microstrips and observation of electromagnetic modes with orbital angular momentum. *Nature Communications*, 9(1):4598, 2018.

[96] Kentaro Nomura. *Topological Insulators and Superconductors.* Modern Theoretical Physics Series. Maruzen Publishing, 2016.

[97] David Vanderbilt. *Berry Phases in Electronic Structure Theory: Electric Polarization, Orbital Magnetization and Topological Insulators.* Cambridge University Press, 2018.

[98] Titus Neupert and Frank Schindler. *Topological Crystalline Insulators*, pages 31–61. Springer International Publishing, 2018.

[99] N. D. Mermin. The topological theory of defects in ordered media. *Rev. Mod. Phys.*, 51:591–648, Jul 1979.

[100] Genki Yonezawa, Jun-ichi Fukuda, and Toshikaze Kariyado. Realization of topological phase in a chiral honeycomb lattice model. *Journal of the Physical Society of Japan*, 94(2):024702, 2025.

[101] Kazusa Beppu, Ziane Izri, Jun Gohya, Kanta Eto, Masatoshi Ichikawa, and Yusuke T. Maeda. Geometry-driven collective ordering of bacterial vortices. *Soft Matter*, 13:5038–5043, 2017.

[102] Hiroki Matsukiyo and Jun-ichi Fukuda. Oscillating edge current in polar active fluid. *Phys. Rev. E*, 109:054604, May 2024.

[103] Andriy Nych, Jun-ichi Fukuda, Uliana Ognysta, Slobodan Žumer, and Igor Muševič. Spontaneous formation and dynamics of half-skyrmions in a chiral liquid-crystal film. *Nature Physics*, 13(12):1215–1220, 2017.

[104] Anton Souslov, Benjamin C. van Zuiden, Denis Bartolo, and Vincenzo Vitelli. Topological sound in active-liquid metamaterials. *Nature Physics*, 13(11):1091–1094, 2017.

[105] Kushal Bagchi, Tadej Emeršič, José A. Martínez-González, Juan J. de Pablo, and Paul F. Nealey. Functional soft materials from blue phase liquid crystals. *Science Advances*, 9(30):eadh9393, 2023.

[106] Samuel J. Palmer and Vincenzo Giannini. Berry bands and pseudo-spin of topological photonic phases. *Phys. Rev. Res.*, 3:L022013, May 2021.

[107] María Blanco de Paz, Chiara Devescovi, Geza Giedke, Juan José Saenz, Maia G. Vergniory, Barry Bradlyn, Dario Bercioux, and Aitzol García-Etxarri. Tutorial: Computing topological invariants in 2D photonic crystals. *Advanced Quantum Technologies*, 3(2):1900117, 2020.

[108] Lisa M. Nash, Dustin Kleckner, Alismari Read, Vincenzo Vitelli, Ari M. Turner, and William T. M. Irvine. Topological mechanics of gyroscopic metamaterials. *Proceedings of the National Academy of Sciences*, 112(47):14495–14500, 2023/12/15 2015.

[109] Toshikaze Kariyado and Robert-Jan Slager. Selective branching and converting of topological modes. *Phys. Rev. Res.*, 3:L032035, Aug 2021.

[110] Yuan Li, Yong Sun, Weiwei Zhu, Zhiwei Guo, Jun Jiang, Toshikaze Kariyado, Hong Chen, and Xiao Hu. Topological LC-circuits based on microstrips and observation of electromagnetic modes with orbital angular momentum. *Nature Communications*, 9(1):4598, 2018.

[111] Sabyasachi Barik, Hirokazu Miyake, Wade DeGottardi, Edo Waks, and Mohammad Hafezi. Two-dimensionally confined topological edge states in photonic crystals. *New Journal of Physics*, 18(11):113013, nov 2016.

[112] Wenjing Liu, Minsoo Hwang, Zhurun Ji, Yuhui Wang, Gaurav Modi, and Ritesh Agarwal. z_2 photonic topological insulators in the visible wavelength range for robust nanoscale photonics. *Nano Letters*, 20(2):1329–1335, 02 2020.

[113] Prashant Kumar, Thi Vo, Minjeong Cha, Anastasia Visheratina, Ji-Young Kim, Wenqian Xu, Jonathan Schwartz, Alexander Simon, Daniel Katz, Valentin Paul Nicu, Emanuele Marino, Won Jin Choi, Michael Veksler, Si Chen, Christopher Murray, Robert Hovden, Sharon Glotzer, and Nicholas A. Kotov. Photonically active bowtie nanoassemblies with chirality continuum. *Nature*, 615(7952):418–424, 2023.

[114] H.-S.Kitzerow and C.Bahr. *Chirality in Liquid Crystals*. Springer, 2001.

[115] Toshikaze Kariyado and Yasuhiro Hatsugai. Manipulation of Dirac cones in mechanical graphene. *Scientific Reports*, 5(1):18107, 2015.

[116] Jeffrey C. Y. Teo and C. L. Kane. Topological defects and gapless modes in insulators and superconductors. *Phys. Rev. B*, 82:115120, Sep 2010.

[117] Julian Schulz, Jiho Noh, Wladimir A. Benalcazar, Gaurav Bahl, and Georg von Freymann. Photonic quadrupole topological insulator using orbital-induced synthetic flux. *Nature Communications*, 13(1):6597, 2022.

[118] Sunil Mittal, Venkata Vikram Orre, Guanyu Zhu, Maxim A. Gorlach, Alexander Poddubny, and Mohammad Hafezi. Photonic quadrupole topological phases. *Nature Photonics*, 13(10):692–696, 2019.

[119] Marc Serra-Garcia, Valerio Peri, Roman Süsstrunk, Osama R. Bilal, Tom Larsen, Luis Guillermo Villanueva, and Sebastian D. Huber. Observation of a phononic quadrupole topological insulator. *Nature*, 555(7696):342–345, 2018.

[120] Christopher W. Peterson, Wladimir A. Benalcazar, Taylor L. Hughes, and Gaurav Bahl. A quantized microwave quadrupole insulator with topologically protected corner states. *Nature*, 555(7696):346–350, 2018.

[121] Stefan Imhof, Christian Berger, Florian Bayer, Johannes Brehm, Laurens W. Molenkamp, Tobias Kiessling, Frank Schindler, Ching Hua Lee, Martin Greiter, Titus Neupert, and Ronny Thomale. Topolectrical-circuit realization of topological corner modes. *Nature Physics*, 14(9):925–929, 2018.